Laboratory Electrical Model of the Louis-Hippolyte Lafontaine Tunnel

Vincent Prévost

A Thesis
in
The Department
of
Electrical and Computer Engineering

Presented in Partial Fulfillment of the Requirements
for the Degree of Master of Applied Science (Electrical and
Computer Engineering) at
Concordia University
Montréal, Québec, Canada

October 2019

CONCORDIA UNIVERSITY

SCHOOL OF GRADUATE STUDIES

This is to certify that the thesis prepared

By: Vincent Prévost

Entitled: "Laboratory Electrical Model of the Louis-Hippolyte Lafontaine Tunnel"

and submitted in partial fulfillment of the requirements for the degree of

Master of Applied Science

Complies with the regulations of this University and meets the accepted standards with respect to originality and quality.

Signed by the final examining committee:

_____ Chair, Examiner
Dr. Chunyan Lai

_____ Supervisor
Dr. Pragasen Pillay

_____ Examiner, External
Dr. Andreas Athienitis to the Program

Approved by: _____
Dr, Yousef R. Shayan
Department of Electrical and Computer Engineering

October 17, 2019

_____
Dr. Amir Asif
Dean, Faculty of Engineering
and Computer Science

ABSTRACT

Laboratory Electrical Model of the Louis-Hippolyte Lafontaine Tunnel

Vincent Prévost

The Louis-Hippolyte Lafontaine tunnel is defined as a critical infrastructure as it represents a major transportation link connecting the island of Montreal and the South Shore. Consequently, the daily operation of the tunnel is highly dependent on the stability of the electrical grid to maintain a proper power supply. Moreover, the changing electrical profile of the tunnel throughout the year is reflected differently on the grid. Hence, the scope of this work is to emulate and model a scaled-down version of the electrical system of the tunnel Louis-Hippolyte Lafontaine based on different operational scenarios. The system that is considered is simplified to the main electrical loads, which are the heating (purely resistive), lighting (mostly resistive) and ventilation fans. The modeling of the electrical profile is achieved using measurement-based data. To achieve the emulation of the ventilation fan, a drive system for a 2-hp induction motor is modeled in the MATLAB/Simulink environment and validated experimentally using open-loop voltage-over-frequency control under no-load condition. The results show proper speed control with the flux maintained constant under rated frequency in addition to accurate response to speed command change. To illustrate the changing operational profile of the tunnel throughout the year, the scaled-down electrical system is simulated and adapted to the corresponding profile of a summer day, a winter day and during an emergency event (diesel generator supply). For each distinctive day, the power characteristics at the point of common coupling are evaluated in regards to the respective electrical loads connected to the system. The analysis of the scaled-down simulated system has shown that the nature of the loads solicited in their respective scenarios has different impacts on the supply system. Through this research work, the scaled-down model of the Louis-Hippolyte Lafontaine tunnel electrical system showed similar power characteristics to what is observed on the actual system.

Acknowledgment

First and foremost, I would like to express my deepest gratitude to my supervisor, Professor Pragasen Pillay, for his invaluable guidance and support throughout this research project. I would also like to express my gratitude to the committee members Dr. Andreas Athienitis and Dr. Chunyan Lai for their time and valuable help through the review process of this research work.

Moreover, I would like to thank my colleagues from the Power Electronics and Energy Research (PEER) group for their support and the knowledge they shared during the last two years. Amongst them, I am extremely grateful to Dr. Mohammad Masadeh for his continuous help in the writing of this thesis and Dr. Mathews Boby for his help in the implementation of the experimental setup.

Special thanks to my good friends, Jean-Sébastien Fiset, Gabriel Broday, Karin Feistel, Mohamed Omer and last but not least Luccas Kunzler for their invaluable help and moral support all along this journey. The camaraderie shared with them during these two years contributed significantly to the completion of my master's studies.

Finally, I am forever indebted to my family for whom I can only express my deepest gratitude for their continuous encouragements and support during my studies. Without them, this accomplishment would not have been achievable.

Table of Contents

List of Figures

List of Tables

Nomenclature

AC	Alternative Current
BESS	Battery Energy Storage System
DC	Direct Current
DTC	Direct Torque Control
DPF	Displacement Power Factor
EMF	Back Electromotive Force
ESS	Energy Storage System
FFT	Fast Fourier Transform
FOC	Field-Oriented Control
HPS	High Pressure Sodium
IGBT	Insulated-Gate Bipolar Transistor
LED	Light-Emitting Diode
MTMDET	Ministère des Transports, de la Mobilité durable et de l'Électrification des transports du Québec
P	Active Power (W)
PF	Power Factor
PV	Photovoltaics panels
PWM	Pulse Width Modulation
Q	Reactive Power (Var)
RMS	Root Mean Square
RPM	Revolutions Per Minute
S	Apparent Power (VA)
SLD	Single-Line Diagram
SPWM	Sinusoidal Pulse Width Modulation
THD	Total Harmonic Distortion
UPS	Uninterruptible Power Supply
V/f	Voltage-Over-Frequency (V/Hz)
VFD	Variable Frequency Drive

Chapter 1: Introduction

1.1 Introduction

Electrical power is a key component of contemporary society's infrastructure. Indeed, modern power transportation and distribution technologies facilitated the society's access to a reliable and constant electricity supply. As a result, for a vast majority of the city's infrastructures, electricity is essential to maintaining their operational activities. From those, a group of infrastructures, designated as critical infrastructures, are pillars to the stability of modern society by enabling and ensuring the population access to essential services to properly function. The Government of Canada refers to the following definition to describe a critical infrastructure [1]:

"Critical infrastructure refers to processes, systems, facilities, technologies, networks, assets and services essential to the health, safety, security or economic well-being of Canadians and the effective functioning of government. […] Disruptions of critical infrastructure could result in catastrophic loss of life, adverse economic effects and significant harm to public confidence."

In other words, infrastructures such as the electrical grid, telecommunication services, hospitals, airports, railways, and tunnels are labeled as critical infrastructures due to their permanent necessity in ensuring the well-being and safety of the population. Hence, in their design, resiliency must be a crucial requirement to be considered in order to prevent any disruption of service in case of emergency situations, a result of a power outage. An infrastructure is defined as resilient by their capacity to withstand and recover quickly to an extreme and hazardous event perturbing and interrupting the services they provide [2]. For instance, interruption of activities is often a result of extreme weather incidents, considered as one of the greatest threats to the operation of the infrastructure, which consequently results in a notable economic impact on society [2]. Considering the current climate change context, extreme weather events are subjected to occur more frequently and severely, thus justifying the need to account for resiliency in the design of these critical infrastructures to limit any future economic and safety concerns for the society [3]. Therefore, the configuration of the electrical system of these infrastructures should be in a way that an auxiliary power system has to be included in the design to withstand the essential electrical loads and ensure an efficient and smooth transition in the event of a power outage.

When looking at the infrastructures located in the province of Quebec, the Louis-Hippolyte Lafontaine tunnel can be labeled as a critical infrastructure as it agrees with the above definition established by the Government of Canada. Indeed, the tunnel is a major link between the island of Montreal and the South Shore into which passes hundred of thousands of vehicles on a daily basis [4]. Like other critical infrastructures, the tunnel's daily operation is highly dependent on the stability of the electrical grid to provide the required level of power. Parts of the tunnel overall system, labeled as essential loads, must constantly be powered to avoid any damage to the material in addition to any potential harm to the public safety, thus the requirement for resiliency toward any perturbation to stability events.

Large infrastructures, such as the Louis-Hippolyte Lafontaine tunnel, have an important energy consumption allowing them to meet their operational requirements. They are currently fed primarily from the electrical grid and equipped with some limited backup power capability in situation of emergency. The variety of instruments found in the tunnel electrical system and their corresponding high power ratings are often the cause of power quality disturbances. Of the recurring problems, voltage sag, high harmonics level and low power factor (PF) can be the result of the tunnel's system operation. The starting of a motor, load variations and presence of non-linear loads are all examples of such causes [5, 6]. To overcome these power quality issues, uninterruptible power supplies (UPS) can be used as a way to mitigate sags, passive or active harmonic filters can be incorporated to limit the harmonics and capacitor banks can be added to improve the PF through reactive power compensation [5]. The integration of all these power quality mitigation devices results in having a quality of power within the standards of the energy provider.

As indicated previously, the interdependency between the critical infrastructure and the electrical provider is such that in order to preserve stability, strategies must be implemented to reduce their operational impacts that are reflected on the electrical grid. To do so, one alternative could be the integration of a renewable energy system, such as solar photovoltaic (PV) panels combined with an energy storage system (ESS), as an auxiliary power supply. The addition of this new system would help the critical infrastructure to meet its important electrical load during a grid outage, hence improving the resiliency of the tunnel toward unexpected power loss. Furthermore, the tunnel electrical system could benefit from the integration of solar PV and ESS systems by

contributing to the peak load management, thus reducing their demand from the grid during peak hours [7]. Implementing such configuration requires a large additional capital investment for the PV panels and a properly sized ESS. However, in addition to the economic savings generated by limiting the peak power demand, this renewable auxiliary power system could also be used as a way to enhance the overall power quality of the tunnel [8]. Harmonics mitigation and PF improvement are achieved by means of controlling the converter interfacing the DC side of the PV and ESS with the AC side of the tunnel network [9].

1.2 Thesis Objective

The main objective of this research work is to implement and study the electrical profile typically observed in critical infrastructure and have a better understanding of its operational profile. The considered case study for the purpose of this research is the Louis-Hippolyte Lafontaine tunnel infrastructure, a major transportation link between the island of Montréal and the South Shore. The scope of this thesis is to implement and emulate, on a smaller laboratory scale, the main components of the tunnel electrical system and study the electrical profile under different scenarios. The overall system is scaled-down to a level that lies within the power limitation of the equipment available in the laboratory.

The concept of emulation refers to the process of reproducing the operational characteristics of a specific element, such as a motor, an ESS or also electrical loads. The emulation of a given device is achieved based on the concept of Hardware-in-the-loop, which consists of using hardware and software tools for testing, namely a real-time simulator, to replicate its actual electrical profile without having to physically test the system to be emulated [10].

Henceforth, the emulated system is comprised of the electrical grid, as the main supply, and a diesel generator, as an auxiliary and emergency power supply. The power system feeds the electrical loads of the tunnel. For the purpose of this research, the electrical loads that are considered are the lighting, heating and ventilation loads. Their corresponding electrical profile models are developed based on measurements completed on the full-scale system taken in the tunnel.

Furthermore, the emulation of the ventilation electrical loads is implemented through a series combination of an electrical drive (AC-DC-AC converter) and a three-phase induction motor. As

for its operational profile, a control strategy is developed to control the rotational speed of the motor similarly to how the ventilation fan reference speed would be subjected to change as a result of the variation in the air quality observed in the tunnel. The selected approach is a scalar voltage-over-frequency (V/F) control strategy for its simplicity and due to the nature of the given application.

Then, based on the measurements taken on the actual tunnel's system for the considered main electrical loads and the model developed for the ventilation system, different operational scenarios are implemented in the Simulink environment. Indeed, the load profile of the tunnel varies depending on the seasons. Consequently, scenarios are developed for the summer, winter and emergency operational profiles, each adapted to the loads that are usually powered during the corresponding period. With each profile implemented independently, the power characteristics of the emulated system are analyzed at the point of common coupling (PCC).

1.3 Thesis Outline

The research thesis is structured into five chapters, as follows.

Chapter Two will present a thorough description of the critical infrastructure considered in this research work, with the main focus oriented toward its electrical configuration. For the purpose of this thesis, the electrical load profile is assumed to consider only the main components, which are the lighting, heating and ventilation loads. In this chapter, a model is defined for the system to be considered in this thesis, based on the power requirements established for the corresponding electrical load.

Chapter Three will study the operational behavior of a three-phase induction motor and its electrical drive as an emulation of the electrical profile of ventilation fans as found in the tunnel. Ventilation fans are highly important in such infrastructure as they are essential to maintain an adequate level of air quality for the user's safety. In the situation where the level is inadequate, the ventilation fans are operating at a higher speed. To emulate the behavior of this load, a scalar Voltage/Frequency control is adopted for the electrical drive allowing a speed control for the induction motor.

Chapter Four will present the complete simulation of the tunnel electrical system considered for this research work, which includes lighting, heating and ventilation electrical loads. In this

simulation, the electrical grid acts as the main supply whereas the diesel generator set represents auxiliary backup power supply powered on during an emergency event. The implemented model is based on the measurements taken on the actual loads found in the tunnel, and the validated ventilation fans system model. The scaled-down electrical model of the tunnel was tested for three different operational scenarios: summer, winter, and during an emergency event. The power characteristics at the PCC are then analyzed for each scenario to assess potential harm to the tunnel electrical infrastructure given the nature of the current system configuration.

Chapter Five will conclude this thesis and research work and propose relevant future research work.

Chapter 2: Description of the Louis-Hippolyte Lafontaine tunnel Electrical System

2.1 Introduction

The critical infrastructure that is considered for this research project is the Louis-Hippolyte Lafontaine tunnel, a major transportation link between the island of Montreal and the South Shore of the Saint-Laurent River as shown in Figure 2.1. With a length of 1.5 km, it is considered as the longest underwater tunnel in Canada [11]. The construction of the tunnel was completed in 1967 and then, opened for public transit. Currently, there are roughly 120,000 vehicles passing daily through the tunnel, for which its maximum capacity is met 10 hours per day [12]. After roughly 50 years of existence, the Quebec Ministry of Transportation is currently planning a major repair work for the tunnel to extend its lifetime by 40 years, while also improving the infrastructure operational system up to the 21st Century standards. Indeed, in addition to upgrading the structure, this repair project will also look into incorporating more efficient electrical, lighting and ventilation systems into the new design. Currently, the control of the operational profile of the tunnel overall system is achieved through the North and South control towers, each responsible for the operation of their respective equipment.

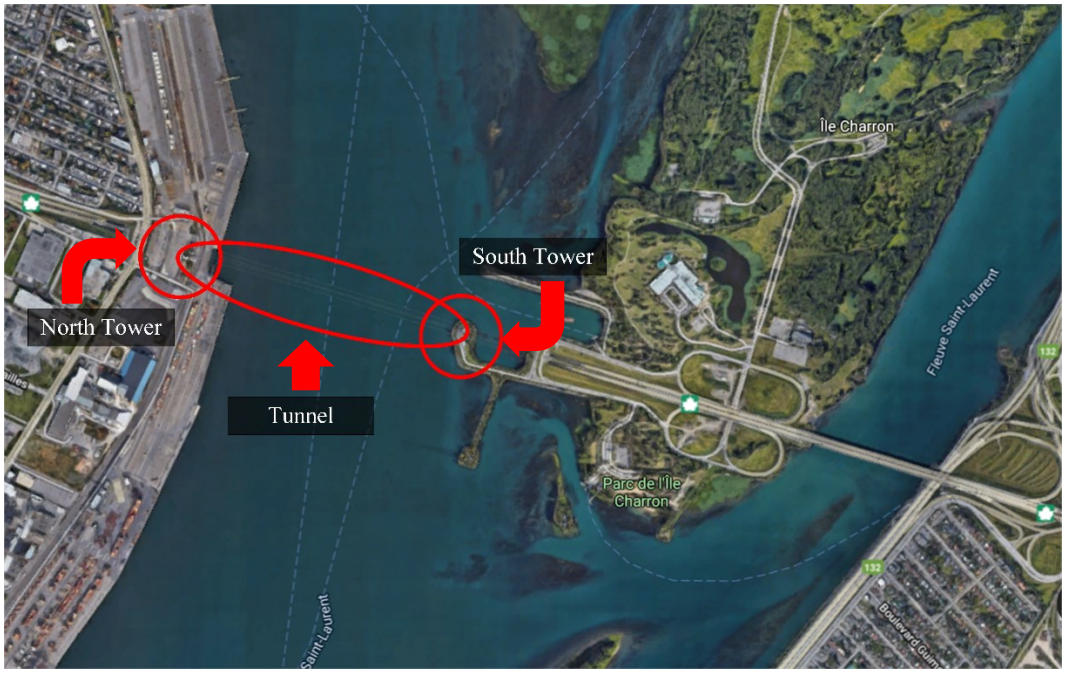

Figure 2.1: Location of the Louis-Hippolyte Lafontaine tunnel [13].

This chapter will present an overview of the electrical system found in the Louis-Hippolyte Lafontaine tunnel and the power characteristics observed for the main electrical loads, which are the lighting, ventilation and heating loads.

2.2 Tunnel Electrical System Layout

The Louis-Hippolyte Lafontaine tunnel electrical system is currently fed from Hydro-Québec at a voltage level of 12.47 kV. The main distribution is then spread into two sub-distribution networks, one feeds the North tower systems and the second supplies the South tower systems. The main supply coming from Hydro-Québec is then stepped down to a voltage level of 347/600 V. Indeed, both towers are equipped with two step-down transformers, connected respectively to two distinct main electrical buses feeding a different set of electrical loads in the tunnel. Moreover, to achieve power factor correction through reactive power compensation, capacitor banks are added to each of these four main electrical distribution buses as a way to meet the electrical power quality standards. In addition to the main supply coming from the electrical grid, the tunnel is also equipped with limited backup power capability in an instance of emergency, consisting of diesel generator sets and uninterruptible power supplies (UPS), which will later be described.

Furthermore, to illustrate and provide the reader with a proper illustration of the tunnel electrical system layout, a single-line diagram (SLD) indicating the electrical pumps and motors located in both towers is shown in Figure 2.2. As can be seen, their ratings vary from few horsepower (hp) to more than a hundred hp. As illustrated in Figure 2.2 (b), the South Tower is powered from the main 12.47 kV electrical bus located in the North Tower (SW101) as the Hydro-Québec substation is located on the island of Montreal. The power is then transported from the North tower to the South tower electrical system through the tunnel full length.

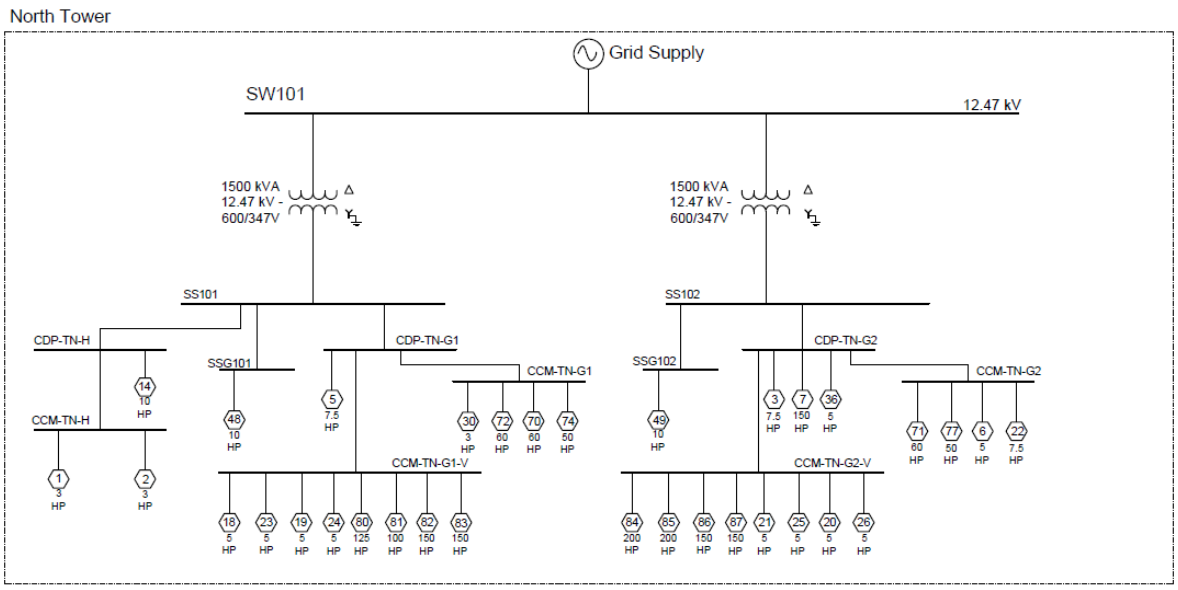

(a)

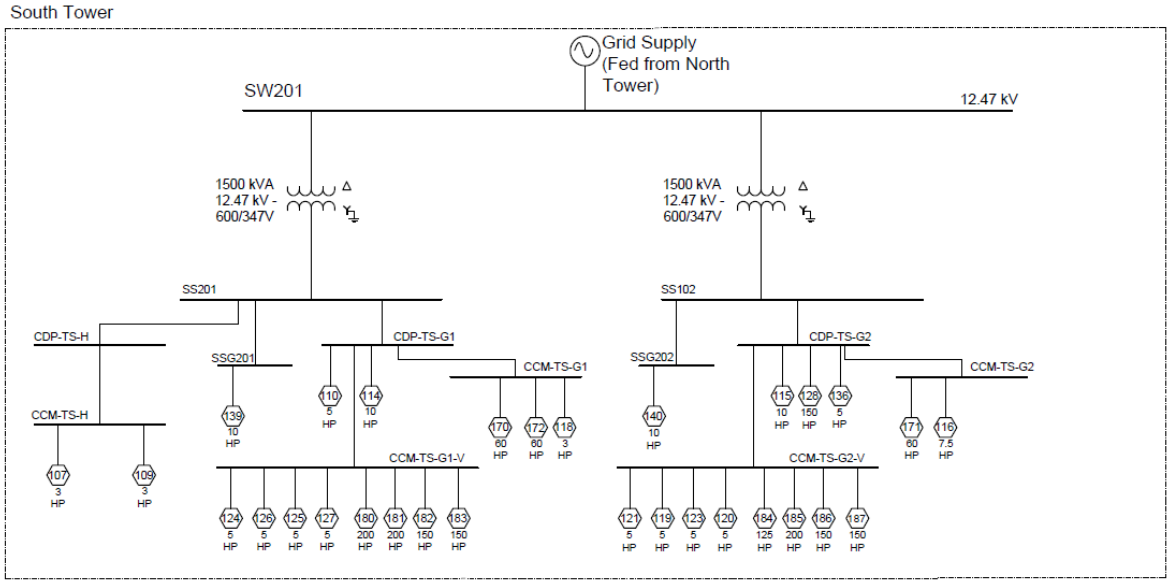

(b)

Figure 2.2: Simplified tunnel's SLD: (a) North tower motorized loads and electrical pumps distribution system, and (b) south tower motorized loads and electrical pumps distribution system.

2.2.1 Tunnel Emergency System

The Louis-Hippolyte Lafontaine tunnel is also equipped with some limited backup power capability in the situation of emergency where the tunnel is completely disconnected from the

electrical provider, which is Hydro-Québec in this case. The current emergency system found in the tunnel consists of a combination of diesel generators and UPS. The North and South towers are equipped with a set of two diesel generators to withstand the energy demand from the essential system ensuring continuity and safety in the tunnel operation. However, in a situation where the tunnel is completely disconnected from the electrical grid, a certain period of time is required for the diesel generators to come online and be able to supply the essential loads. As such, a secondary power supply must be present to withstand these essential loads during the startup process of the generators. Thus, a UPS system is also part of each tower emergency system as a means to ensure continuous power supply without any disruption from the moment power is lost from Hydro-Québec to the moment the diesel engines come online. The essential electrical loads will be described in the next section.

2.3 Tunnel Operational Profile

2.3.1 Normal Operation

The operational profile of the tunnel is subject to variations on a yearly basis. Indeed, the temperature plays an important role in the energy profile due to various systems being operated differently based on the outside weather. For instance, the heating elements are mainly operating during the winter period as a means to mitigate the freezing of the tunnel systems. Henceforth, when referring to the load profile of the tunnel on a yearly basis, it can be seen that the peak power met during a day is considerably higher during the winter period compared to the summer period, which can be observed in Figure 2.3. The peak power information used for this graph was taken from the historian database of the Louis-Hippolyte Lafontaine tunnel electrical profile for the year of 2015 provided by the Ministère des Transports, de la Mobilité durable et de l'Électrification des transports du Québec (MTMDET). The load profile is implemented through samples taken every 15 minutes. Given the confidentiality of this information, the peak power values were scaled down to a "per unit" reference frame as a means to keep undisclosed the actual values, while maintaining a representative picture of the operational profile of the tunnel on a yearly basis.

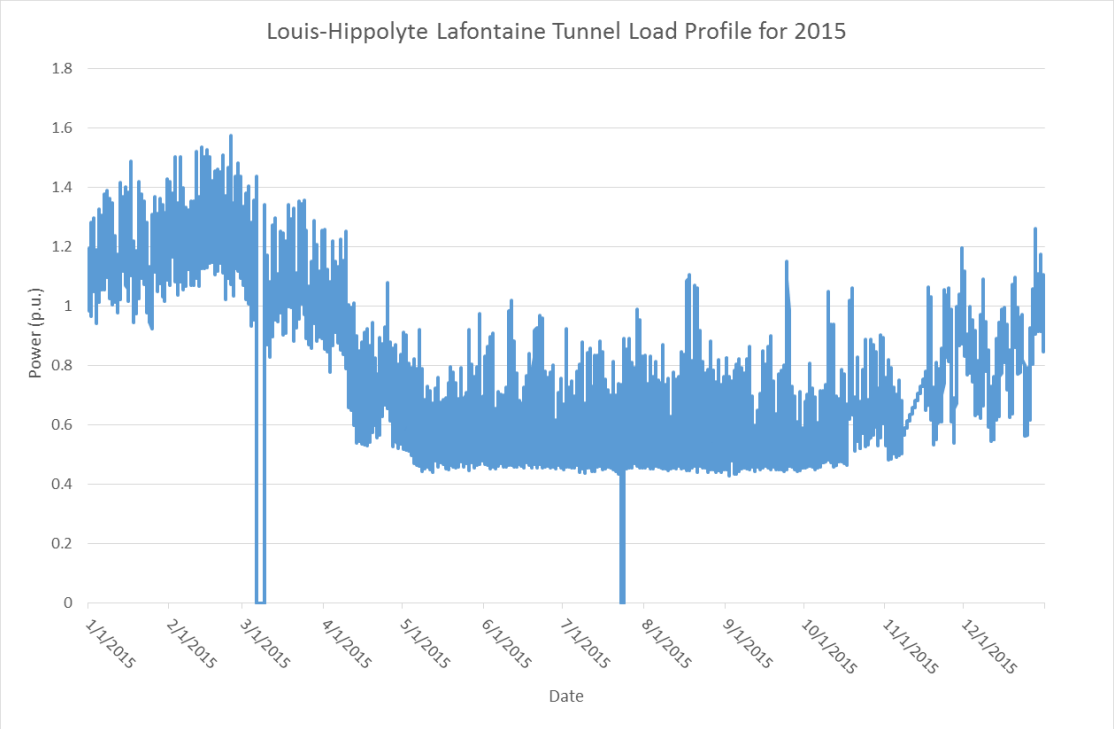

Figure 2.3: Louis-Hippolyte Lafontaine tunnel load profile for the year of 2015.

Some discontinuities can be observed in Figure 2.3 where dips in the load power consumption can be observed in the months of March and August as a result of missing information within the database for these days. The load profile of the tunnel reaches its peak power consumption for the year of 2015 during the month of February, where the temperature is colder. Hence, during this day, the overall load of the tunnel is at its highest level mainly because of their heating requirements. When looking at the daily load profile of the tunnel for a winter and summer days as shown respectively in Figure 2.4 and Figure 2.5, it can be observed that the daily peak power period is starting at around 8 AM and is ending roughly at sunset. Thereby, such an observation is explained by the fact that the lighting electrical loads are representing a large proportion of the overall load profile of the tunnel. Furthermore, the lighting levels found in the tunnel are dynamically changing throughout the day to respect and maintain safe vision standards for the users. Indeed, the lighting levels found in the tunnel are at their highest when the outside luminosity is also at its highest intensity as a means to facilitate the transition inside the tunnel for the human eye. Hence the power consumption is dropping following the sun's path to sunset with the inside lighting levels progressively reducing.

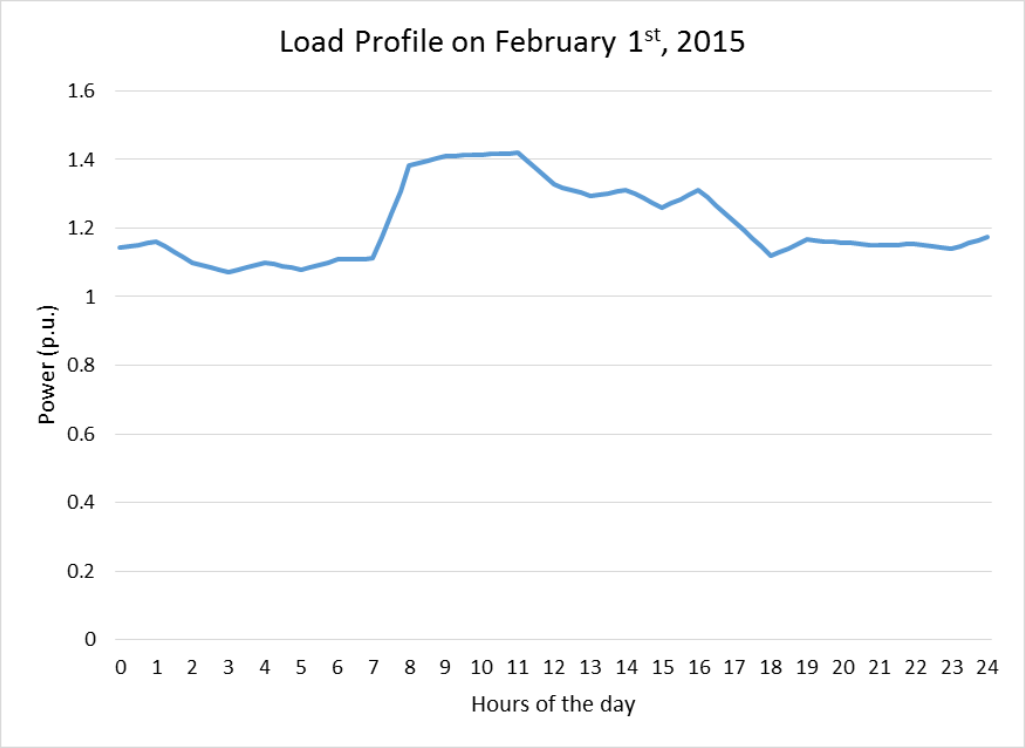

Figure 2.4: Louis-Hippolyte Lafontaine tunnel daily load profile on February 1st, 2015.

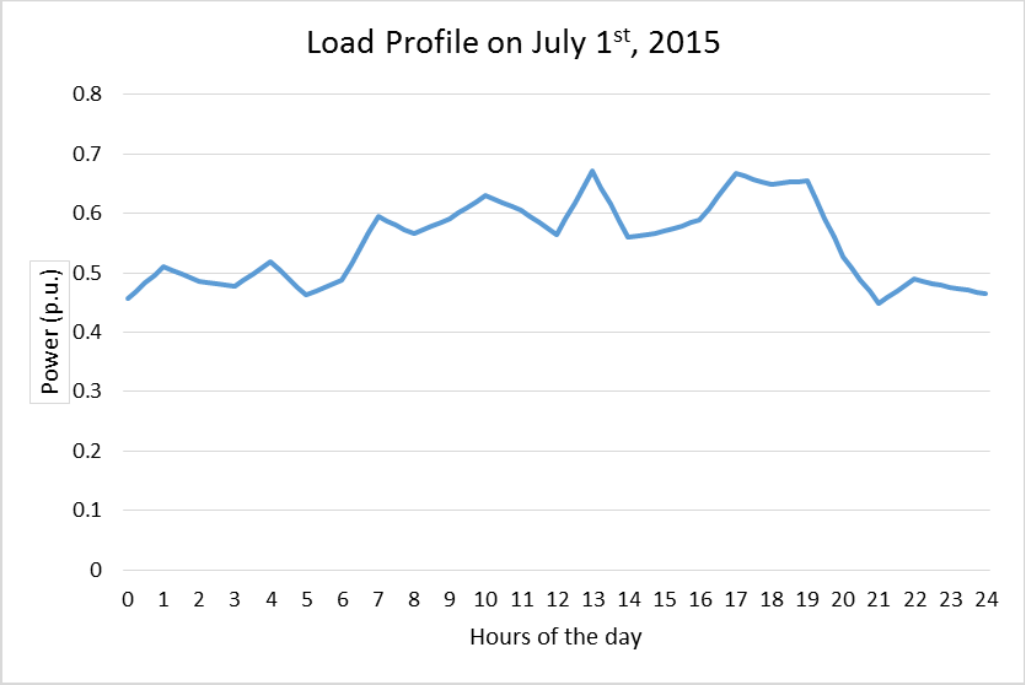

Figure 2.5: Louis-Hippolyte Lafontaine tunnel daily load profile on July 1st, 2015.

As shown in Figure 2.4 and 2.5, the daily peak period is concluding roughly when the sun goes down, which is occurring earlier during the winter in comparison to the summer. Indeed, when considering the sampling period, which is characterized by the time of the year and the hours of the day, it can be observed that the heating and lighting electrical loads play an important part in establishing the level and the shape of the tunnel load profile. With the heating electrical system being a major contributor to the energy profile, the daily load profile of an arbitrary winter day is shifted up when compared to a summer day due to the large power requirements for the heating elements. Indeed, from Figures 2.4 and 2.5, the load profile observed during February 1st is varying between 1.07 and 1.42 p.u. whereas the range lies between 0.45 and 0.67 p.u. during the day of July 1st, a result of the changes in the heating requirements between the seasons.

Furthermore, as indicated in the report entitled "*Efficacité Énergétique et Déglaçage des Entrées et Sorties Sans Utilisation de sel du Tunnel Louis-Hippolyte-La Fontaine"* [14], the main electrical loads that are the heating, lighting, and ventilation systems are estimated to be representing roughly between 60 to 70% of the total energy consumption of the tunnel. The remaining 30% of the energy consumption consists of systems such as pumps, electronics, air conditioning, etc. Throughout the year, the percentage impact of each load on the total energy consumption does not represent a constant data and is subjected to change based on different criteria. As mentioned previously, the temperature is playing a major part in determining the operational profile of the tunnel, however, another criterion such as the level of occupancy inside the tunnel will determine to which level the ventilation fans would operate to ensure a satisfactory level of quality of air. As such, during the warmest months of the years, the ventilation fans are operated more frequently to overcome the effect of higher temperatures on the quality of air inside the tunnel. Hence, during the winter period, the fans are practically never operating. In regards to the lighting electrical load, the daily energy consumption is characterized by constant consumption levels throughout the year. Additionally, with the lighting load playing a major part in the energy consumption of the tunnel, it represents only approximately 30% of the total energy consumption during the winter compared to roughly 65% during the summer, the reason being the high ratings and constant operation of the heating elements during the colder months, for which the proportion of the total energy profile can go up to 65%.

Overall, the normal operation of the tunnel is designated as the operation of all required systems inside the tunnel when powered entirely by the electrical provider. However, situations might arise where the tunnel is completely disconnected from the grid. However, during these periods, a selected number of equipment essential to the tunnel operation must continuously be powered from the emergency backup system.

2.3.2 Emergency Operation

As indicated above, the Louis-Hippolyte Lafontaine tunnel is equipped with a combination of a diesel generator set and a UPS system as a backup power system acting as a contingency supply in the situation of emergencies where the tunnel is disconnected from the main power supply. These situations can be categorized into two scenarios. One is designated by a service interruption where the tunnel is experimenting a grid outage being completely disconnected from Hydro-Québec. The second situation is designated as an operational emergency during a potential fire that is ignited inside the tunnel and must be extinguished rapidly to limit the damages. During those rare events of fire occurrence, only the essential loads are powered by the backup power system. These include:

- Emergency tunnel and services lighting,
- Air conditioning for the UPS system,
- Tunnel ventilation,
- Drainage pump sumps,
- Fire pumps, and
- Heating cables and heating elements.

In these emergency situations of a fire, the fire pumps, drainage pumps, and ventilation fans are operating jointly to accelerate the extinguishing process of the fire. Indeed, the fire pump injects a water supply in the sprinkler system to extinguish the flames, the drain pipes are required for the drainage of the water excess resulting from the fire protection system while the ventilation fans are used to exhaust the smoke from the tunnel.

In the events of outage where the tunnel's electrical system is disconnected from the electrical system and no operational emergencies arise, the backup power system can, based on the situation, supply electrical loads designated as non-essential in addition to the essential loads required for

the tunnel's operation. Indeed, the capability of the diesel generators allows for these loads to be powered as the operation of the fire pumps is not required and the requirements for the ventilation fans are lowered in the absence of fire with them usually running at approximately 5% of their capability. The following systems are categorized as non-essential electrical loads:

- Building heating,
- Building ventilation,
- Pumps, and
- Tour access ramp defrosting system.

As previously mentioned, the tunnel overall system is divided into two locations: the North and South towers. Each tower is equipped with its own backup power supply and the loads, both essential and non-essential, have basically the same ratings and capabilities. Thus, in the event of operational emergencies, the operation percentage of the electrical loads is relatively the same in both towers. As such, Table 2.1 is illustrating how the load is dispatched in the North tower under three different operational profiles established in "*Note Technique n°6: Calcul des Charges Électriques du Système Existant*" [15]. Scenario A is representing the normal operation of the tunnel when tied to the electrical grid. Then, scenario B is designated as the situation at which the tunnel electrical system is completely disconnected from the grid and the electrical loads are powered by the diesel generators and UPS system. Finally, scenario C is represented as the event where an operational emergency is occurring (e.g. a fire) and the tunnel is disconnected from the grid and only the essential loads are powered by the diesel generators and the UPS system.

Table 2.1: Louis-Hippolyte Lafontaine tunnel essential electrical loads operation percentage under different operational profile.

Electrical Load Description	Scenario A: Normal Conditions (Grid) Operation %	Scenario B: Grid Outage (Diesel + UPS) Operation %	Scenario C: Fire Event (Diesel+ UPS) Operation %
Normal Tunnel Lighting	70%	N/A	N/A
Normal Tunnel Services Lighting	10%	N/A	N/A
Tunnel Night Lighting	100%	100%	100%
Emergency Tunnel Lighting	100%	100%	100%
Emergency Tunnel Services Lighting	70%	100%	100%
Tunnel Night Instrumentation Lighting	100%	100%	100%
UPS Air Conditioning Distribution Panel	30%	100%	100%
Tunnel Ventilation	3%	5%	35%
Drainage Pump System	15%	15%	80%
Fire Pump System	0%	0%	100%
Heating Cables	50%	80%	80%

The indication of N/A in Table 2.1 is indicating that the electrical load to which it is associated is not to be powered in their respective scenarios. As for the 0 %, it is indicating that the operational percentage of the load under normal operating conditions. This value is subjected to increase in the situation of a particular event.

2.4 Main Electrical Loads

As indicated previously, the main contributors to the energy profile of the tunnel are the heating, lighting, and ventilation electrical systems. They represent approximately 60 to 70% of the total energy consumption of the tunnel. During the month of January 2018, a site visit was conducted in the tunnel facilities to complete electrical measurements on these main electrical systems. The tool used to take these measurements was the *Fluke 435-Series II* power analyzer. The scope of this site visit was to define power equations to estimate the power consumption of each of these main electrical loads to help in the approximation of the tunnel load profile. The developed equations were taking into consideration only the data monitored and stored in the

tunnel database. As such, the available information for the heating system is the current drawn by the element. In regards to the lighting system, the data monitored is the outside level of flux that determines which level of lighting is turned on. Finally, for the ventilation fans, the stored data includes the current drawn by the fan in addition to the rotating speed of the fan. Thus, to implement the approximated power equations, voltage and current measurements were taken locally on the distribution of each type of loads in order to obtain their respective power characteristics.

2.4.1 Heating Elements

The high energy consumption ratings of the tunnel's heating system are mainly a result of the protection system in place to mitigate the freezing of the fire protection conduits, the domestic water pipes, and the drainage system conduits. In order to do so, this protection system is resorting to electrical heating cables. Additionally, the overall heating system electrical load is also including the system in place that is responsible for heating up the tunnel's office premises and the pathways de-icing system.

As part of this site visit, measurements were taken for three different sets of heating loads. With the help of the tunnel's electrician, the following loads were turned on for analysis:

- *Heating Load #1*: Fire protection
- *Heating Load #2:* Fire protection
- *Heating Load #3:* Domestic water protection

These loads were selected as their respective capacities form a large proportion of the complete heating system. The measurements were taken once the heating load had reached the steady state in order to obtain a more accurate profile of the heating system power consumption. In Figure 2.6, the distribution and control panel for the heating elements is shown. From this panel, the RMS current and voltage values for each phase were taken from the sensor display downstream of the circuit breaker corresponding to the selected load.

Figure 2.6: Louis-Hippolyte Lafontaine tunnel heating distribution panel.

In the ensuing procedure, the current and voltage measurements taken for these heating loads are summarized below in Table 2.2.

Table 2.2: Heating elements power characteristics

Heating Element	**Line Voltage V_{AB} (V)**	**Line Voltage V_{BC} (V)**	**Line Voltage V_{CA} (V)**	**Line Current I_A (A)**	**Line Current I_B (A)**	**Line Current I_C (A)**	**Power Factor (PF)**	**Active Power (kW)**
Heating Load #1	202	206	204	21.9	20.3	21.2	1	7.47
Heating Load #2	204	204	206	28.6	27.6	47	1	12.21
Heating Load #3	205	207	206	5.5	3.17	3.9	1	1.49

As illustrated in Table 2.2, the heating loads of the tunnel electrical system are purely resistive as indicated by the measured unity power factor for all of them. Consequently, these heating loads are only consuming active power (P). A realistic assumption can be established in regards to the

overall heating system consuming only active power. Therefore, the power consumption for the heating elements can be estimated using Equation 2.1.

$$P_{Heating} = \left\{\left(\frac{V_{AB}}{\sqrt{3}} \times I_a\right) + \left(\frac{V_{BC}}{\sqrt{3}} \times I_b\right) + \left(\frac{V_{CA}}{\sqrt{3}} \times I_c\right)\right\} \quad (2.1)$$

In Equation 2.1, the RMS line voltages and currents of the heating element that is considered for analysis are used for the calculation of the power.

2.4.2 Lighting Electrical System

The second main electrical load of the tunnel is the lighting electrical system. Even though the heating system has a considerably higher energy consumption during the winter season, on a yearly basis, the lighting electrical system has the largest energy consumption of all, with it being constant all year long. The system that is currently in place inside the tunnel is consisting of a set of high pressure sodium (HPS) lighting bulbs, which are commonly used in public lighting system due to their high efficiency, their large range in the visible spectrum and their long durability over time [16, 17]. For the renovation project, lighting emitting diodes (LEDs) are considered as a replacement lighting system for the HPS due to their lower power consumption requirements. However, the use of LED is leading also to some power quality concerns in regards to the harmonic distortion generated by their drivers. Thus, to mitigate these power quality concerns, the tunnel would need to incorporate into its configuration systems that would reduce the harmonics and improve the power factor.

As illustrated in Figure 2.7 (a) and (b), the current and voltage measurements for the lighting electrical loads were taken for all three phases and neutral at the intermediary point that is designated by the safety switch panel. Measurements were taken with all levels of lighting turned on, which represent a scenario where the outside luminosity is above a standard flux threshold. Thus, the tunnel lighting level must be at their maximum to smoothen the transition from outside to inside. Then, the site electrician opened each breaker individually to observe and measure the corresponding power characteristics for each of the lighting levels.

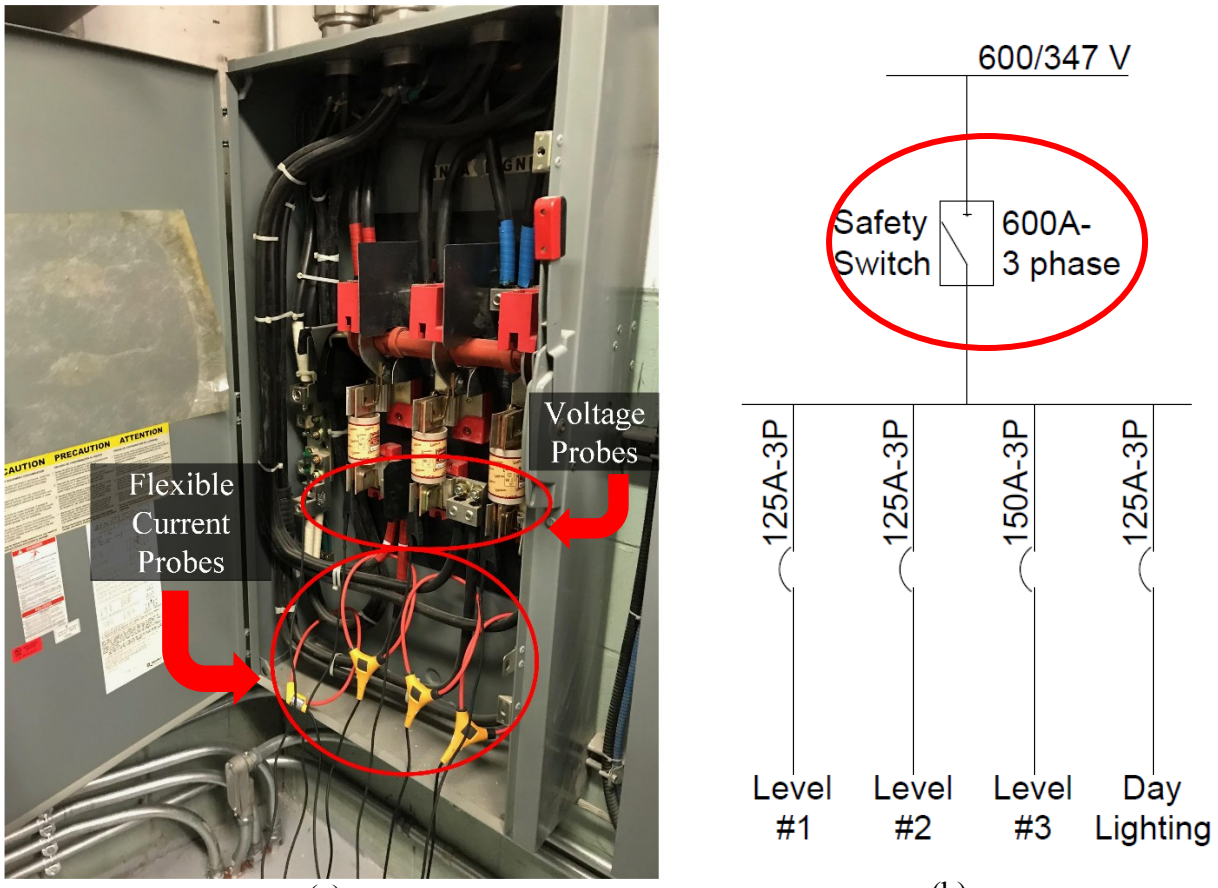

(a) (b)

Figure 2.7: Lighting system's electrical measurements: (a) Louis-Hippolyte Lafontaine lighting system safety switch, and (b) Simplified single line diagram of the North tower lighting system.

For this portion of the site visit, the *Fluke 435-Series II* instrument was used to record the current and voltage RMS values, active power (P), reactive power (Q), apparent power (S), Power Factor (PF), magnitude of harmonics within the order range from 1st (fundamental) to the 50th and last, Total Harmonic Distortion (THD). It is worth mentioning that the test procedure was conducted for the North tower lighting system. The hypothesis that the same power characteristics can be observed for the South tower lighting system can be assumed as the same type of light and somewhat the same quantity can be found. The measured data for the scenario where all circuit breakers are turned on are summarized in Table 2.3.

Table 2.3: Lighting electrical system power characteristics.

Parameters \ Phase	A	B	C	Neutral	Total
Phase Voltage (V)	344.33	343.45	349.05	N/A	N/A
Line Voltage (V)	535.67	535.67	535.67	N/A	N/A
Line Current (A)	180.53	185.03	184.11	5.36	N/A
Active Power (W)	58,909.35	60,211.54	60,622.76	N/A	179,743.66
Reactive Power (Var)	20,516.21	20,998.48	22,016.62	N/A	63,506.68
Apparent Power (VA)	62,163.09	63,547.58	64,266.11	N/A	189,989.81
Power Factor	0.95	0.95	0.94	N/A	0.95
Current THD (%)	1.02	1.36	0.61	254.74	N/A
Voltage THD (%)	0.44	0.34	0.53	18.31	N/A
Voltage Unbalance (%)*	N/A	N/A	N/A	1.03	N/A
Current Unbalance (%)*	N/A	N/A	N/A	1.28	N/A

* deviation from rated value

Using the data summarized in Table 2.3, the power consumption for the lighting system can be estimated using the following equation:

$$P_{lighting} = \{(V_a \times I_a \times PF_a) + (V_b \times I_b \times PF_b) + (V_c \times I_c \times PF_C)\}. \quad (2.2)$$

The RMS line currents and phase voltages in addition to the PF are used for the estimation of the power consumption. However, this equation can only be used if the current values are known. If they are unknown, one alternative consists of using the power rating of one HPS bulb to which the ballast power consumption is added. Then, this power for a single unit is multiplied by the total number of units for a given lighting level.

Referring to the information provided in Table 2.3, the lighting system has a PF close to unity, thus indicating that it is mainly consuming active power. Furthermore, the voltage and current THD percentages of the supply signals show low distortions of maximum values of 0.53% and

1.36% respectively. They are well under the limitations prescribed by *IEEE Std 519-1992 Harmonic Limits* [18]. The high THD percentage observed in the neutral conductor can be explained by the low fundamental current value at 60 Hz compared to the sum of the harmonics.

2.4.3 Ventilation Fans

Finally, the remaining main electrical load to be analyzed is the ventilation fan system. The tunnel is equipped with two different sets of electric fans. The first one consists of the air supply fans tasked with bringing fresh air from outside to inside the tunnel. As for the other set, the exhaust fans duties involve removing the polluted air from inside to outside. The overall ventilation system is equipped with motors rated within the range of 100 to 200 hp. As mentioned earlier in this chapter, this load is mainly operating during the warmer seasons as the inside air quality is deteriorated under high-density traffic and hotter temperature conditions. The tunnel is equipped with multiple carbon monoxide and nitrogen dioxide probes to sense their levels and once a certain threshold is met, a signal is sent and the fans are starting to operate.

In order to analyze the energy profile of the ventilation system, the *Fluke 435-Series II* was used to take measurements at the input of the variable frequency drive (VFD) associated with the ventilation fan under study as indicated in Figure 2.8 a) and b). In doing so, the actual power consumption drawn for the operation of the fan could be extrapolated considering the motor and drive efficiencies. Furthermore, by taking the measurements at this location, the extent of the current harmonics generated by the VFD could be logged and analyzed later on. Measurements were taken once the steady state was reached for all three modes of operation for which the motors are running ideally at 50%, 66% and 100% of the rated speed.

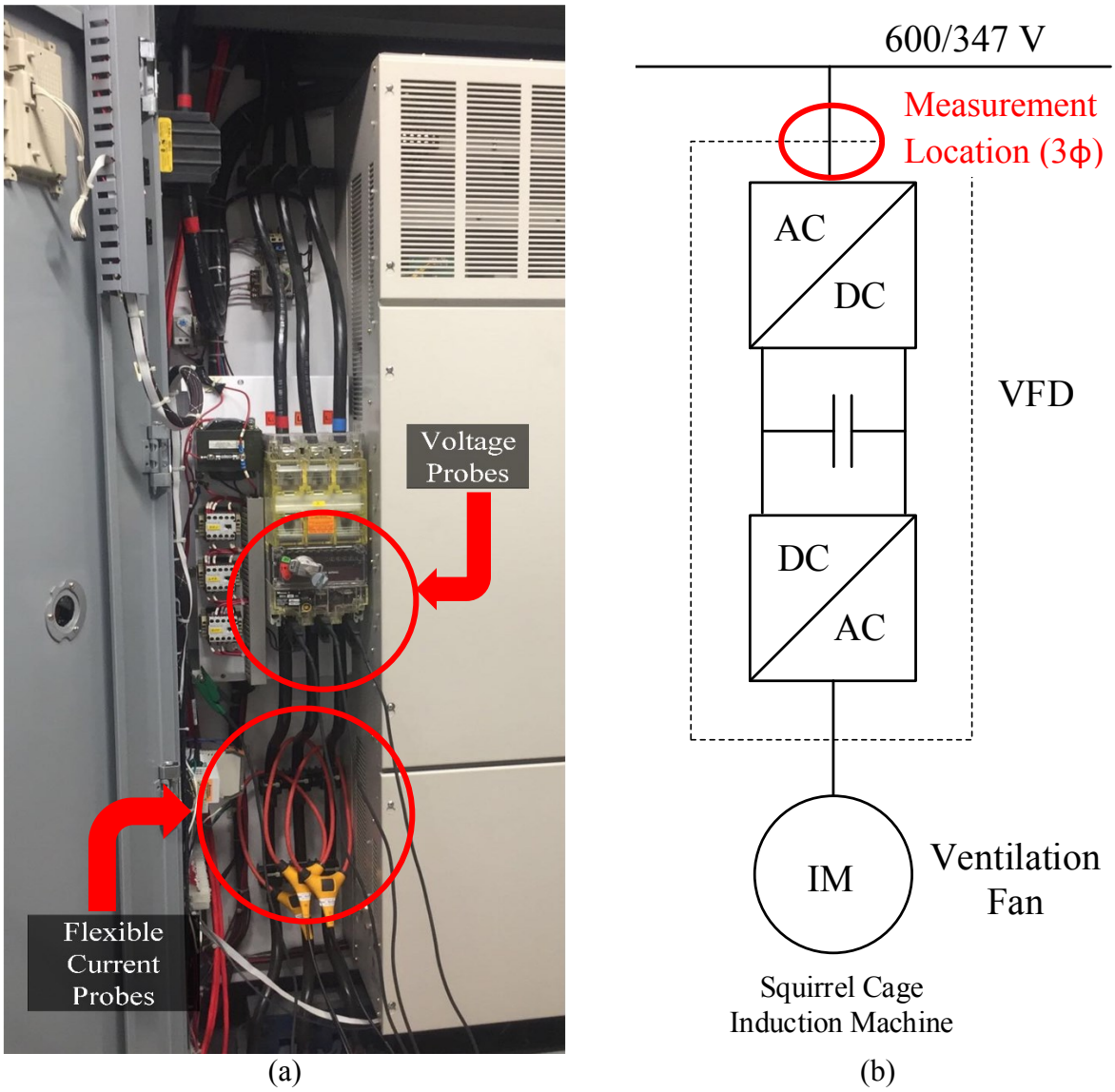

Figure 2.8: Ventilation fan system's electrical measurements: (a) Actual ventilation fan VFD system, and (b) simplified single line diagram for the fan VFD system.

The measurements at the steady state conditions are summarized below for a load percentage of 50% and 89.1% and are tabulated respectively in Table 2.4 and Table 2.5. The measured data illustrate the power characteristics change once the speed is increased.

Table 2.4: Air supply ventilation fan power characteristics under a load percentage of 50% @ 204 RPM.

Parameters \ Phase	A	B	C	Neutral	Total
Phase Voltage (V)	346.28	347.20	350.38	N/A	N/A
Line Voltage (V)	535.67	535.67	535.67	N/A	N/A
Line Current (A)	41.64	33.08	48.94	4.07	N/A
Active Power (W)	9091.67	8206.49	13,044.43	N/A	30,342.76
Reactive Power (Var)	4665.92	45.03	1746.24	N/A	6465.30
Apparent Power (VA)	14,418.86	11,483.71	17,147.61	N/A	43,556.21
Power Factor	0.63	0.71	0.76	N/A	0.70
Current THD (%)	99.93	97.42	83.57	9.83	N/A
Voltage THD (%)	1.20	0.99	1.41	20.99	N/A

Table 2.5: Air supply ventilation fan power characteristics under a load percentage of 89.1% @ 390 RPM.

Parameters \ Phase	A	B	C	Neutral	Total
Phase Voltage (V)	345.22	345.19	349.50	N/A	N/A
Line Voltage (V)	535.67	535.67	535.67	N/A	N/A
Line Current (A)	161.66	158.38	184.40	4.04	N/A
Active Power (W)	47,852.46	49,708.67	58,560.21	N/A	156,121.32
Reactive Power (Var)	15,468.69	6,423.36	13,096.02	N/A	34,957.84r
Apparent Power (VA)	55,809.78	54,671.41	64,447.13	N/A	175,278.0
Power Factor	0.86	0.91	0.91	N/A	0.89
Current THD (%)	48.76	43.79	39.58	2.92	N/A
Voltage THD (%)	2.81	2.45	2.67	26.08	N/A

As can be observed from Table 2.4 and Table 2.5, once the load percentage increases, the power factor is also incidentally increasing. Indeed, the amount of active power consumed by the fans is becoming larger compared to the amount of reactive power, which is essentially remaining constant at different load percentage.

As indicated by the measurement location in the ventilation system, the active power values shown in Table 2.4 and Table 2.5 are taking into consideration the drive efficiency. Thus, considering that the current values drawn by the fans are logged in the tunnel database, the active power consumption can then be approximated using the following equation:

$$P_{fan} = \frac{\sqrt{3}\, V_{LL} \times I \times PF}{Drive\ Efficiency}. \tag{2.4}$$

Another alternative could be the estimation of the consumed power using the speed of the fan. The following relation is proposed by the Affinity law, which stipulates that the power is proportional to the cube of the fan shaft speed [19].

$$P_{fan} \propto \left(N_{shaft}\right)^3 \tag{2.5}$$

Therefore, using the relation proposed by the Affinity law, the power consumption of the analyzed fan can be estimated using the following equation where the drive and motor efficiencies are taken into consideration to account for the losses.

$$P_{fan} = \frac{k * \left(N_{shaft}\right)^3}{Drive\ Efficiency * Motor\ Efficiency} \tag{2.6}$$

For large motors, the efficiency is relatively high and usually within the range of 0.95 [20]. As for the drive, the efficiency is changing based on the loading percentage of the motor. When operating below a load percentage of 50%, the efficiency of the drive is relatively low compared with the condition where the drive is operating above this threshold where a conservative approximation of efficiency would be around 0.85.

2.4.3.1 Harmonics

Even though VFDs are a proven tool in the control of the speed of motors, their usage has led to some concerns regarding their impact on the power quality of industries electrical systems. As shown in Table 2.4 and Table 2.5, the current THD percentage is considerably higher than the voltage one. Consequently, the current signal is highly distorted and harmonics are injected upstream into the distribution system, which could be harmful to other systems. The distorted input line current of the drive system and the input phase voltage are shown in Figure 2.9. It is to be noted here that the measured input current was measured in the opposite direction of the actual flow. Hence, the line current seems to be 180 ° phase shifted from the phase voltage. However, as typically observed with drive, the line current and the phase voltage should have a displacement power factor (DPF) close to unity.

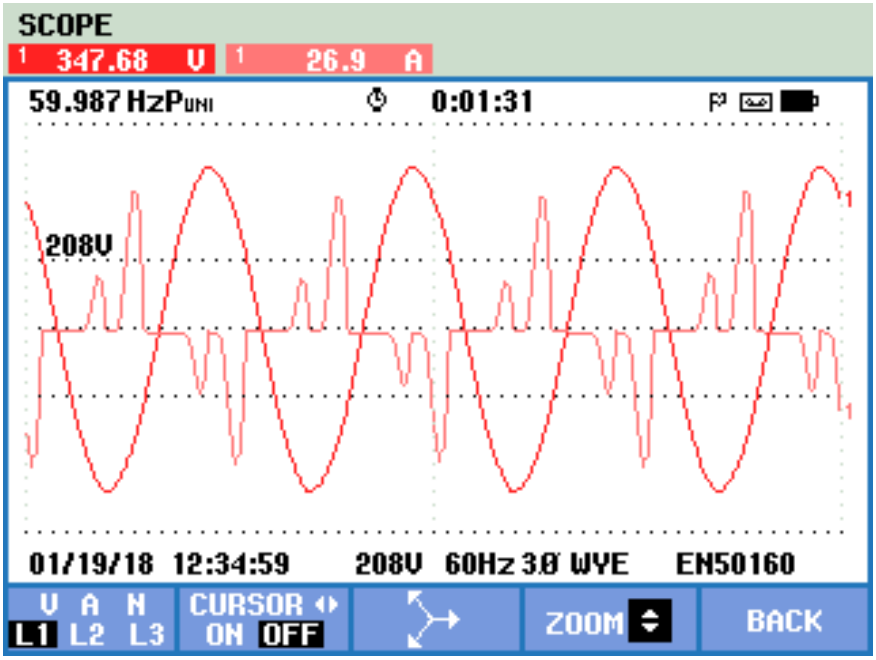

Figure 2.9: Phase voltage and line current waveform at low load percentage.

Furthermore, Figures 2.10 and 2.11 are illustrating the current harmonic spectrum respectively for operation at 50% and 89.9%.

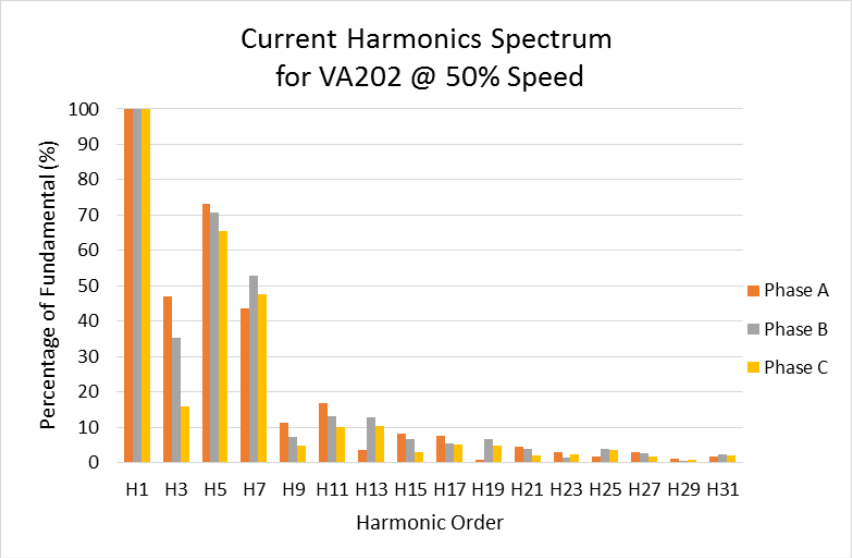

Figure 2.10: Current harmonics spectrum @ 50% load.

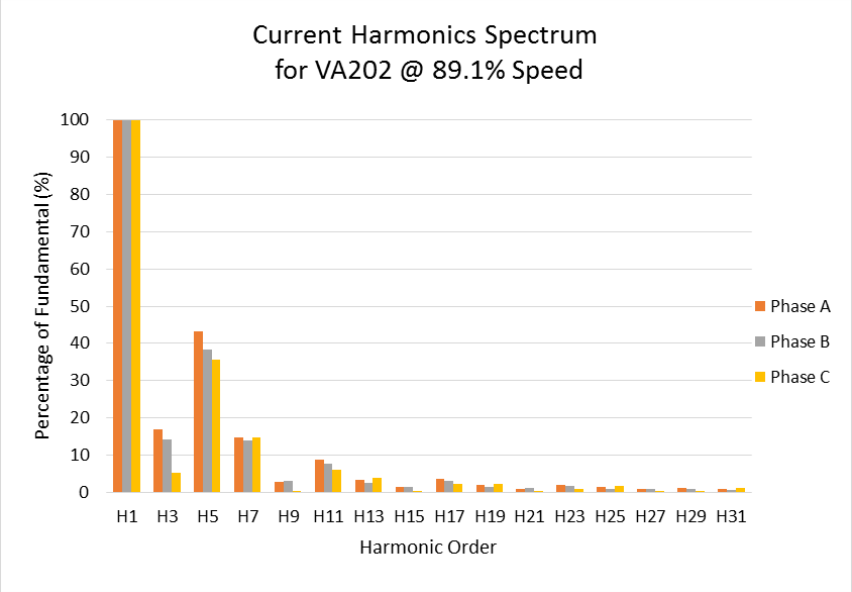

Figure 2.11: Current harmonics spectrum @ 89.1% load.

As the ventilation fans are operating toward full capacity, the current THD tends to decrease, while keeping the same switching mechanism in the drive. Indeed, the fundamental component of the current increases at a larger load percentage while the harmonics generated by the variable

frequency drive remain relatively constant. Hence, a reduction in the current THD ratio is occurring at a higher loading percentage.

In addition to the harmonics being harmful to other systems, the THD percentage at the point of common coupling with the electrical provider must be below a certain level to avoid any penalties. Parts of the generated harmonics will be canceled with each other's in the electrical distribution network. However, for the remaining harmonics, mitigation tools are required to enhance the power quality up to the standards.

2.5 Summary

In this Chapter, the Louis-Hippolyte Lafontaine tunnel electrical system was introduced. The power flow of this system was then described as whether the tunnel is fed from the electrical grid or the emergency backup power system. Furthermore, the operational profile was discussed with regards to the electrical load variations between the normal operations of the tunnel versus the emergency operations based on the report produced by the engineering consulting firm [15]. Once the tunnel was disconnected from the electrical grid, essential loads were prioritized in order to maintain a safe operation of the tunnel. Finally, following a site survey of the tunnel, power equations were developed based on the measurements conducted on the three main electrical loads (heating, lighting, and ventilation) to approximate the power consumption of each of them using only the information available in the tunnel's logging database system.

Chapter 3: Modeling and Validation of Variable Frequency Drives (VFDs) Operation with Ventilation Fans

3.1 Introduction

The supply and exhaust ventilation fans are essential systems inside the tunnel infrastructure as they are considerably contributing to ensuring a proper and safe daily operation. As indicated previously in this work, they are responsible for maintaining the air quality above a specified threshold. On an electrical level, the ventilation system is basically consisting of multiple sets of variable frequency drive (VFD) used to drive the induction motor to a given speed, which in turn is acting as the prime mover for the fan blades.

In regards to the ventilation system of the tunnel, induction motors are used as the prime movers for the blades. Indeed, this type of motor is commonly found in industrial electrical infrastructure due to not only its high efficiency but also its robustness, simplicity, and high reliability. In addition to their operational advantages, induction motors are also characterized by their economic benefits. Indeed, they require less maintenance and are also found at an affordable price as a result of the simplicity of their design [21, 22, 23]. Due to the fact of being widely used in industrial applications, they are responsible for a significant proportion of the total electrical energy consumption of the industries, which can reach up to more than 80% [24, 25]. Consequently, strategies should be implemented as a means to reduce their impact on the energy profile of the infrastructure. As such, the progress made in the power semi-conductors research field over the past decades allowed for a more efficient operation of the induction motor through the use of VFDs. Basically, the VFD technology is defined by the conversion from the AC supply to DC through means of a rectifier. Then, the filter capacitor on the DC link smoothens the DC voltage ripple. The DC voltage is then converted back to an AC signal at the desired frequency through the inverter (IGBT based) controlled by a pulse width modulation (PWM) signal. The simplified VFD design is illustrated in Figure 3.1.

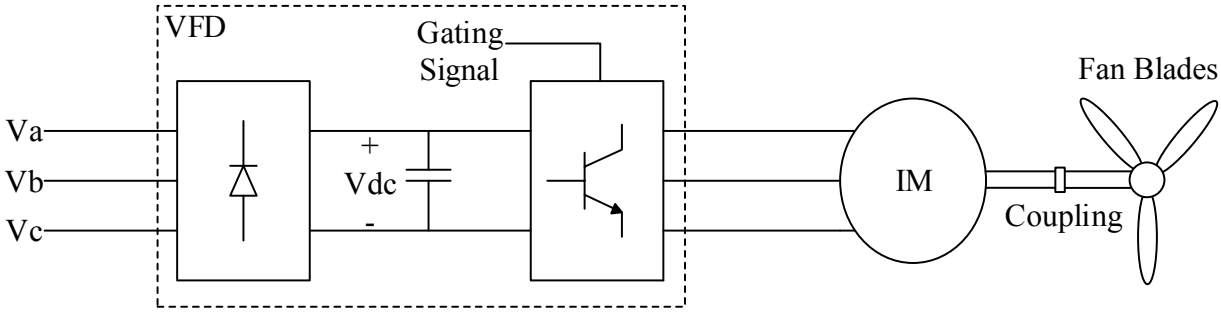

Figure 3.1: Simplified diagram of a VFD system connected to an induction motor.

Following the simplified VFD diagram shown in Figure 3.1, the drive system is designed and built experimentally to validate the developed speed control scheme for the induction motor. The end product is shown in Figure 3.2 and the components used will be described in a later section of this Chapter.

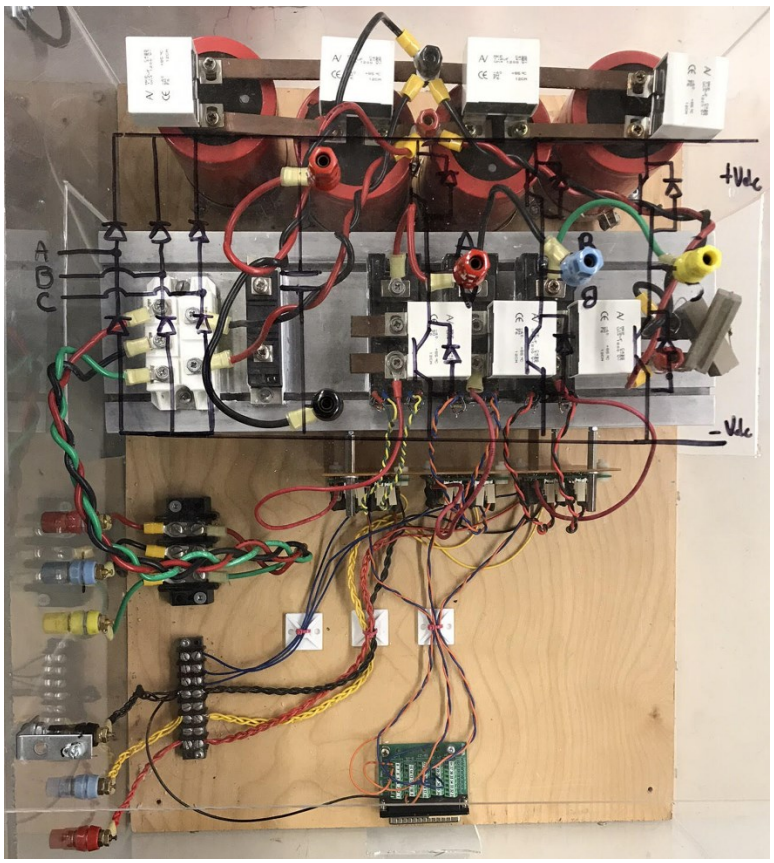

Figure 3.2: Drive converter implemented experimentally.

Moreover, the inverter of the VFD can be controlled via the gates signal of the inverter switches based on the user's speed and torque requirements, from which a reference signal will be generated. Consequently, VFDs are often prevailing, depending on the applications, over fixed speed controllers as they are more energy efficient which results in an enhanced overall operation [26]. In regards to the tunnel ventilation system, VFDs are used to control the rotational speed of the ventilation fans to meet the air quality standards. Therefore, the energy profile of the ventilation electrical load is enhanced due to savings generated when operating at a lower speed. Consequently, it is proven to be beneficial on an operational perspective as it reduces also the maintenance requirements [27].

3.2 VFDs Control Strategies

The control of the VFD is achieved through the switching mechanism of the inverter. Many induction motor control strategies have been developed over the past years [28, 29] and constantly optimized since then [30, 31, 32]. The three main schemes are the scalar control, field-oriented control (FOC) and finally, direct torque control (DTC), which are all summarized below [33].

3.2.1 Scalar Control

The scalar control, also known as constant voltage-over-frequency (V/f) control, relies on the concept of maintaining a constant flux density of the induction motor for the operation of the machine at frequencies that are less than or equal to the rated frequency [32]. In order to do so, the armature voltage is adjusted accordingly to the operational frequency, thus maintaining a constant voltage-over-frequency ratio resulting in a constant rated flux density. Within this control strategy, the assumption that the voltage drop across the stator impedance is negligible when operating in the higher range of frequencies is made [33]. Consequently, the back electromotive force (EMF) is approximated to be equal to the applied stator voltage. However, when the motor is operating at a lower speed, the approximation is no longer valid as the voltage drop across the stator impedance is becoming significant and must be taken into consideration for the V/f control scheme. To overcome this concern and maintain the linear relation below the rated frequency, a boost voltage is added into the control scheme [32]. The simplest solution consists of approximating the boost voltage as the voltage drop across the stator resistance under rated current condition [34]. Other more complex strategies have been developed to enhance the scalar control under low-speed operation. In [34], the boost voltage is taken into consideration through vector compensation of

the voltage drop across the stator resistance and slip frequency compensation to develop torque. In [35], an open-loop scalar slip compensation control scheme is proposed where flux estimation and speed sensors are not required. The compensation scheme is determined from the motor parameters and the stator current using a feedforward strategy.

3.2.2 Field-Oriented Control (FOC)

Another alternative control scheme for drives is based on the vector-based field-oriented control theory, from which a better dynamic response is observed when compared to the constant V/f control scheme. Indeed, within the FOC technique, the *a-b-c* stator current components are converted to the *d-q* reference frame. As such, once steady state is reached, the sinusoidal AC components of the induction motor can be expressed as their DC equivalent quantities through this transformation. Moreover, the stator current *d-axis* component corresponds to the field quantity whereas the stator current *q*-axis is designated as the torque component of the induction motor [33]. Furthermore, within the FOC scheme, an analogy with the control of a separately excited DC motor can be made as it allows for independent control of the flux and the torque [36]. The torque of the induction motor is controlled through the *q*-axis component of the stator current, while maintaining to a constant value the *d-axis* component. The FOC technique can be achieved either directly or indirectly. In the direct approach, the angle of the flux is determined either through direct measurement of air gap flux or is estimated based on the voltage and current measurements. As for the second technique, the indirect vector control scheme uses the rotor speed and slip compensation to determine the flux angle, hence given the nature of the feedback signal, which procures a more robust control strategy compared to the direct approach [33, 36].

3.2.3 Direct Torque Control (DTC)

Using direct torque control scheme with an induction motor allows for a fast response to sudden load torque variations. The control is achieved using a hysteresis tolerance band for the torque and flux error signals, from which the switching states of the inverter are determined based on space-vector modulation, where the stator voltage vectors are selected from a look-up table. DTC control scheme has some benefits when compared to FOC control technique. Indeed, the exemption of the need to convert the signals to a different set of coordinates reference frame in addition to having no requirement for current feedback control result in a simplified control procedure. However, DTC operation at low-speed results in lower performance due to the effect

generated from the stator impedance voltage drop, thus resulting in a less accurate flux estimation [37, 38]. An additional drawback to DTC is observed in the higher torque ripples [33].

Based on the characteristics associated to the respective control techniques used for induction machines and given the nature of the Louis-Hippolyte Lafontaine tunnel case study, the open-loop scalar control provides satisfactory performance in terms of the emulation of the ventilation fan system where the requirements for speed feedback and high dynamic performance are not mandatory to the operation [39]. Henceforth, for applications where sudden and precise changes in the motor running speed are not required, the open-loop scalar control scheme is selected for driving the induction motor. With less intensive requirement for the dynamic response, the driving system is less complex and results in economic benefits, thus justifying the selection of this control scheme for the modeling of the drive presented in this chapter [35].

3.3 Induction Motor

As indicated previously, induction motors are considered as the workhorse of the industry due to their high reliability, robustness, efficiency and also their low cost. Moreover, in regards to the Louis-Hippolyte Lafontaine tunnel ventilation system, the induction motor is used as the prime mover to drive the supply and exhaust fans.

For this case study where the tunnel electrical profile is emulated on a scaled-down level, the selected induction motor driving the ventilation fans is a three-phase squirrel-cage induction motor rated at 2-hp. In Table 3.1, the selected motor machine characteristics are presented.

Table 3.1: Induction motor nameplate information selected for the case study *[40]*.

Baldor Industrial Motor M1556T -Nameplate Information-	
Power	2-hp
Voltage	208-230 V
Current	6.1 A
Speed	1725 RPM
Frequency	60 Hz
Phase	3φ
Configuration	Wye-Connected
Class	B

The per-phase equivalent circuit of the induction motor is illustrated in Figure 3.3. However, the selected motor machine parameters are unknown and must be determined in order to implement the motor model. To do so, Method 2 of IEEE Std 112™ – 2017 entitled *IEEE Standard Test Procedure for Polyphase Induction Motors and Generators* is used as a reference [41].

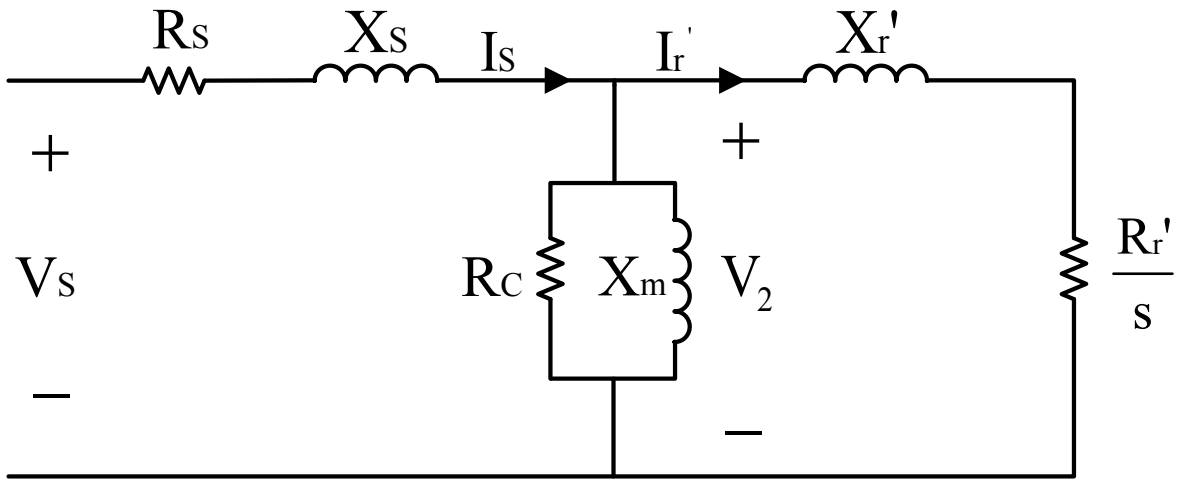

Figure 3.3: Per-phase equivalent circuit of an induction motor.

where V_s is the stator phase voltage, R_s is the stator resistance, X_s is the stator leakage reactance, R_c is the core loss resistance, X_m is the magnetizing reactance, X_r' is the rotor leakage reactance referred to the stator, R_r' is the rotor resistance referred to the stator and s is the slip.

In order to determine the circuit parameters shown in the above Figure 3.3, three different sets of tests based on IEEE Std 112™ – 2017 should be accomplished. The DC test is done for the stator resistance calculation, whereas the No-Load test and the Locked-Rotor test were completed to determine the 2-hp motor remaining machine parameters considered for this case study [42, 43].

3.3.1 DC Test

The DC test is allowing for the calculation of the stator resistance R_s independently of the other circuit parameters. This procedure consists of applying a DC voltage V_{DC} at the stator winding terminal. Then, with the current being a DC quantity, no voltage is induced on the rotor and consequently, only the stator resistance must be considered in the DC test. With the induction motor being *WYE*-connected, the current flows through the stator resistances of two phases. Thus,

in order to calculate the per-phase stator resistance, the current is adjusted to its rated value and the stator terminal voltage is measured. It is assumed that the three-phase windings are identical and equal. Hence, the stator resistance is then calculated as follows:

$$R_s = \frac{V_{DC}}{2I_{DC}}. \tag{3.1}$$

The measurements have been taken at cold and hot temperatures by using a high precision resistance measurement device from Tektronix DMM 4020. Furthermore, the procedure of having the motor run for about 15 minutes helps achieving closer values to the ones if the machine is being operated at rated conditions. The three-phase measured resistances are indicated in Table 3.2.

Table 3.2: DC Test measured resistances.

DC Test Results	
R_{AB}	2.7159 Ω
R_{BC}	2.7136 Ω
R_{CA}	2.7150 Ω

The values indicated in Table 3.2 must be divided by two to consider the per-phase resistance. Then, the stator resistance considered in the equivalent circuit is the average value of Table 3.2 quantities. The stator copper loss can then be calculated using the measured resistance.

3.3.2 No-Load Test

The second test to be completed is the No-Load test for which the motor is running at rated voltage with no constraints imposed on the motor shaft. Within this test, the magnetizing reactance and the core loss resistance can be determined through the rotational losses of the induction motor. For this procedure, the applied voltage is varied from 125% of the rated voltage down to the value at which the current begins to increase again. The corresponding current and power measurements are taken for each point. The friction and windage ($P_{F\&W}$) losses can be estimated from the intercepting point of the curve showing the relation between the subtracted stator copper loss to the input power and the voltage squared as shown in Figure 3.4 [41].

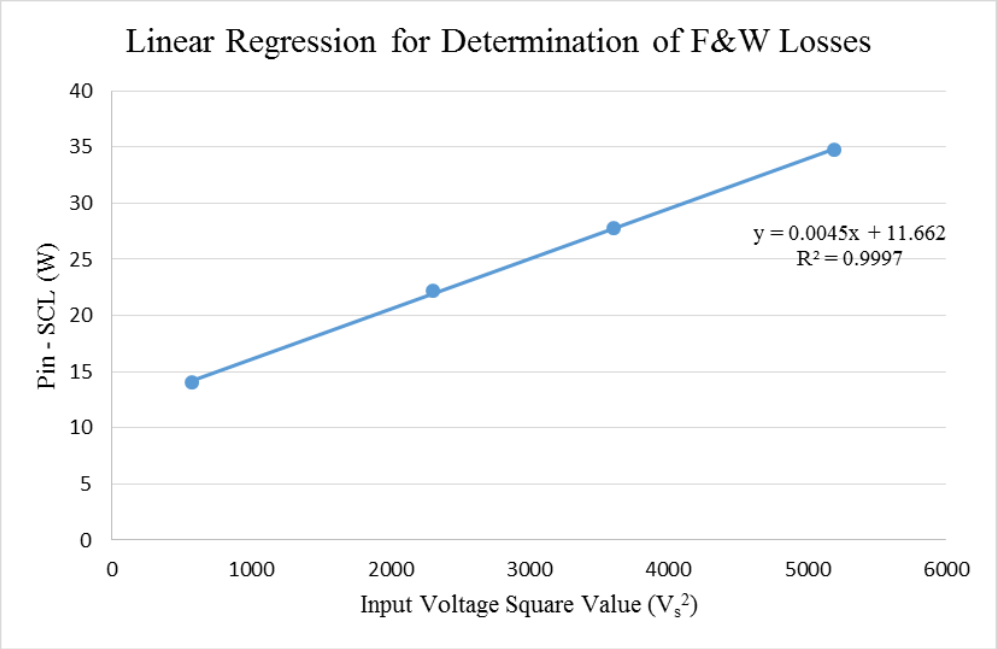

Figure 3.4: Linear regression for determination of F&W losses.

From Figure 3.4, one can observe that, given the linear regression equation, the F&W losses are estimated to be 11.66 W. Then, subtracting the F&W losses from the stator copper losses (SCL), the core loss power can be determined. The measured input power is defined by the following equation:

$$P_{in} = P_{SCL} + P_{core} + P_{F\&W} \tag{3.2}$$

where P_{SCL} represents the stator copper losses, P_{core} corresponds to the no-load core losses and $P_{F\&W}$ designates the friction and windage losses. The required quantities used for the parameter determination are summarized in Table 3.3, where the values at the rated voltage of 208 V are shown.

Table 3.3: No-load test measurements at the rated voltage.

No-load test measurements	
Phase Voltage	120.12 V
Line Current	1.46 A
3φ Input Power	122.28 W
SCL	39.07 W
F&W losses	11.66 W
Core Loss	71.55 W
Magnetizing Reactive Power	1068.35 Var

Then the measurements taken for the input current and power at the nominal motor voltage are used to determine the voltage across the branch of the magnetizing inductance and the core loss resistance, which is defined as V_2 in Figure 3.3. The voltage drops across the stator resistance and stator leakage reactance is determined from the phasor diagram. In order to obtain the magnitude of the voltage V_2, the leakage inductance must be obtained from the Locked rotor test described next in part C. It is to be noted that the rotor branch is negligible due to the slip being relatively small at no load conditions, thus resulting in a low rotor current (i.e. close to 0). From the applied voltage V_2, the core loss resistance and the magnetizing inductance can be calculated as follows:

$$R_C = \frac{3V_2^2}{P_{core}} \tag{3.3}$$

$$X_m = \frac{3V_2^2}{Q_{nl}} \tag{3.4}$$

where, Q_{nl} is the reactive power (Var) quantity across the magnetizing branch under no-load condition.

3.3.3 Locked-Rotor Test

The final test for obtaining all the parameters of the equivalent circuit is the locked-rotor test, which provides information regarding the leakage inductances. Within this procedure, the rotor of the motor is locked, consequently preventing it to rotate. Hence, the slip is equal to unity with the rotor being mechanically locked. The equivalent circuit from Figure 3.3 can be simplified

considering that most of the input current will flow through X_r' and R_r' in addition to them being much smaller than the core loss resistance and the magnetizing reactance, which can be neglected in the circuit analysis. In order to complete this test, the phase voltage, line current, 3-phase input power, and source frequency are measured.

Following the procedure indicated in Method 2 of IEEE Std 112™ – 2017, the locked-rotor test is achieved under rated current conditions for three different sets of frequencies, namely at 20, 40 and 60 Hz. From these measurements, the input impedance R_{in} can be calculated using the input phase voltage and line current. Furthermore, from the respective power factor (PF) of each test case, the rotor resistance and stator leakage reactance can be determined.

$$R_r' = R_{in} - R_s \tag{3.5}$$

$$X_s + X_r{}' = \left(\frac{f_{rated}}{f_{LR}}\right) X_{LR} \tag{3.6}$$

where X_{LR} is the measured locked-rotor reactance and f_{LR} is the test case frequency. While there are no definite ways to evaluate exactly the contributions of the stator and rotor reactances independently, the IEEE Std 112™ – 2017 states that for a class B induction motor, the relation between the two is defined as [38]:

$$\frac{X_s}{X_r'} = 0.67\ . \tag{3.7}$$

Therefore, with all the information gathered through these three sets of tests, the per-phase equivalent circuit parameters shown in Figure 3.3 are summarized below in Table 3.4.

Table 3.4: The 2-hp Baldor induction motor equivalent circuit parameters.

Baldor Industrial Motor M1556T -Equivalent Circuit Parameters-	
Stator resistance $\boldsymbol{R_s}$	1.36 Ω
Stator leakage reactance $\boldsymbol{X_s}$	1.33 Ω
Core loss resistance $\boldsymbol{R_C}$	562.03 Ω
Magnetizing reactance $\boldsymbol{X_m}$	37.64 Ω
Rotor resistance referred to stator $\boldsymbol{R_r'}$	0.81 Ω
Rotor leakage reactance referred to stator $\boldsymbol{X_r'}$	1.98 Ω

The equivalent circuit parameters of the selected induction motor for this case study are then computed into the MATLAB/Simulink induction motor system block used for the ventilation fan driving system simulation model. It is to be noted that the stator resistance taken for the analysis is the cold resistance value as the driving system will be validated under no-load conditions.

3.4 Modeling of VFD

As discussed in the introduction of this chapter, the driving system of the ventilation fan induction motor is controlled using a simple open-loop scalar control scheme, from which only a reference speed signal is selected as the input for the control. For industrial supply and exhaust fan applications, the high dynamic response performance of the control is not a mandatory requirement as it would be for the driving system of an electric vehicle for example. For the Louis-Hippolyte Lafontaine tunnel case study, the ventilation system is implemented as such that the fans are to be operated at 0, 50, 66 or 100% of the rated speed. Additionally, the speed reference is applied through a speed command change by the tunnel operator. Using the open-loop scalar control scheme does not allow for accurate speed control as only the synchronous speed, or frequency, can be controlled. However, based on the induction motor theory, the rotor speed of the motor is lower than the synchronous speed due to the slip, thus resulting in a lower speed control accuracy.

For the purpose of this case study, the driving system prototype is implemented in the laboratory-based on the two-level inverter topology design. Thus, the driving inverter is composed first of a full bridge diode rectifier that is converting the supply AC to DC, secondly of a DC link capacitor used for limiting the voltage variations under load changes and finally of a two-level IGBT based inverter that is converting the voltage from DC to AC at a given voltage amplitude and frequency. The drive model is implemented in the MATLAB/Simulink environment using the machine parameters determined using the IEEE Std 112^{TM} – 2017 and then validated experimentally. The results of this analysis are shown in the latter section of this chapter.

The theory behind V/f, or scalar control, relies on the concept that the flux density of the induction motor remains constant below the rated frequency. Indeed, while neglecting the voltage drop across the stator resistance, the air-gap quantity of the stator voltage is proportional to the electrical frequency and the peak flux density as [42]:

$$V_s = \left(\frac{\omega_e}{\omega_{rated}}\right)\left(\frac{B_{peak}}{B_{rated}}\right)V_{rated} \tag{3.8}$$

with Vs being the stator supplied voltage, ω_e the electrical frequency, B_{peak} the peak air-gap flux density and ω_{rated}, B_{rated} and V_{rated} are the rated quantities of the machine. Thus, by maintaining the flux to its constant rated value (i.e. $B_{peak} = B_{rated}$), Equation 3.8 can be re-written as follows:

$$\frac{V_s}{\omega_e} = \frac{V_{rated}}{\omega_{rated}}. \tag{3.9}$$

As such, the flux of the induction machine is kept constant below the rated frequency, while also maintaining a constant ratio between the applied stator voltage and operating frequency.

Moreover, in the drive system design, a boost voltage must be included in the control system as a means to overcome the low frequency effect of the stator resistance voltage drop that can no longer be neglected in the analysis. The simplest way, although not the most accurate way to compensate, is to boost the stator voltage by the magnitude of the product between the stator resistance and the full-load current magnitude of the induction motor [35]. Incorporating the boost voltage to the drive control system is allowing the flux to be at its rated value, hence enabling full torque at a lower speed (i.e. lower frequency). The intent of incorporating a constant boost voltage is shown in Figure 3.5.

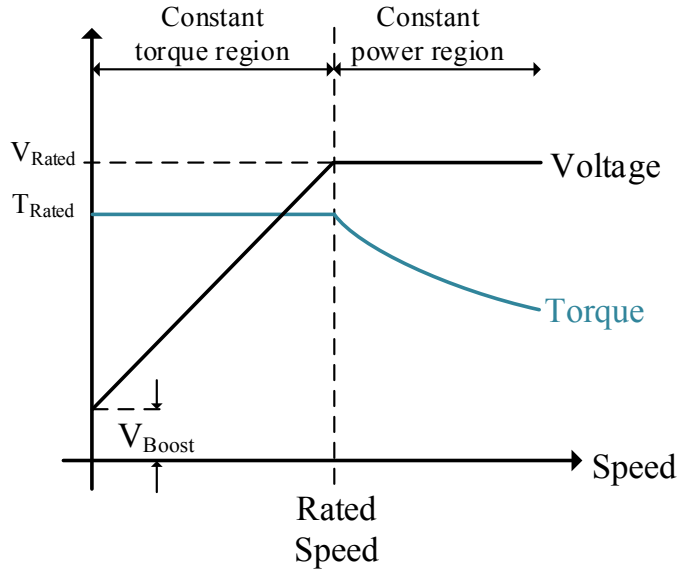

Figure 3.5: Open-loop scalar (V/f) control with constant boost voltage.

Consequently, for the purpose of the modeling process of this drive control system, the boost voltage is estimated as follow:

$$V_{Boost} = I_{full-load} \times R_s = 6.1 \times 1.3575 = 8.28\,V\,. \tag{3.11}$$

Therefore, based on the 2-hp induction motor parameters shown in Table 3.1 and selected for this case study, the V/f ratio can be calculated as:

$$\frac{V_s - V_{Boost}}{\omega_e} = \frac{120\,V - 8.28V}{2 \times \pi \times 60} = 0.296\,. \tag{3.10}$$

As illustrated in Figure 3.5, the V/f ratio corresponds to the slope of the stator voltage versus frequency curve. With the constant parameters determined for the motor driving system that are the boost voltage and the V/f ratio, the complete control block diagram of the open-loop scalar control system is shown in Figure 3.6. It is to be noted that the considered V_{Boost} and V_s^* values are phase RMS quantities. Furthermore, with the motor running below the rated speed, the system is said to be operating in the constant torque region, whereas above rated speed, it is operating in the constant power region. Indeed, when operating below rated speed, the flux is maintained constant in the scalar control scheme. Consequently, the maximum torque will then be kept constant for the same operating range. Once above the rated speed, the voltage is kept constant and the torque is decreasing with an increase in the speed.

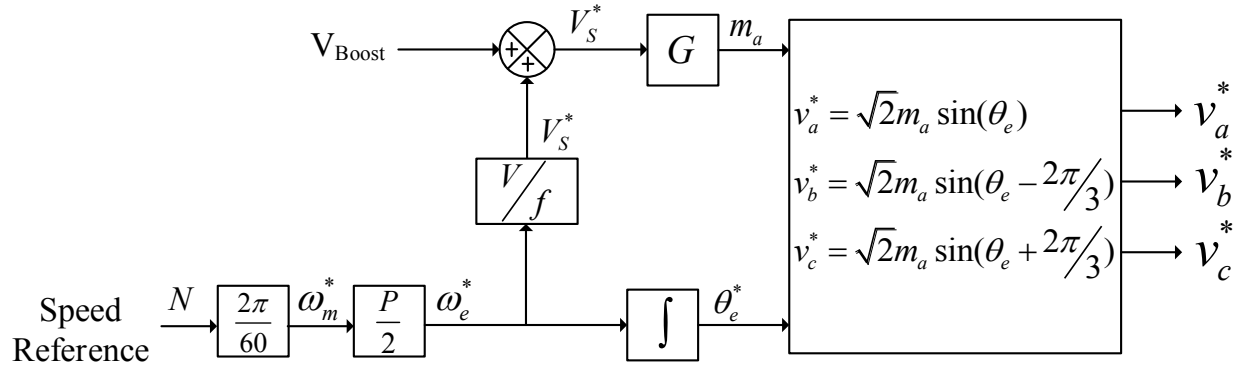

Figure 3.6: Open-loop scalar (V/f) control block diagram for an induction motor driving system.

From Figure 3.6, the variable that can be controlled is the synchronous speed in RPM, or the frequency. It is then converted to the mechanical angular velocity in rad/s. Following this transformation, the number of poles is taken into consideration in the conversion to the equivalent electrical angular velocity based on the following relation:

$$\omega_e^* = \frac{P}{2}\omega_m^* \tag{3.11}$$

where, ω_e^* is the reference electrical angular velocity, ω_m^* is the reference mechanical angular velocity and P is the number of poles in the induction motor.

The electrical angle can then be extracted by taking the integral of the electrical angular velocity. Hence, the calculated angle is used to generate the three-phase reference voltage used for the speed control of the induction motor. The amplitude of the control voltages must be between 0 and 1 in order to avoid overmodulation of the system. To do so, the modulation index m_a is determined by normalizing the value of V_s^* as such:

$$m_a = \frac{V_s^* \times 2 \times \sqrt{2}}{V_{DC}} \tag{3.12}$$

where the value of V_{DC} is given by:

$$V_{DC} = V_{LL} \times \sqrt{2} = 208 \times \sqrt{2} = 294.16\,V \tag{3.13}$$

where V_{LL} represents the supply grid voltage at the three-phase rectifier input.

The three-phase reference signals are then calculated as:

$$v_a^* = \sqrt{2} \times m_a \sin(\theta_e) \tag{3.14}$$

$$v_b^* = \sqrt{2} \times m_a \sin(\theta_e - {}^{2\pi}/_{3}) \tag{3.15}$$

$$v_c^* = \sqrt{2} \times m_a \sin\left(\theta_e + {}^{2\pi}/_{3}\right). \tag{3.16}$$

The three-phase control reference signals are then used to generate the gating pulse to the two-level inverter IGBT switches.

With the limitations imposed by the laboratory AC supply, which is limited to a line-to-line RMS voltage of 208V, the maximum available DC bus voltage that can be obtained across the DC

link capacitor can be calculated as 294.16 V. However, this DC bus voltage limit does not allow for a full range of operation of the induction motor. Indeed, overmodulation is occurring with the machine running in the upper frequency range when using sinusoidal pulse width modulation (SPWM) scheme. Indeed, within the SPWM modulation technique, the modulation index should then be between 0 and 1 and the maximum RMS line-to-line voltage that can be met under those limitations is 180.14 V, which is consequently meeting only 86.6% of the desired induction motor operating range. Hence, the control system is exiting the linear region of operation with the motor operating at higher frequency. As such, with the system running at a higher speed, low order harmonics are introduced in the system. In Figure 3.7, overmodulation occurs when operating the machine at the synchronous speed of 1800 RPM and the effects are circled in black in the inverter switching output pole voltage.

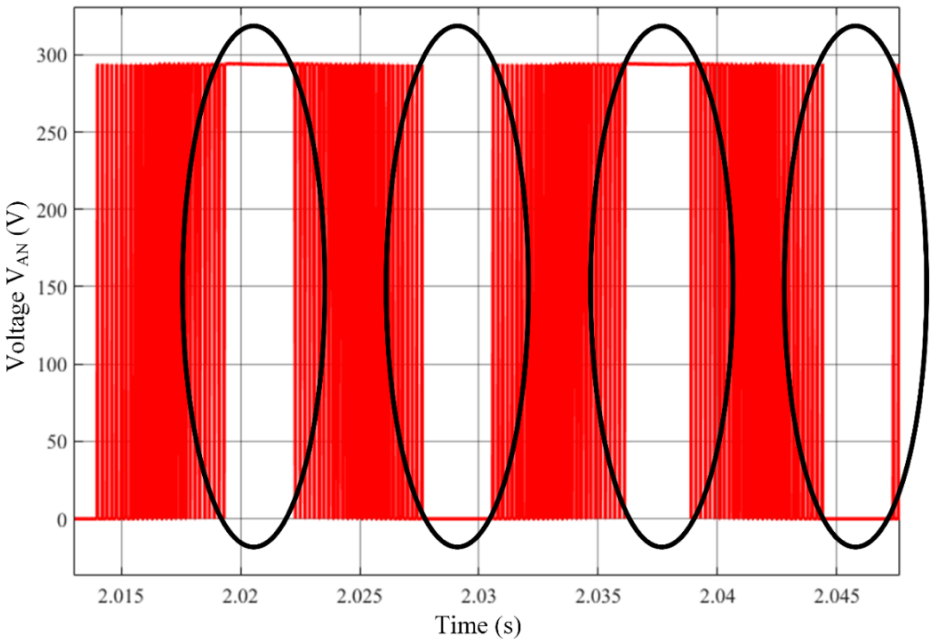

Figure 3.7: Overmodulation seen in the inverter pole voltage.

Moreover, a DC bus voltage magnitude of 339.66V would be required to allow a complete operation of the induction motor. Indeed, based on the limitations imposed by the laboratory rating and the sinusoidal pulse width modulation (SPWM) linear region limited to a modulation index of 1, an alternative modulating approach should be taken to overcome these limitations and avoid overmodulation. Consequently, the method used consists of injecting to the sinusoidal reference

signal a triangular third harmonic component using the min/max zero sequence, from which an improvement of 15.47% is seen in regards to the utilization ratio of the DC bus voltage [44, 45, 46]. The injection of the third harmonic component has no impact on the signal applied on the machine as the third harmonic components are canceled in the inverter output line voltage and current in a balanced three-phase system [47]. Henceforth, an additional control block is added to the control system shown in Figure 3.6 to which the min/max zero sequence is subtracted from the sinusoidal reference initially generated. The new reference control voltages are generated using the following relations:

$$v_{min/max} = \frac{\min(v_a^*, v_b^*, v_c^*) + \max(v_a^*, v_b^*, v_c^*)}{2} \tag{3.17}$$

$$v_{a\_new}^* = v_a^* - v_{min/max} \tag{3.18}$$

$$v_{b\_new}^* = v_b^* - v_{min/max} \tag{3.19}$$

$$v_{c\_new}^* = v_c^* - v_{min/max}\,. \tag{3.20}$$

By generating these modified control voltages, the enhanced gain allows for a better utilization rate of the DC bus voltage, which results in extending the modulation linear region enough for the induction motor to operate at rated speed without encountering any overmodulation in the control.

3.5 Developed Drive System (AC-DC-AC Converter) Parameters

The drive system used for the induction motor speed control has been developed entirely in the laboratory. The first stage of the system is consisting in the transition from AC to DC through a diode bridge rectifier. The voltage is then filtered through the DC link capacitors. The final conversion from DC to AC is achieved through the IGBT switches, which are controlled by the gate drivers. The implemented drive system for experimentation is shown in Figure 3.8. The components used for the making of the prototype are summarized in Table 3.5.

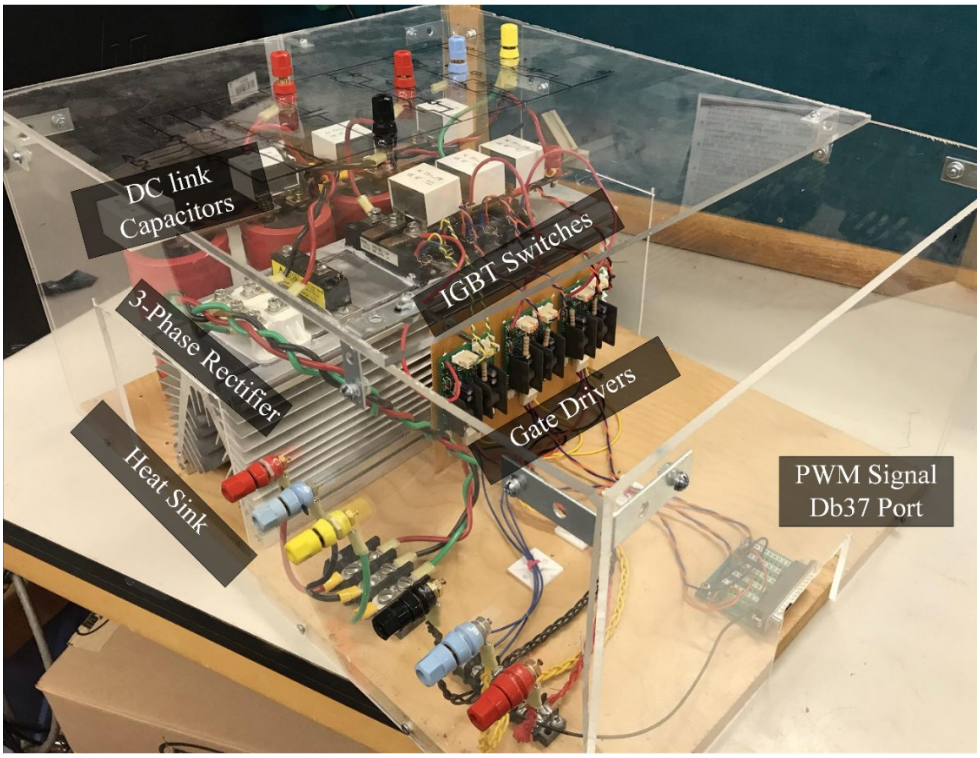

Figure 3.8: Drive system (AC-DC-AC converter) built experimentally.

Table 3.5: Selected drive components.

Component	Manufacturer	Ratings
3-Phase Bridge Rectifier	Micro Commercial Components *MD50S16M4*	1600 V, 50 A
IGBT Switch	Fuji Electric *2MBI60L-120*	1200 V, 50 A
Gate Drive Board	Powerex BG2B	Logic source V_L = 5V Supply Source *Vs* = 15V
DC link Capacitor	EAP 362T350X5L3PH	C = 3.6 mF 700 V
PWM Signal Generator	dSPACE DS1103 Controller Board	N/A

In order to limit the voltage ripple on the DC link, the capacitance should be large enough to maintain constant the DC bus voltage. Ideally, the capacitors should be sized accordingly to remove the 6th harmonic generated from the rectifier, thus limiting the ripple. Additionally, from the implemented drive system, the DC link is configured as such that two capacitors are connected in series to increase the DC voltage capability from 350 to 700 V.

The theoretical maximum power capability of the drive can also be determined based on the ratings of the different components selected for the implementation of the system. Indeed, due to the $L\frac{dI}{dt}$ spikes, the limitations imposed on the DC bus voltage is corresponding to 50% of the IGBT rated value. Hence, the maximum voltage would be 600 V. The theoretical power capability of this converter can be determined as such:

$$S = \sqrt{3}\left(\frac{300}{\sqrt{2}} * \sqrt{3}\right) * \left(\frac{50}{\sqrt{2}}\right) = 22,500\,VA\,. \tag{3.21}$$

3.6 Validation of the Induction Motor Drive System

The drive model for the 2-hp induction motor is first implemented in MATLAB/Simulink environment software using the extracted parameters from the equivalent circuit of the induction motor. The validation procedure involved the operation of the motor at different speed values to observe first if the V/f ratio is respecting the theoretical ratio determined based on the rated parameters of the selected machine, which has been evaluated to be of 0.296. Furthermore, the scalar control has been tested for a sudden speed change command as a means to evaluate and analyze the drive system response in order to investigate the dynamic performance of the whole drive system. The driving system model that has been implemented in the Simulink environment is shown in Figure 3.9.

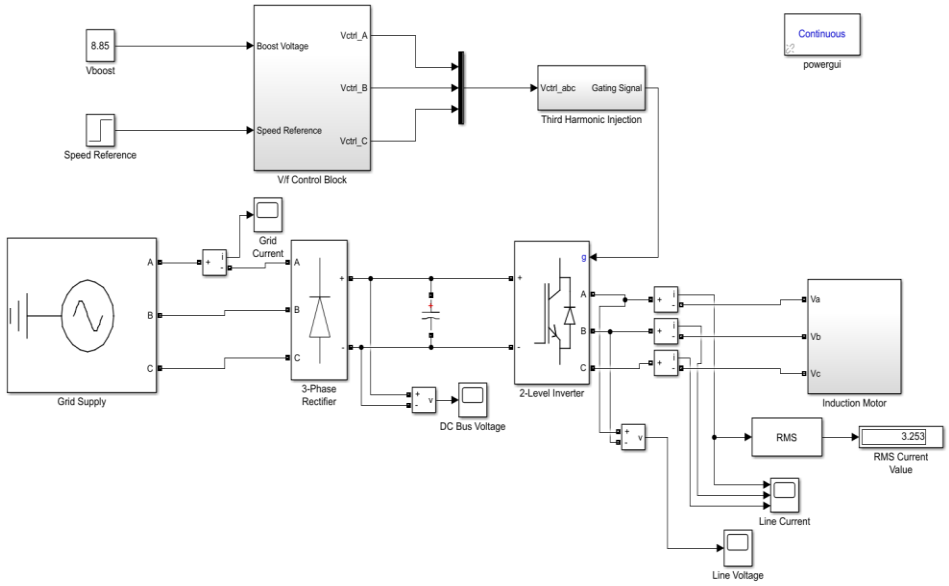

Figure 3.9: Simulink model for an induction motor drive system.

Following the validation process of the drive model through simulation, the system is then tested experimentally on the actual motor using an AC-DC-AC power converter developed in the laboratory and run as a drive. The same procedure used in simulation has been followed for the experimental process. The experimental V/f ratio is determined and the speed response to speed command changes are analyzed. The scalar control system is implemented using the dSPACE real-time simulation environment and DS1103 Controller Board. Furthermore, it is to be noted that the system is tested at no-load conditions both in the simulation and experimentally. The implemented experimental setup is shown in Figure 3.10.

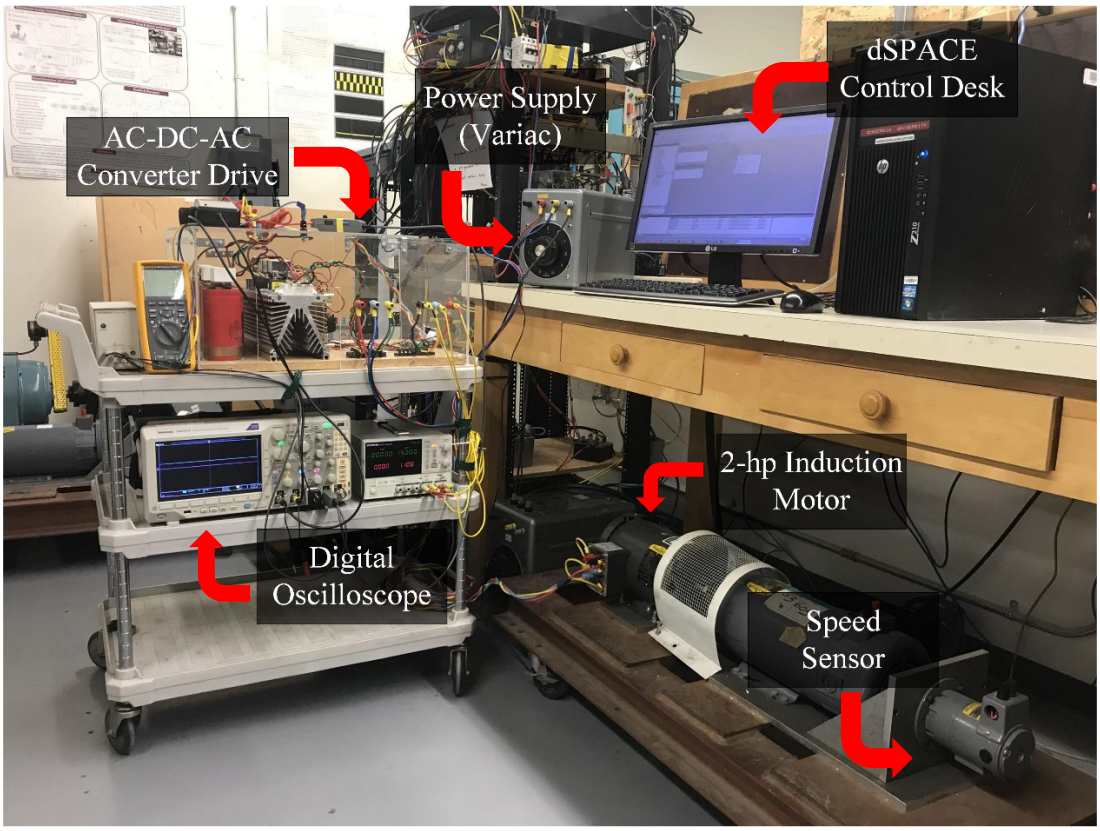

Figure 3.10: V/f controlled drive experimental setup.

3.6.1 Validation of Constant V/f Ratio

To validate the V/f constant ratio of the induction motor drive model, the system is tested for frequencies of 1, 2, 5, 10, 20, 30, 40, 50 and 60 Hz, corresponding respectively to 30, 60, 150, 300, 600, 900, 1200, 1500 and 1800 RPM. Measurements have been taken at low frequency to observe

the controller response for the conditions where the voltage drop across the stator resistance is no longer negligible. Within this procedure, the RMS value of the inverter fundamental output line-to-line voltage is extracted using the fast Fourier transform (FFT) feature in Simulink, which is taken directly for the simulation procedure. In order to obtain the RMS value of the experimental switching line-to-line voltage, the measured data is extracted from the digital oscilloscope. The data is then uploaded in MATLAB as a means to reconstruct the signal measured experimentally. Then, the FFT function is used to determine the RMS value of the fundamental component of the measured voltage as well as other high order harmonics. For both the simulation and experimental analysis, the fundamental phase voltage is calculated and based on the corresponding frequency at which the machine is operating, determined using the line current signal or the rotational speed of the motor, the V/f ratio can then be computed.

In regards to the simulation procedure, a switching frequency of 5 kHz is used for the control of the inverter. Additionally, for the Simulink model, a sampling period of 1μs is selected for higher resolution. In order to calculate the V/f ratio from the simulated model, an average value is extracted from all three phases of the system (A, B and C). In Figure 3.11, the three-phase control voltages resulting from a speed command set for a reference of 1800 RPM are shown.

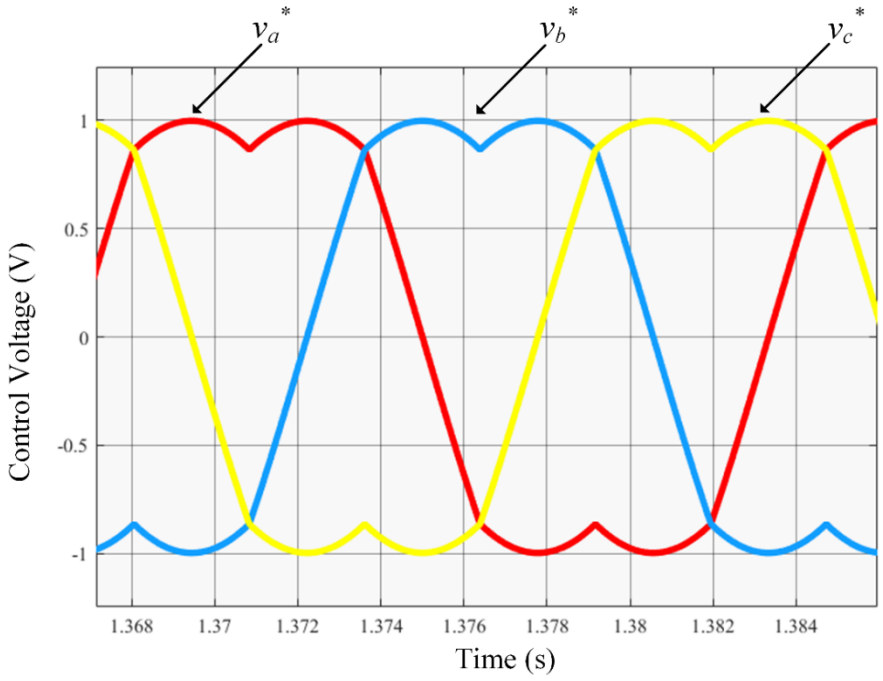

Figure 3.11: Three-phase control voltages with the reference speed set at 1800 RPM.

As illustrated from Figure 3.11, the amplitudes of the reference control voltages are close to unity with the induction machine running at its rated voltages, thus avoiding any overmodulation occurrence. Hence, the complete operating range of the motor is occurring in the linear region of modulation, a direct result of the triangular third harmonic injection in the control system. To illustrate the complete operating range of the control system implemented for the drive, the inverter output line currents and line-to-line voltage waveforms are taken in simulation and experimentally for frequencies between 1 and 60 Hz. However, only the measured waveforms for 10 and 60 Hz taken in simulation and experimentally are shown in this thesis.

a) Operation at 10 Hz

With the reference voltage computed accordingly to the reference speed given, the average phase voltage at the output of the inverter is measured for multiple frequencies. The scope of this analysis is to extract the V/f curve from both the simulation and experimentation. Following the simulation validation, the waveforms illustrating the actual machine rotating speed superimposed with the reference speed when operating at 10 Hz, line-to-line inverter output voltage and DC bus voltage, and the three line currents are shown respectively in Figure 3.12 (a), (b) and (c).

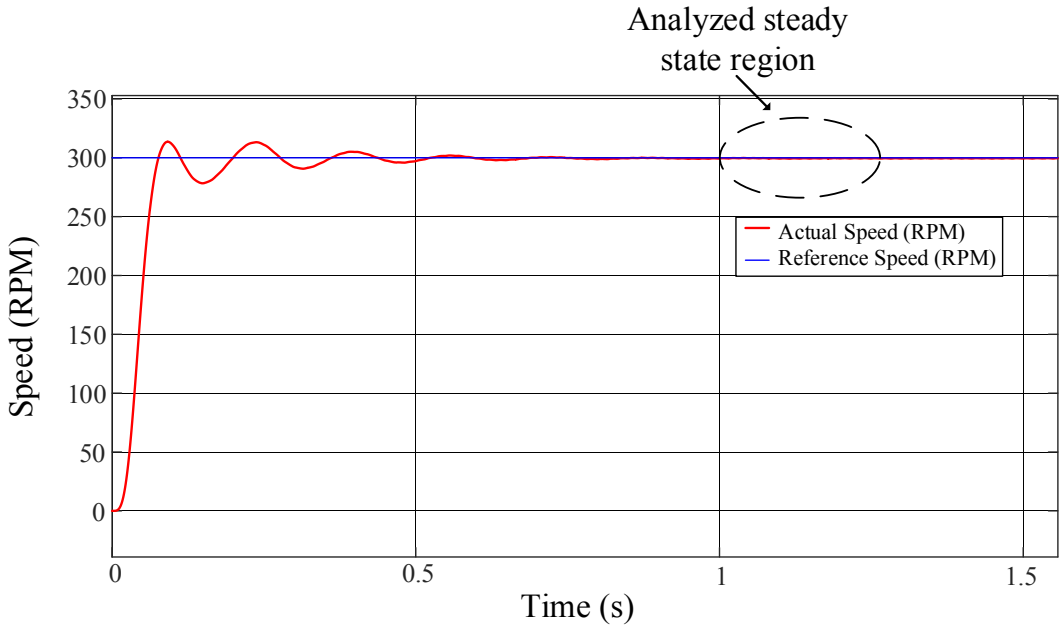

(a)

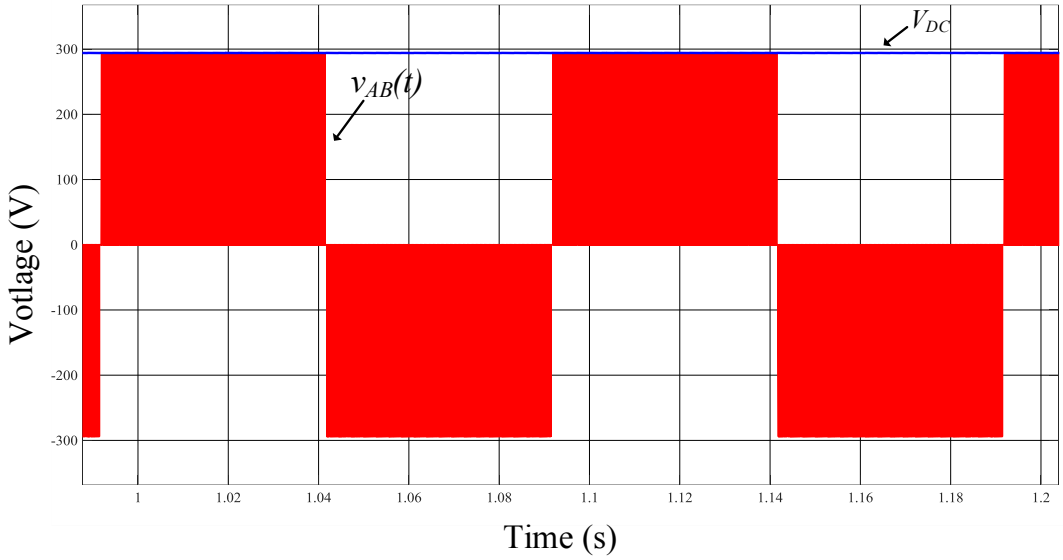

(b)

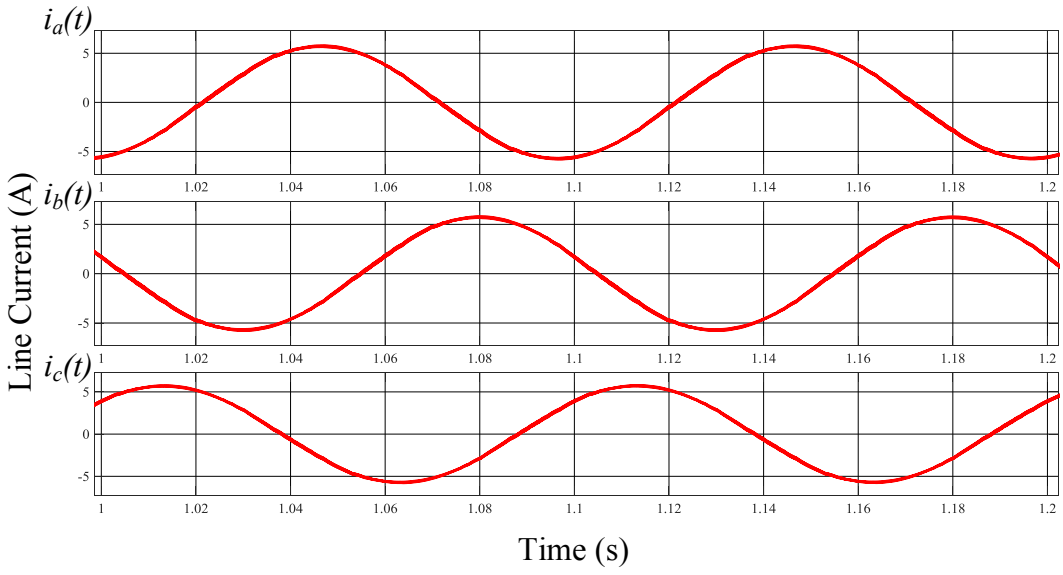

(c)

Figure 3.12: Motor operating at 10 Hz: (a) Induction motor actual rotational speed superimposed with the reference speed, (b) Line-to-line inverter output voltage and DC bus voltage, and (c) Inverter output line current.

As it can be seen from Figure 3.12 (a), the steady-state operation of the motor is settling closely to 300 RPM after close to 0.6s of transients. From both the line currents and line-to-line voltage waveforms, it can be observed that one period of the signal is corresponding to 0.1s. As such, the frequency of the fundamental component of the switching line-to-line voltage and the line current can be calculated as 10 Hz, which follows the reference speed signal of 300 RPM for a 4-poles

induction motor. Furthermore, as expected, the amplitude of the switching line-to-line voltage is equal to the magnitude of the voltage across the DC link capacitor of the inverter. To calculate the fundamental component of the line voltage, the fundamental component at 10 Hz is extracted through the FFT analysis of the signal, for which the harmonic spectrum is shown in Figure 3.13. As it can be observed, the THD level of the inverter output voltage is considerably high at 216.18% due to the magnitude of the 10 Hz fundamental component of the line voltage being small. From the spectrum, harmonics are located around the sidebands of the switching frequency and its multiple.

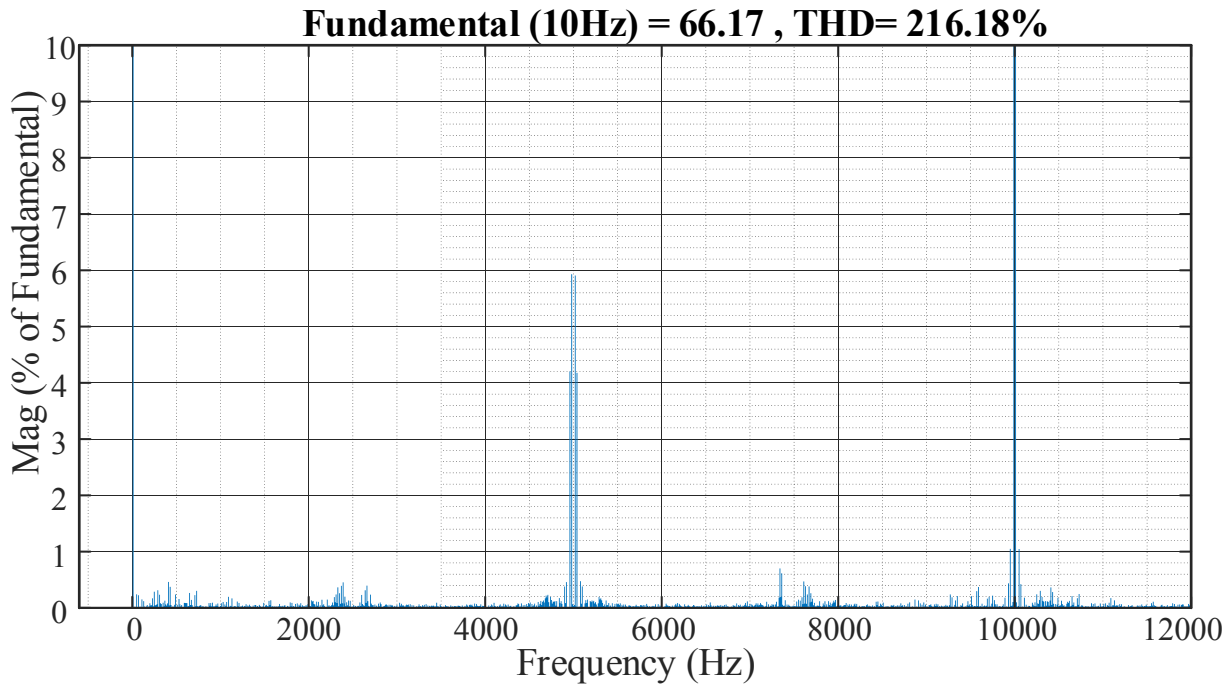

Figure 3.13: Harmonic spectrum of the simulated line voltage V_{AB} at the output of the drive when operating at 300 RPM.

For the experimental process, the same control technique used in the simulation has been implemented in the dSPACE/Simulink environment. The speed command is given through the dSPACE control desk The voltage and current measurements are taken once the machine reaches the steady state condition. As for the speed measurements, they have been taken using two different methods. In the first technique, the speed has been measured by using the Omega HHT13 laser tachometer. The second method has involved the DC voltage measurement across the terminals of

the speed sensor coupled to the induction motor, for which the gain has been calculated and set to be 50Vdc/1000RPM. The average speed is taken between these two methods. To illustrate the experimental operation of the system, the line-to-line voltage V_{AB} and the line current I_A waveforms at steady state are plotted together on the oscilloscope in Figure 3.14. Additionally, the three line currents I_A, I_B and I_A are shown in Figure 3.15.

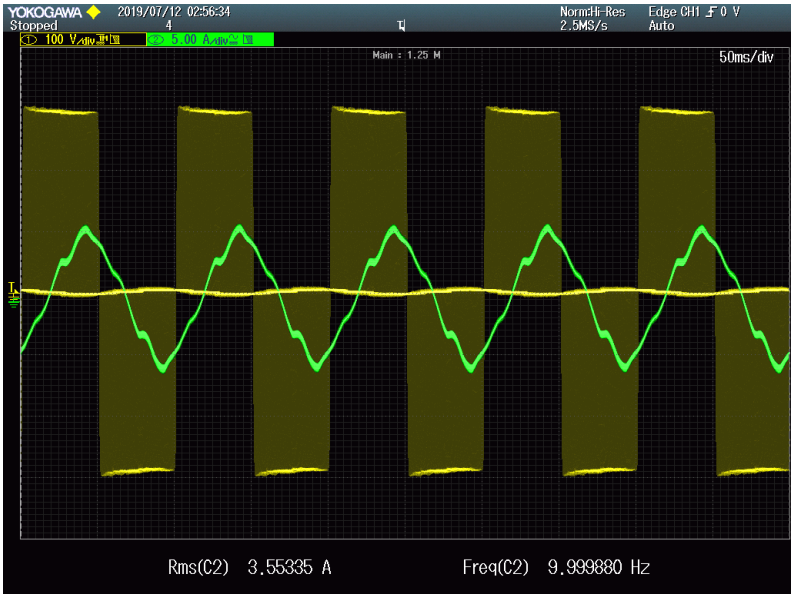

Figure 3.14: Line voltage V_{AB} and current I_A with the motor operating at 10 Hz.

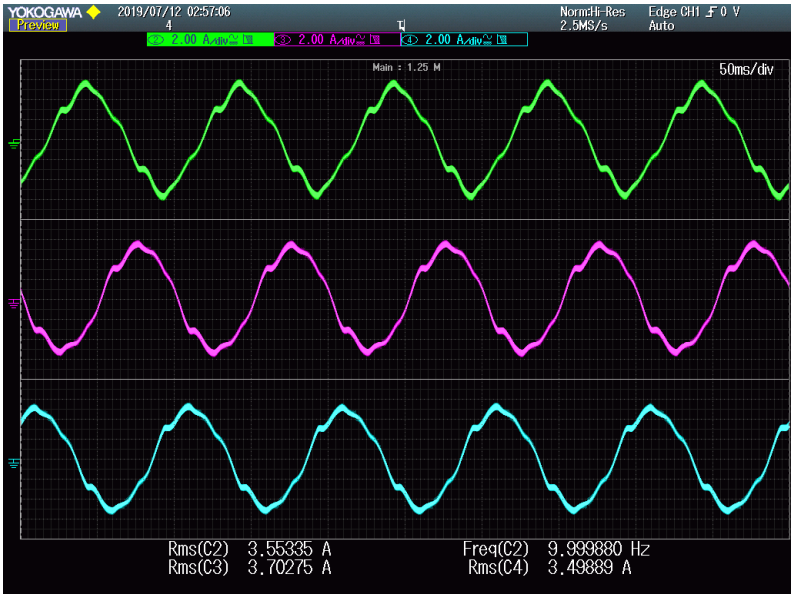

Figure 3.15: Line Currents I_A, I_B, and I_C with the motor operating at 10 Hz.

As can be observed in Figure 3.14 and Figure 3.15, when operating at low frequency, the line currents at the output of the inverter are not purely sinusoidal. However, the measured currents are following the constraint imposed by the controller as they are phase-shifted by +/- 2π/3 rad with a fundamental frequency close to 10 Hz. As for the line-to-line voltage, its amplitude is following the voltage ripple across the dc-link capacitor. In order to get clearer images for the experimental results, a lower bandwidth is imposed on the oscilloscope to remove the high switching harmonics and limit the noise on the signal waveform.

Moreover, as completed for the simulation, the fundamental component of the inverter output line voltage is extracted using the FFT tool of Simulink. The harmonic spectrum of the measured signal is shown in Figure 3.16 and is comparable to the simulated spectrum shown in Figure 3.13. However, one can see the impact of dead time in the experimental spectrum with the presence of the 5^{th} and 7^{th} harmonics.

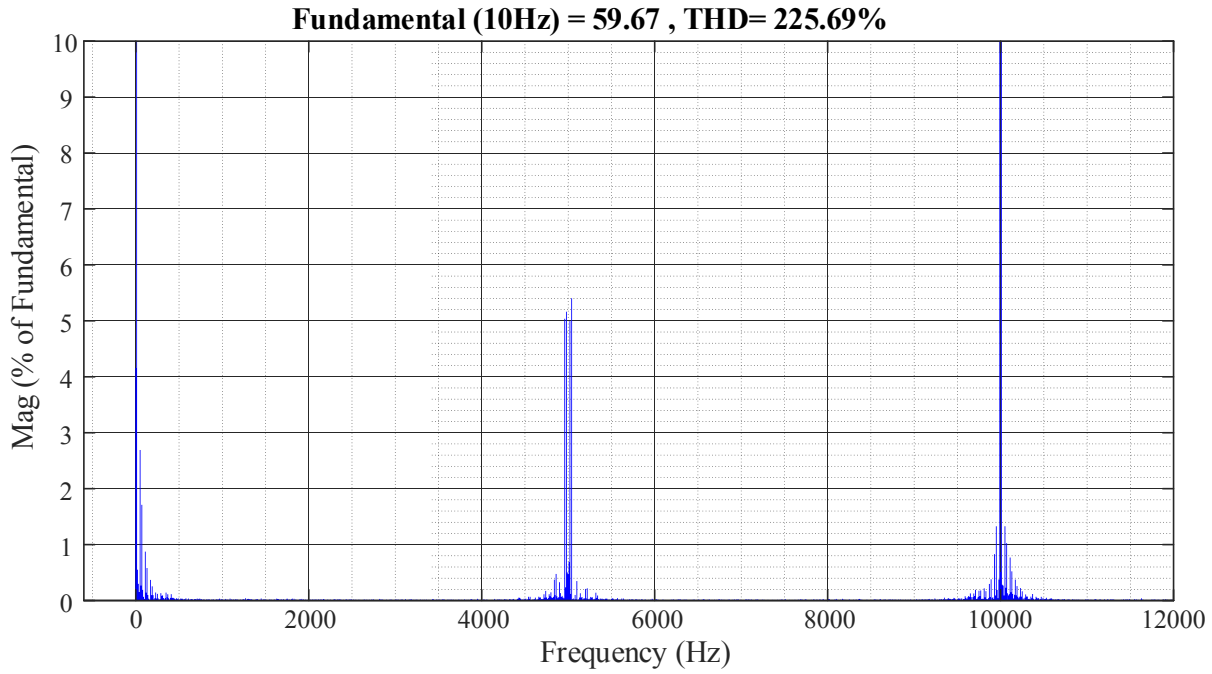

Figure 3.16: Harmonic spectrum of the experimentally measured line voltage VAB at the output of the drive when operating at 300 RPM.

b) Operation at 60 Hz

To illustrate the full operating range of the drive control system for which the rated speed of the induction motor occurs once the machine is running at 60 Hz, the inverter output line currents and line-to-line voltage waveforms are taken in simulation and experimentally. The waveforms, obtained from simulation, for the line-to-line inverter output voltage and the DC bus voltage, the line currents and the machine rotating speed when operating at 60 Hz are shown respectively in Figure 3.17 (a), (b) and (c).

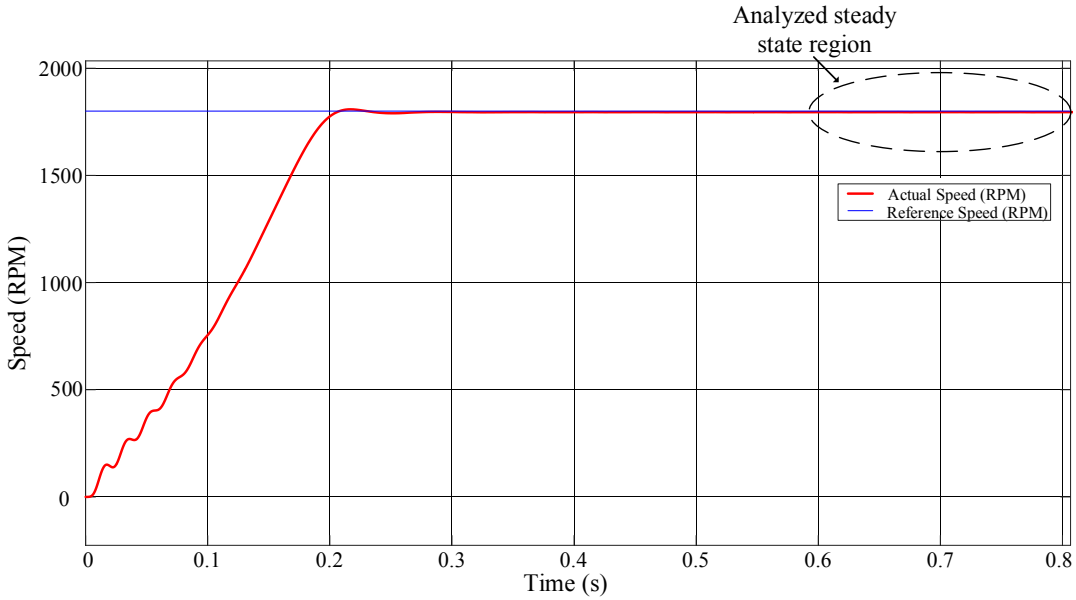

(a)

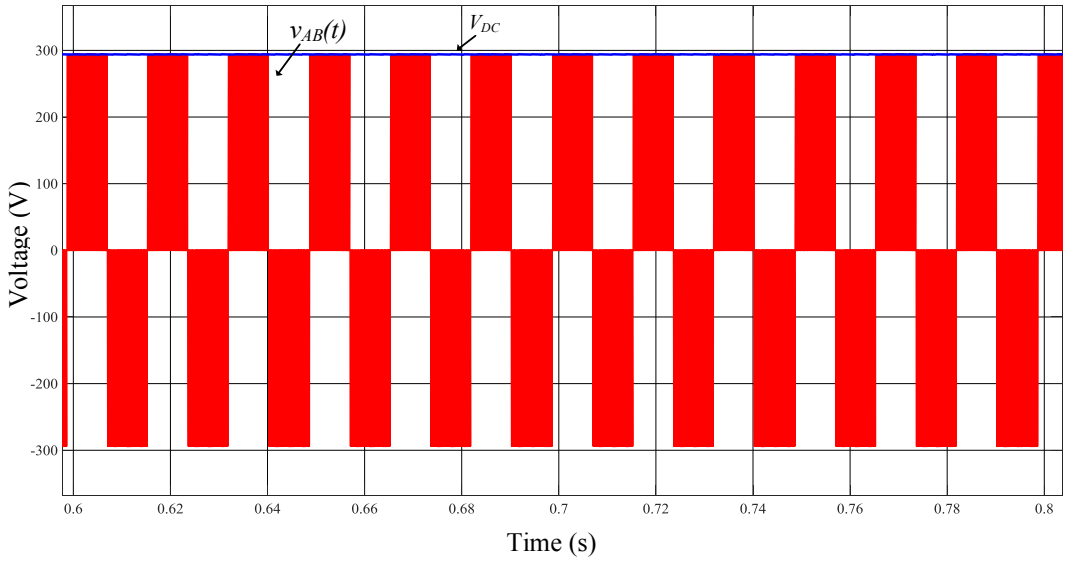

(b)

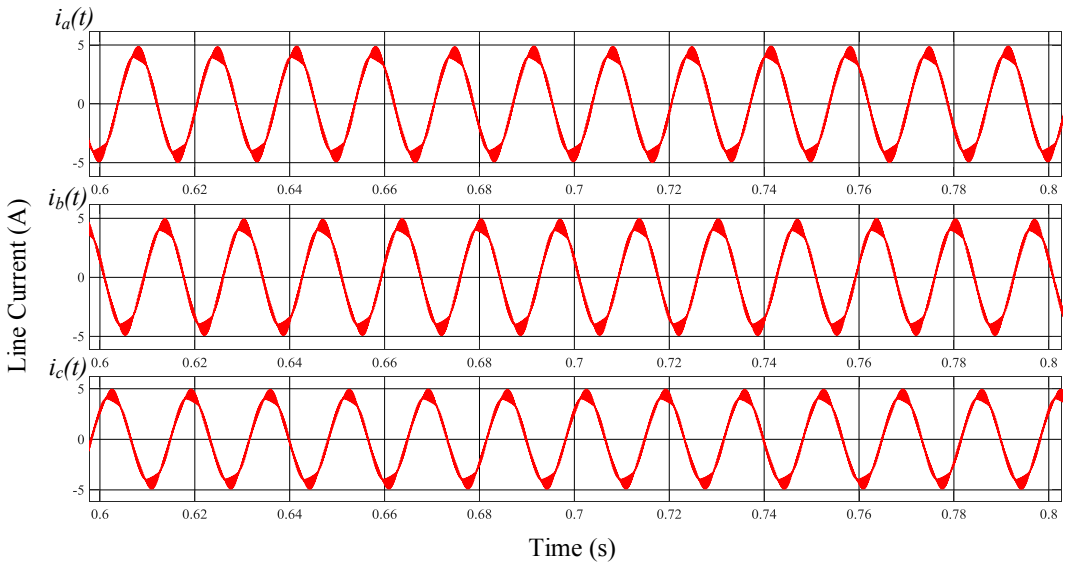

(c)

Figure 3.17: Motor operating at 60 Hz: (a) Induction motor actual rotational speed superimposed with the reference speed, (b) Line-to-line inverter output voltage and DC bus voltage, and (c) Inverter output line current.

As can be observed from Figure 3.16 (c), the steady-state operation of the motor is settling at 1792 RPM after only close to 0.75 s of a transient condition. From both the line currents and line-to-line voltage waveforms of Figure 3.16 (a) and (b), it can be seen that there are close to 3 complete cycles within 0.05 s. As such, the fundamental operating frequency can then be estimated as 60 Hz, which is corresponding to the speed reference of 1800 RPM. As it has been observed with the machine operating at 10 Hz, the amplitude of the switching line-to-line voltage follows the voltage ripple across the DC link capacitor of the inverter.

Moreover, as achieved for the machine operating at 10 Hz, the fundamental component of the inverter output line voltage is extracted using the FFT tool from Simulink. The resulting harmonic spectrum is shown in Figure 3.18. As can be seen, with the machine operating at rated voltage, the magnitude of the switching frequency harmonic sidebands is increasing compared to when the machine is operating at a lower speed.

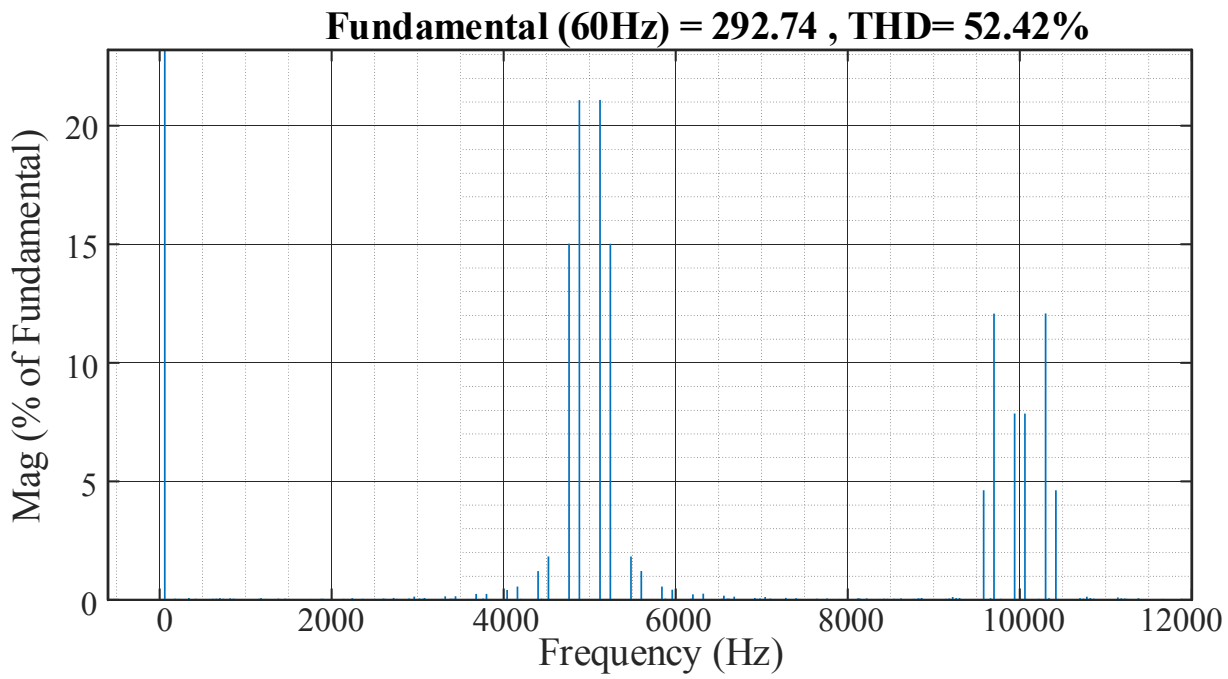

Figure 3.18: Harmonic spectrum of the simulated line voltage VAB at the output of the drive when operating at 1800 RPM.

Then, following the simulation process, the performance of the drive control system is observed for the induction motor running at the rated voltage and no-load conditions experimentally with the induction motor running at 1800 RPM. Again, the same analysis process achieved for 10 Hz is followed for 60 Hz. As such, the line-to-line voltage V_{AB} and line current I_A are plotted together on the oscilloscope as shown in Figure 3.19. Additionally, the three measured line currents I_A, I_B and I_A are shown in Figure 3.20.

Figure 3.19: Line voltage V_{AB} and current I_A with the motor operating at 60 Hz.

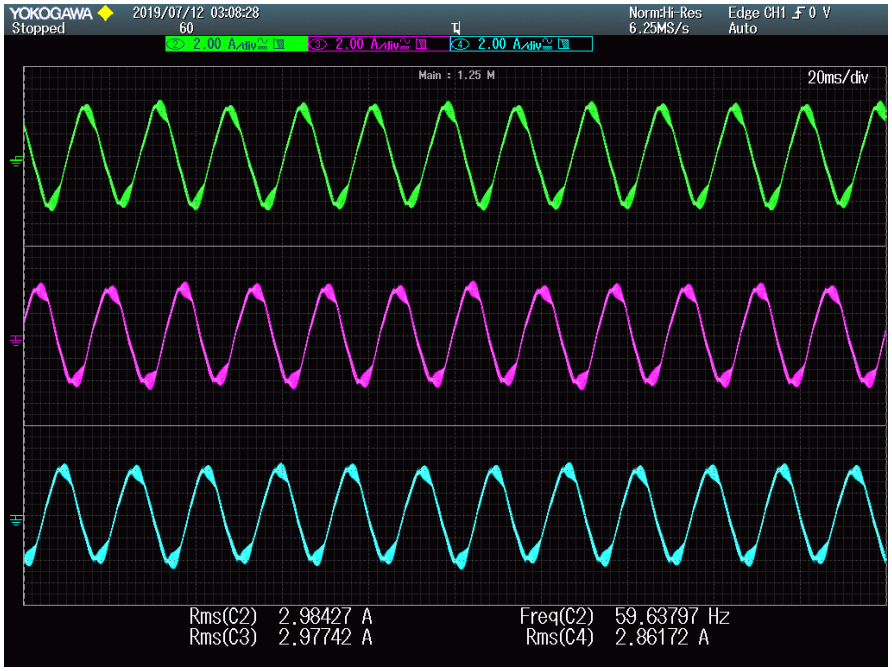

Figure 3.20: Line Currents I_A, I_B , and I_C with the motor operating at 60 Hz.

Similar observations to those made for the motor operating at 10 Hz are also valid for the machine running at 60 Hz. Indeed, the line-to-line voltage amplitude is following the voltage ripple across the dc-link capacitor. Furthermore, from Figure 3.19 and Figure 3.20, it can be observed that the measured signal parameters are corresponding to the constraints imposed by the reference signal, with the current signal following more closely the sinusoidal waveform. The current frequency is relatively close to the 60 Hz signal. Additionally, the fundamental component of the inverter output line-to-line voltage is also at 60 Hz. Again, the bandwidth of the oscilloscope has been reduced for the current signals in order to remove the noise and high order switching harmonics to get a signal closer to the fundamental component of 60 Hz.

The fundamental component of the inverter output line voltage is then extracted using the FFT tool in order to complete the complete V/f curve of the induction machine. The harmonic spectrum for the machine operating at 1800 RPM is shown in Figure 3.21. Again, the effect of the dead time can be seen from the presence of the 5^{th} and 7^{th} harmonic. However, at 60 Hz, their magnitudes are lower due to the fundamental component being larger.

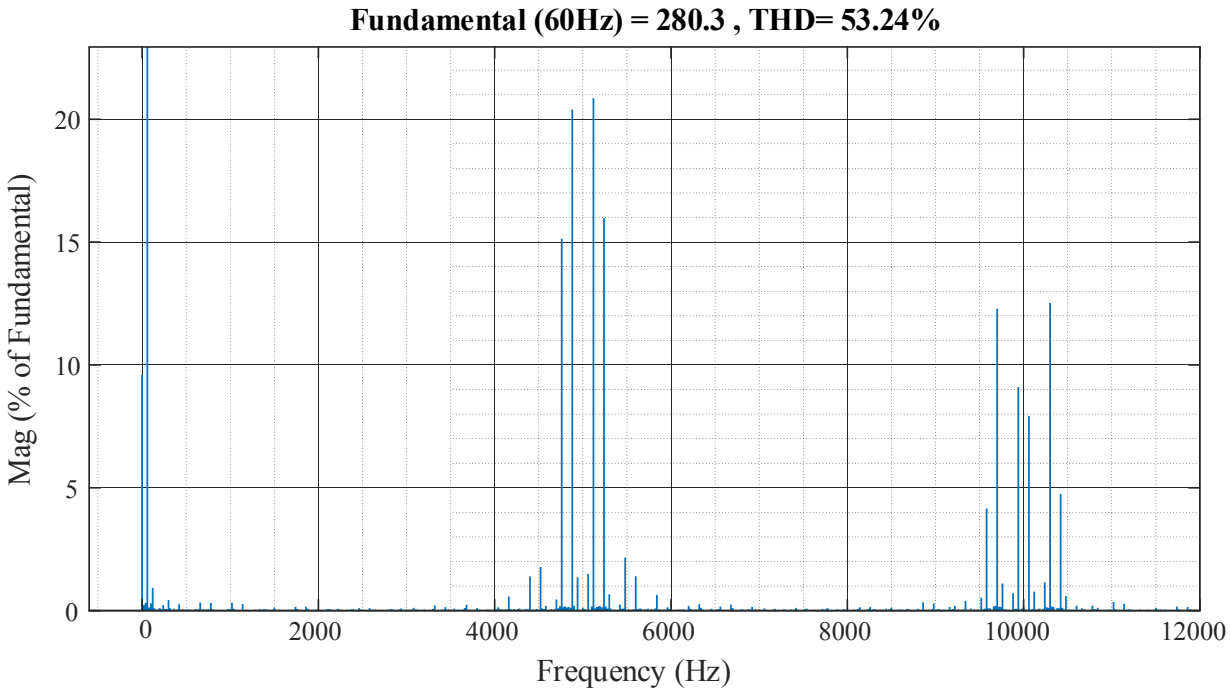

Figure 3.21: Harmonic spectrum of the experimentally measured line voltage VAB at the output of the drive when operating at 1800 RPM.

c) Analysis and summary of all measurements

The process has been repeated for frequencies of 1, 2, 5, 10, 20, 30, 40, 50 and 60 Hz in order to get the most accurate V/f profile in simulation and experimentally. Measurements have been taken at low frequencies (i.e. 1, 2 and 5 Hz) to see the controller response as for this operating region, the assumptions made in the controller design are not fully valid since the voltage drop across the stator resistance is no longer negligible. In order to implement the V/f curve, the inverter output line-to-line voltage is measured for $V_{AB,}$ V_{BC}, and V_{CA} from which the phase voltages are extracted. The average value of the independent phase voltages is then taken to plot the V/f curve. For the experimental procedure, the measured line-to-line voltage waveform is extracted from the oscilloscope and reconstructed in MATLAB to determine its fundamental component. The quantities measured in simulation and experimentally for the phase voltage and the rotational speed of the motor are summarized in Table 3.6. It is to be noted that all the tabulated values are RMS quantities.

Table 3.6: Simulation and experimental measurements for the phase voltage and rotational speed of the motor.

	Simulation		**Experimentation**	
Reference Speed (RPM)	Average Phase Voltage (V)	Measured Speed (RPM)	Average Phase Voltage (V)	Measured Speed (RPM)
30	10.36	30.90	5.85	28.90
60	11.35	60	7.94	59.80
150	17.77	150	14.09	149.50
300	27.01	299	24.29	298.54
600	45.20	598	42.67	598.19
900	64.03	897	60.81	898.12
1200	82.73	1195	78.79	1196.13
1500	101.29	1494	96.34	1495.27
1800	119.63	1792	114.22	1794.60

From Table 3.6, the scalar control V/f curve is computed using the measured RMS phase voltage and the operating frequency of the induction motor for both the simulation and experimental results. Theoretically, within the scalar control, the machine flux should be

maintained constant for the full operating range of the machine (i.e. below the rated frequency of 60 Hz). Consequently, for this to happen, the applied phase voltage needs to vary accordingly with the frequency as such that the ratio between the two is maintained constant. The computed V/f curves for both the simulation and experimental results are shown in Figure 3.22 and Figure 3.23, respectively.

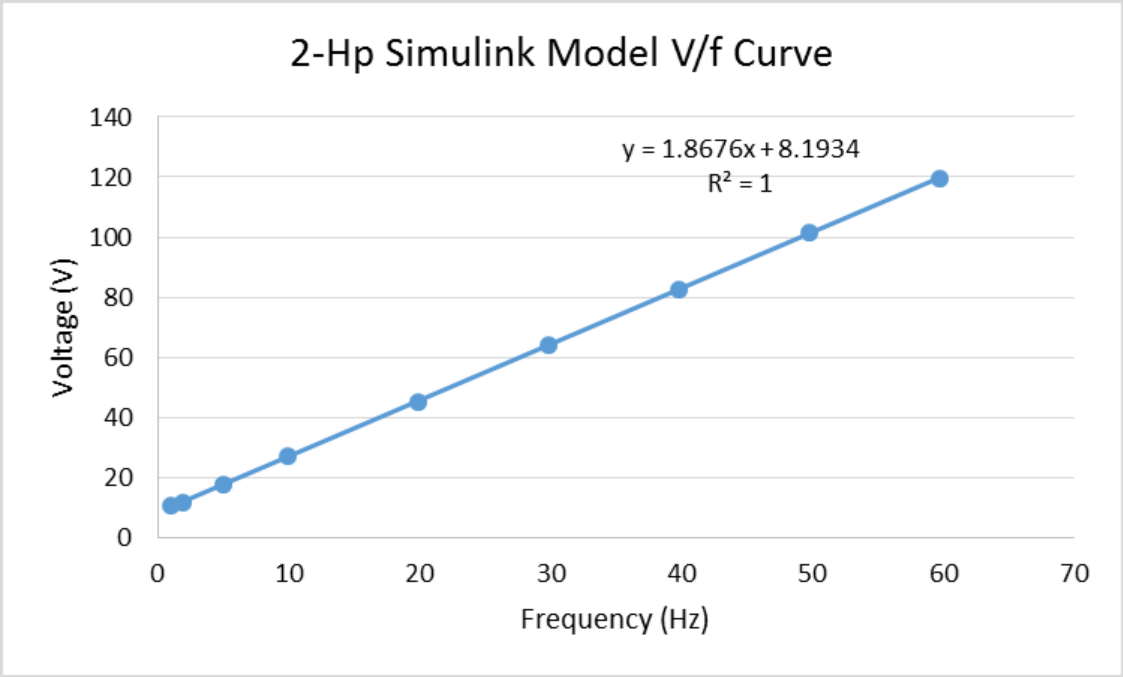

Figure 3.22: V/f curve obtained through simulation in Simulink for 2-hp induction motor running under no-load condition.

From the control system modeled in Simulink, the V/f curve, shown in Figure 3.22, illustrates an almost ideal linear relationship between the applied voltage and frequency. Indeed, one can observe a constant V/f ratio with the machine operating between 5 and 60 Hz where the ratio is relatively constant. However, at the lower frequencies of 1 and 2 Hz, the limitations of the open-loop scalar controller are shown. Indeed, the calculated V/f ratio varies considerably from the calculated theoretical quantity. Consequently, at these lower operating points, the ratio between the voltage and frequency is not maintained. Hence, the flux is not constant in this region. A compensation system should be implemented to enhance the operation of the induction motor at a lower frequency. However, considering that the case study is referring to the tunnel ventilation system, the fans are running at least at 50 % operating speed. The linear regression of the curve is

achieved in Excel and the V/f ratio can be calculated using the slope of the trend-line. By dividing the ratio by 2π, one can get the constant in relation to the angular frequency. As such, the average V/f ratio obtained from the simulation analysis is evaluated to be 0.297.

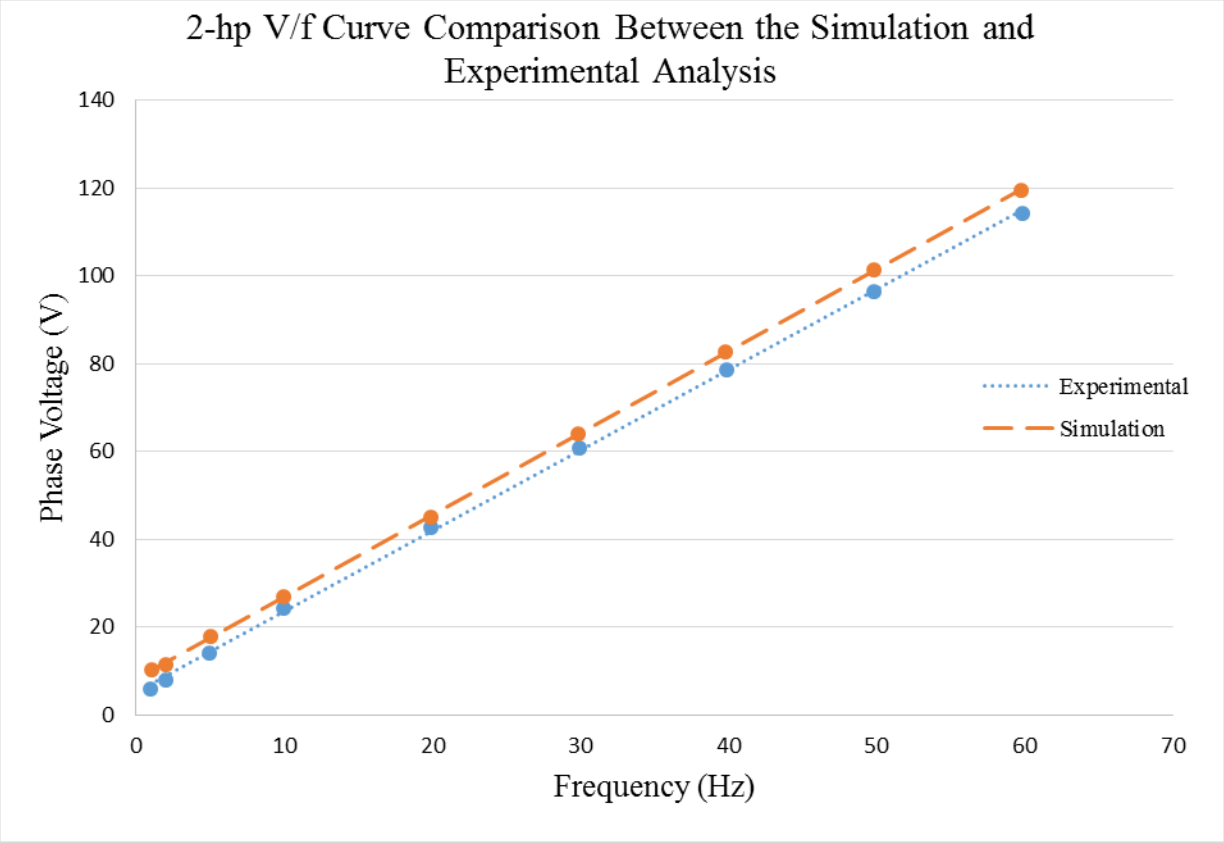

Figure 3.23: V/f curve comparison between the simulation and experimental results for the 2-hp induction motor running under no-load condition.

In Figure 3.23, the simulated and experimental V/f curves are plotted on the same chart. As can be seen, the experimental curve is slightly offset compared to the simulated one. Such observation can be justified by the effect of the non-idealities found in the experimental system. Indeed, in the simulation, many components are considered ideal, which is not the actual case in a real-life system.

As can be observed, the scalar V/f control is validated experimentally based on the constant relationship obtained between the physical induction motor applied phase voltage and its corresponding operating frequency. Again, as demonstrated in the simulation process, the V/f ratio

tends to be constant at higher operating frequencies close to the rated frequency. Experimentally, the ratio is relatively constant for frequencies over 20 Hz as opposed to 5 Hz for the simulation. Based on the linear regression trend computed in Excel, the experimental V/f ratio is evaluated to be 0.293. Additionally, when considering low frequencies in the trend computation (i.e. 1, 2 and 5 Hz), the experimental boost voltage is evaluated as 5.068 V which differs slightly than the theoretical value of 8.28 V. However, when ignoring the lower frequency points and considering only the operating region where the control is optimized, the boost voltage is estimated as 7.11 V.

Overall, the scalar control has been validated both in simulation and experimentally within acceptable results. Indeed, when evaluating the relative error in regards to the theoretical V/f ratio, a 0.338% error is obtained in the simulation analysis whereas an error of 1.02% is obtained experimentally. As such, when considering industrial applications such as ventilation fans, the results provided by the designed open-loop scalar control are proven to be adequate.

3.6.2 Open-loop Control Response to Speed Command Change

With the implemented open-loop speed control system developed to emulate the tunnel ventilation fan system, the main objective is to observe how the control would behave to speed command change as it would happen within the tunnel based on the level of traffic density and quality of air. The operating profile of the fans is as such that they are either stationary or running at a percentage higher than a specified threshold, 50% for the Louis-Hippolyte Lafontaine tunnel test case. Indeed, they are never operating below 50% as this region is not energy efficient for the induction motors and drive system.

To validate the speed command change response of the developed control system, a varying speed reference has been applied to the system. The transition between different reference speed values is achieved gradually following a ramp pattern. To follow the tunnel control in regards to the ventilation system, the speed references operating percentages are of the order of 50, 66 and 100% of the rated speed. As such, the drive is given a speed reference sequence spread in a 36s interval that is summarized in Table 3.7.

Table 3.7: Speed reference sequence applied to the control system.

Time (s)	Speed (RPM)
0	0
4	900
8	900
12	1200
16	1200
20	1800
24	1800
28	900
32	900
36	0

The speed reference sequence tabulated in Table 3.7 is used for both the simulated model illustrated in Figure 3.9 and the experimental setup of Figure 3.10. The Simulink model has been simulated with a sampling time T_s of 5 µs for a total simulation time span of 40s. The measured induction motor speed with respect to the speed reference sequence used for the controller input are both shown in Figure 3.24 (a) and zoomed-in (b) and (c).

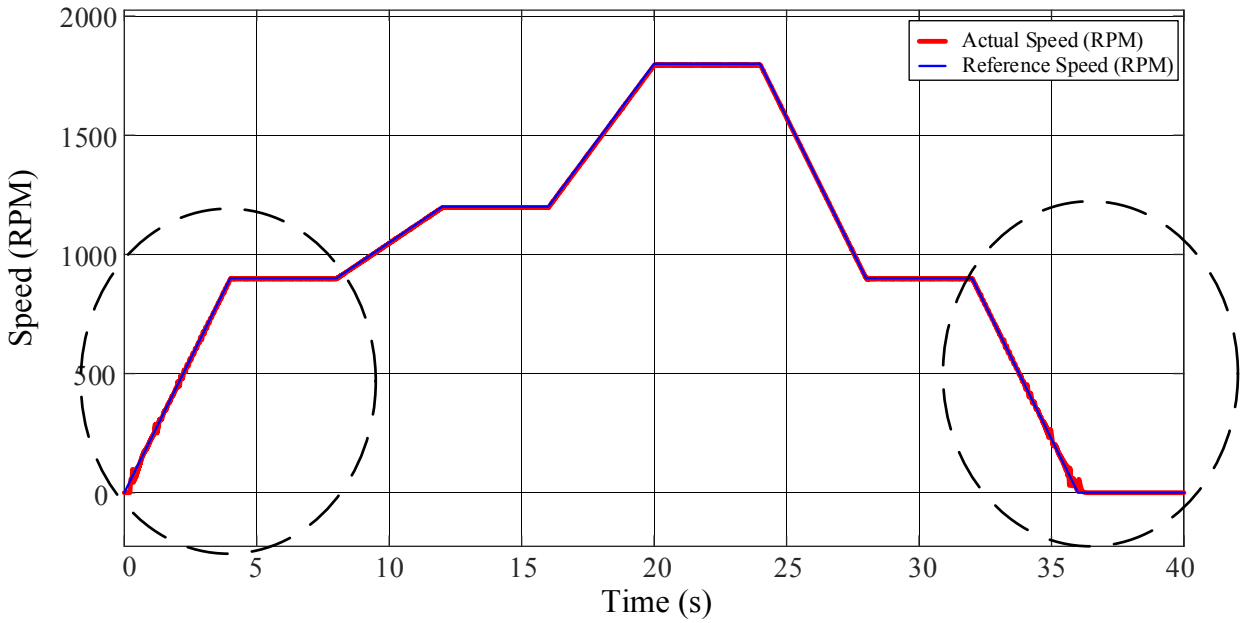

(a)

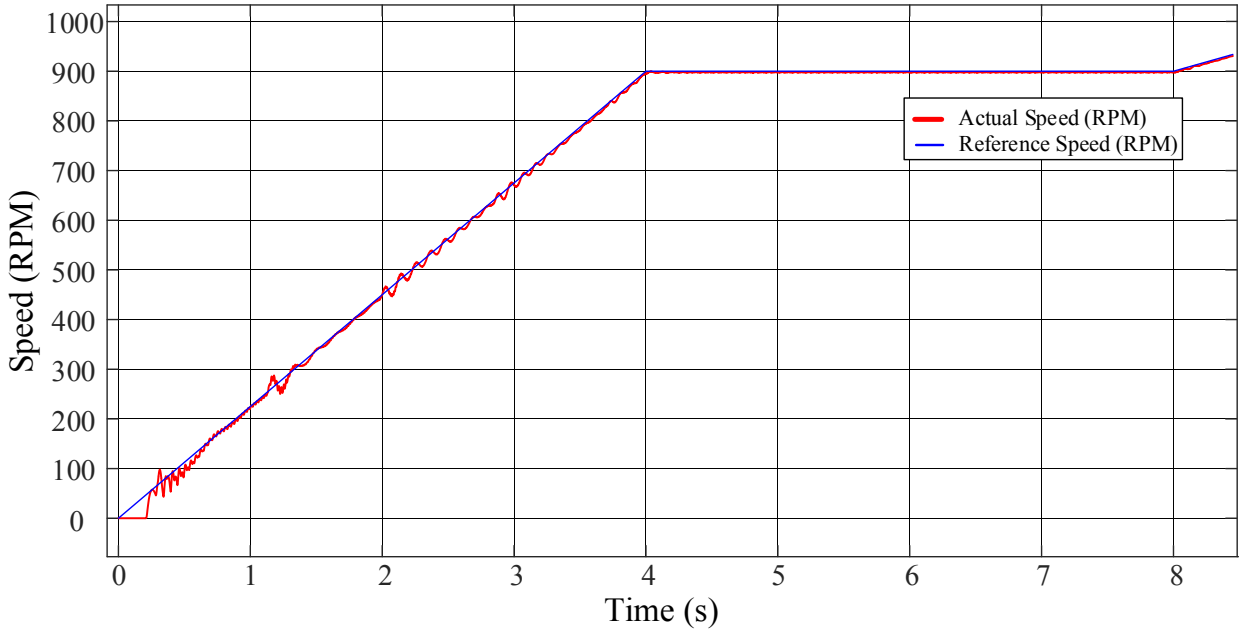

(b)

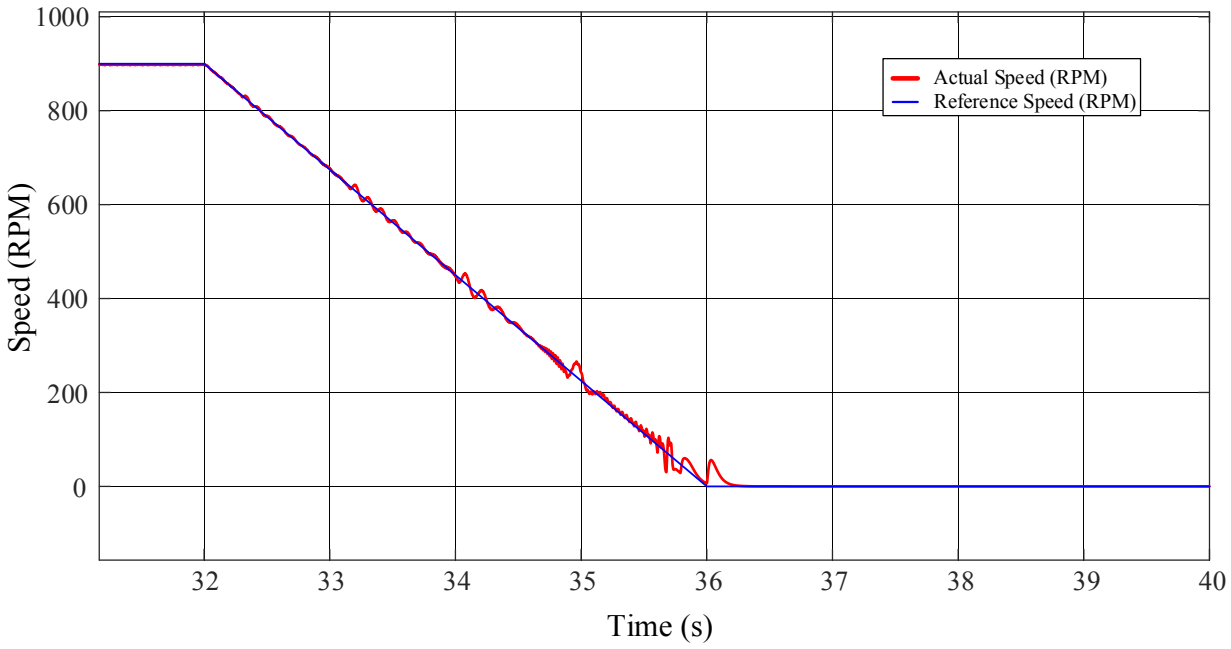

(c)

Figure 3.24: Simulation results for the: (a) complete speed reference sequence, (b) zoomed-in region of induction motor acceleration from 0 to 900 RPM, and (c) zoomed-in region of induction motor deceleration from 900 to 0 RPM.

As can be observed from Figure 3.24, the speed controller responds accordingly to the speed reference sequence when considering the type of applications the controller would be used for.

Considering the fact that the control system is open-loop and there is no speed feedback, the measured speed of the induction motor follows closely the speed reference. From Figure 3.18 (b), the zoomed-in region illustrating the transition from 0 speed to 900 RPM shows more oscillation in the actual measured speed before it settled at 900 RPM. Within this test procedure, the limitations of the control system are also shown for low operating speed where the assumptions made are no longer valid. This is due to the non-idealities of the system components at low frequency. Indeed, from the simulation, the speed response can be improved by considering the nonlinearities of the different system components.

The speed reference sequence is also used for the experimental setup. In order to measure the actual motor speed, the DC voltage generated at the speed sensor terminals has been recorded and converted to RPM using its dedicated gain, which has been adjusted with the speed measurements from the validation of the V/f control system test procedure. Hence, instead of having a gain of 50Vdc/1000 RPM, it is adjusted to 50.6 Vdc/1000 RPM based on the measured speed using the portable laser tachometer. Additionally, using the digital-to-analog converter of the dSPACE module, the speed reference sequence is plotted on the oscilloscope against the measured speed. While the test is undergoing, a lot of noise has been noticed in the measured voltage signal as illustrated in Figure 3.25.

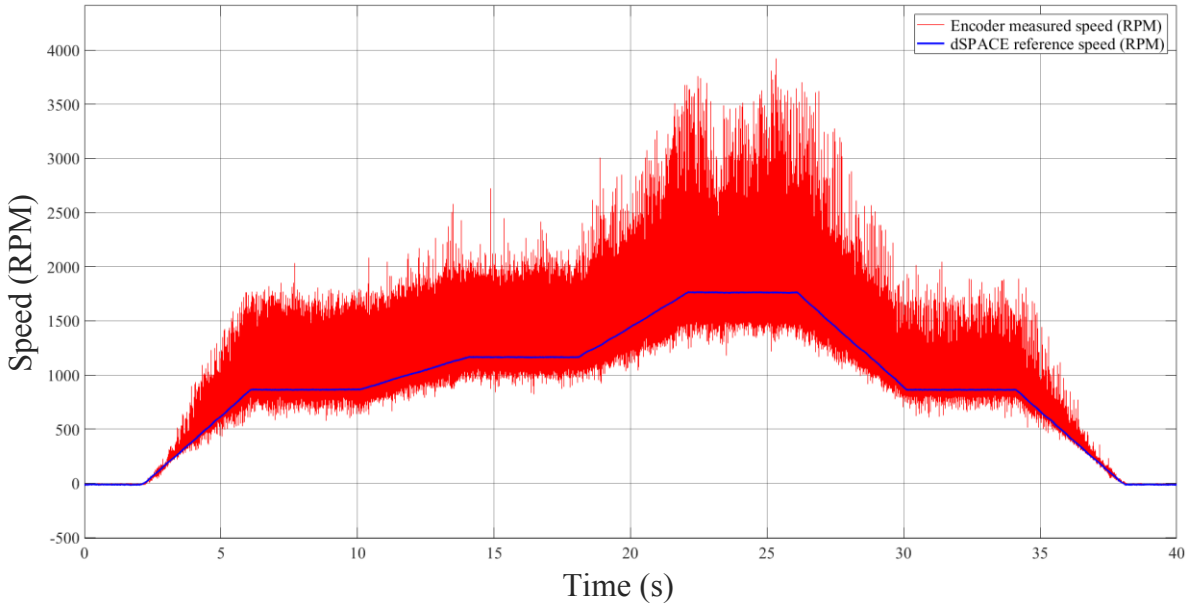

Figure 3.25: Measured speed response superimposed on the speed reference profile captured in dSPACE without filtration.

To limit the noise effect on the recorded signal, the measured voltage has been extracted from the oscilloscope to the MATLAB environment to filter out the noise and have a better representation of the controller speed response. The type of filter providing the best signal is found to be the Bessel low pass filter of order 25 with a cutoff frequency of 600 Hz. Then, the speed reference sequence measured from dSPACE and the measured speed from the speed sensor are plotted together and adjusted with their corresponding gains. The resulting responses are shown in Figure 3.26.

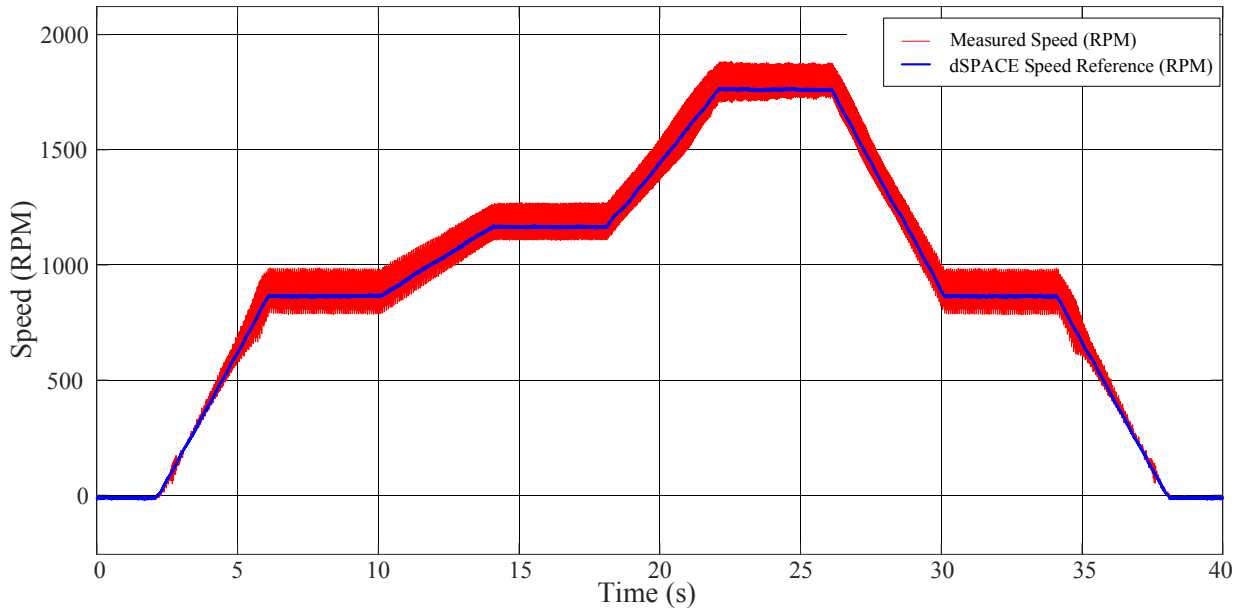

Figure 3.26: Measured speed response superimposed on the speed reference profile captured in dSPACE with filtration.

In regards to the filtered signal shown in Figure 3.26, it can be observed that measured speed at the sensor's terminal tends to follow the speed reference sequence computed by the dSPACE model. Indeed, if a more accurate speed sensor had been used or if the average value of the speed signal is taken, the measured speed value would be close to the reference. Furthermore, the operating points shown in Figure 3.26 are illustrating a possible operational profile of an industrial ventilation system. As such, the developed open-loop scalar V/f control has the capability to go from standstill zero speed to the desired operating speed progressively. It has the capability to follow a predetermined slope and maintain this speed for the required time and vice-versa from a given speed to the stationary state of the induction motor with satisfactory accuracy for these

applications. In order to get more accurate results or for the design of a closed-loop system, the speed sensor would need to be tuned in order to avoid or limit the amount of noise found in the signal.

3.7 Summary

In this chapter, an induction motor drive system used for industrial applications, such as for ventilation fan systems, was developed using an AC-DC-AC converter, while the two-level inverter was using the IGBT as the semiconductor devices. A similar system was modeled and built in MATLAB/Simulink. With the industrial ventilation fans ratings being in the 100-hp range, the developed drive system was designed for a lower power rating of a 2-hp Wye-connected induction motor. Furthermore, considering the type of application that is the Louis-Hippolyte Lafontaine tunnel, an open-loop scalar V/f control was found to be the most suitable control scheme as it did not require high-speed control precision provided by a closed-loop system as it would be needed for electrical vehicles drive system. The modulation approach taken was the SPWM to which was incorporated the third harmonic injection strategy, thus increasing the linear region by close to 15%. The theoretical V/f ratio was determined using the machine parameters and was modeled in Simulink for simulation validation. The inverter output phase voltage was extracted using the FFT tool to evaluate the fundamental voltage component for frequencies of 1, 2, 5, 10, 20, 30, 40, 50 and 60 Hz and the V/f curve was plotted accordingly. Furthermore, a reference speed sequence was imposed on the control system input to analyze the dynamic performance of the system when it was subjected to speed command change as it would be seen in ventilation fan control system. The same process was implemented experimentally where the control system was achieved in the dSPACE environment with the actual 2-hp induction motor. The control was validated both in simulation and experimentally with their respective V/f ratio being within an acceptable relative error range when compared to the theoretical value. Finally, the controller response to speed command change sequence was also validated in simulation and experimentally with the measured speed following closely the speed reference.

Chapter 4: Scaled-Down Simulation of the Louis-Hippolyte Lafontaine Tunnel's Electrical Profile

4.1 Introduction

The complete electrical profile of the Louis-Hippolyte Lafontaine tunnel has been first described in Chapter 2 of this research work. It has been shown that the tunnel electrical energy consumption is greatly influenced by the weather conditions and the period of the day. Indeed, peak power demand is observed in the yearly load profile of the tunnel during the winter season due to the heating requirements. Hence, the power demand increases with colder temperatures in order to avoid freezing of the tunnel systems. Additionally, the daily load profile shown in Chapter 2 indicated that the power demand is greatly impacted by the outside luminosity. Consequently, the level of lighting inside the tunnel increases with the intensity of the sun and thus, the tunnel power demand is at its maximum during the day. The outcome of Chapter 2 illustrated that the main group of electrical loads is composed of the heating, lighting and ventilation loads.

As such, in order to implement a representative model of the tunnel's electrical profile, the simulated system is comprised of the three main electrical loads (heating, lighting, and ventilation), electrical grid for the main supply and diesel generator acting as the auxiliary power supply. In this chapter, the simulated system representing the tunnel simplified scaled-down electrical profile is modeled in Simulink and analyzed. For the purpose of this research work, the heating and lighting electrical loads are defined as static load due to the fixed nature of their components [48, 49]. As for the ventilation system, it is defined as a dynamic load due to the presence of electromechanical transients in the induction motor load variations [50]. Moreover, the drive model used for the emulated ventilation fan system has been implemented and validated in simulation and experimentally in Chapter 3. The diesel generator model developed in [51] is used in this work for the emergency power supply system.

The simulated system of the simplified tunnel electrical profile is analyzed under different loading scenarios. Indeed, as indicated above, the power demand is highly related to the weather conditions. As such, the electrical profile of the tunnel is simulated for three operational scenarios: during a summer day, a winter day and an emergency situation. Additionally, the model is configured in a way that the loading percentage for the different electrical loads is subjected to

change in order to have a better representation of the case under study for the electrical load profile. Briefly, the winter scenario will see the electrical profile largely dominated by the heating loads and followed by the lighting loads. Next, the summer months will be defined by a load profile of combined lighting and ventilation electrical loads. As for the emergency test case, a diesel generator will act as the main supply for the essential electrical loads in the event where the tunnel is disconnected from the electrical grid. The electrical profile of each scenario is then analyzed. The area of interest for the analysis of each scenario system configuration is defined as the point of common coupling (PCC) between the grid supply, or diesel generator, and the electrical loads.

The modeling process for the tunnel electrical profile is based only on the main electrical loads impact during a given operational scenario. Indeed, the loading percentage for the heating, lighting and ventilation loads varies according to the external weather conditions and thus, the time of the year. Furthermore, each of the considered electrical load is modeled based on the power characteristics obtained from the tunnel on-site measurements discussed in Chapter 2. The load modeling is achieved using measurement-based data [48]. As such, the heating loads are represented as ideal resistive loads [52]. The measurements have shown that the heating system only consumed real power (W) with a unity power factor.

Then, the high pressure sodium (HPS) lighting system configuration is comprised of a ballast interfacing the lamp with the main supply. Within this ballast, reactive power compensation is achieved as a means to improve the power factor (PF) of the HPS lighting fixture [53, 54, 55]. With the ballast operating at high switching frequency, the HPS lamp can be represented as a pure resistance [56]. Consequently, considering the power characteristics observed from the measurements of the tunnel lighting system as mentioned in Chapter 2, the HPS lighting fixtures are represented as a RL load. The inductance is added to the resistance of the lamp in order to meet the same PF measured for the lighting system in Chapter 2.

Finally, the remaining main electrical load is the ventilation system. As discussed in Chapter 3, this system is comprised of multiple units, each with a VFD driving an induction motor and fan blades coupled to it [26]. The control system used for the VFD is the open-loop scalar control due to the simplicity and the nature of the application of a ventilation fan system. The model has been validated in simulation and experimentally under no-load conditions. However, for the purpose of the tunnel electrical profile simulation, the ventilation modeled system presented in Chapter 3 is

to be loaded. In reference to the 2-hp induction motor parameters used in the model [40], the machine has a rated full-load torque of 8.16 N-m. Consequently, based on the operational profile of the system, the ventilation fans are to be operated at 50, 66 and 100 % of the rated speed in addition to the machine being loaded.

Moreover, the presence of non-linear loads and highly inductive loads in an industrial electrical system often results in power quality problems that can result in damaging the infrastructure electrical equipment. The tunnel electrical infrastructure is no different in that matter. Indeed, it is equipped with multiple VFDs used for the control of fans and pumps. The use of these power electronic devices allows for a more efficient control that results in power and economical savings [57]. However, their integration to the system results in the introduction of non-linear loads and hence, distortion in the voltage and current waveforms. High level of harmonics represents a risk and could be harmful to other equipment found inside the tunnel.

In order to achieve a power quality assessment of the tunnel electrical system comprised only of the main electrical loads mentioned previously, the voltage and current waveforms of each load at the PCC will be computed and analyzed. The proposed models for each scenario are implemented in the MATLAB/Simulink environment.

Furthermore, the electrical system considered for this emulation is illustrated by the single-line diagram (SLD) shown in Figure 4.1. Each of the developed operational profile is determined by the status of the selector switch indicated by SW*x* on the SLD where *x* is indicating the switch number. It is to be noted that the rating of the electrical loads varies between each scenario in order to properly reflect the impact of each load for a given scenario.

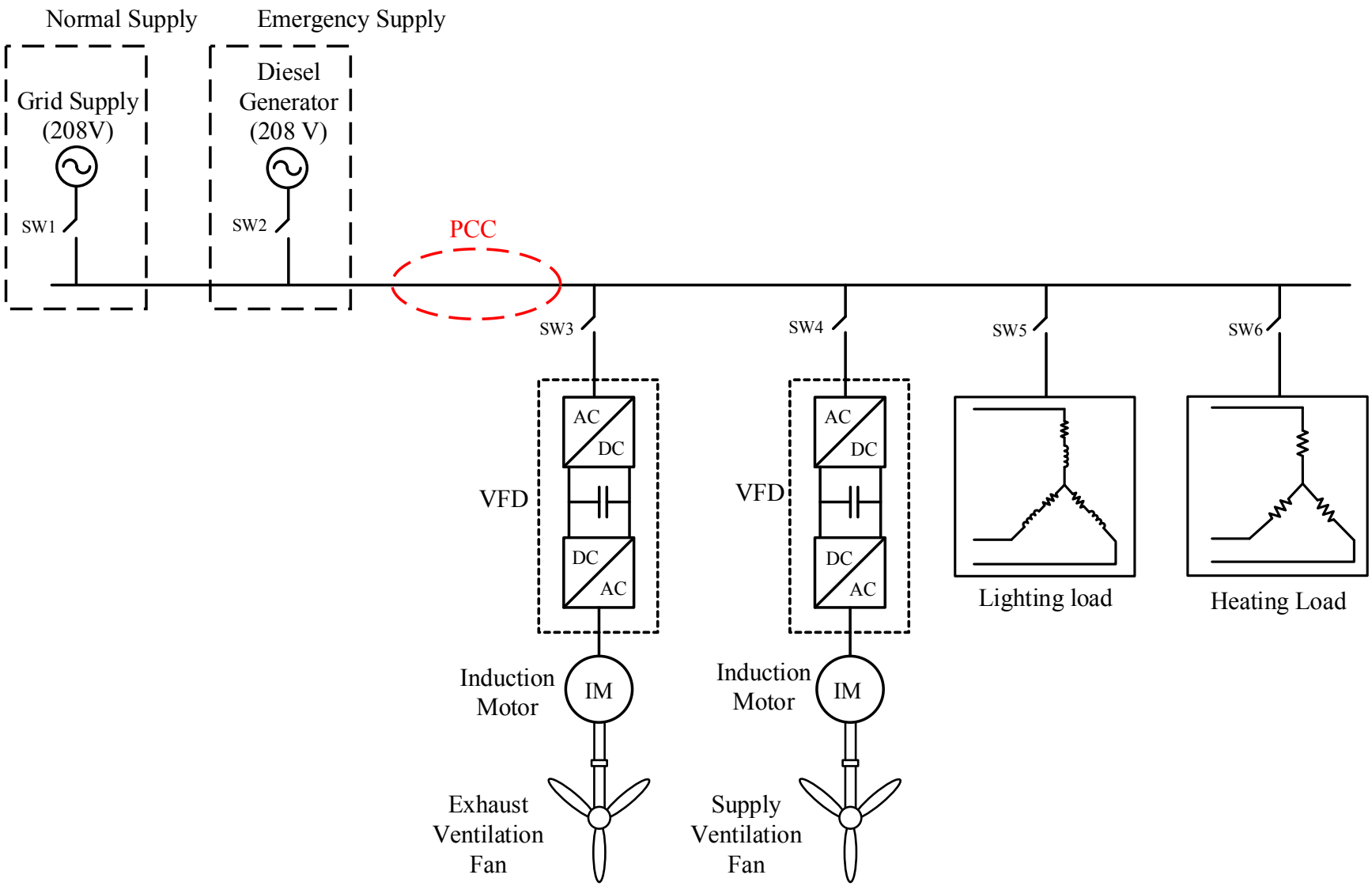

Figure 4.1: Tunnel electrical system configuration to be simulated.

4.2 Loading of an Induction Motor

In Chapter 3, the tunnel ventilation system has been simplified and defined as an induction motor, acting as the prime mover for the fan blades, for which the speed is controlled through the use of a VFD. The control model has then been validated in simulation and tested experimentally under no load condition. However, in the representation of the ventilation system, the induction motor is loaded as torque is required to initiate and maintain the rotational speed of the fan blades. Consequently, for the simulation of the tunnel electrical profile, a load torque is applied to the induction motor in the model previously implemented in Simulink.

The induction motor induced torque is calculated using the air-gap power and the synchronous angular speed as illustrated by:

$$\tau_{ind} = \frac{P_{ag}}{\omega_s} \tag{4.1}$$

where τ_{ind} is the induced torque, P_{ag} is the air gap power and ω_s is the synchronous angular speed.

The air-gap power is defined as the power transferred across the air gap between the stator and rotor circuit. Moreover, this power quantity corresponds to the power absorbed by the resistance R_r'/s shown in Figure 3.3 of Chapter 3. As such, Equation 4.1 can be re-written as follows:

$$\tau_{ind} = \frac{3I_r'^2(R_r'/s)}{\omega_s}. \tag{4.2}$$

In order to determine the rotor current I_r', Thevenin's theorem is applied to the equivalent circuit shown in Figure 3.3 of Chapter 3 [39, 40]. The magnitude of the Thevenin equivalent voltage is then calculated as follows:

$$V_{th} = V_s \frac{X_m}{\sqrt{R_s^2 + (X_s + X_m)^2}}. \tag{4.3}$$

Equation 4.3 can then be simplified further when considering that $X_m >> R_s$.

$$V_{th} \approx V_s \frac{X_m}{X_s + X_m}. \tag{4.4}$$

The Thevenin equivalent stator impendence is then calculated as the parallel impedance between the stator impedance (R_s and X_s) and the magnetizing reactance (X_m). The Thevenin impedance is comprised of a real and imaginary part as indicated by:

$$R_{th} \approx R_s \left(\frac{X_m}{X_s + X_m}\right)^2 \tag{4.5}$$

$$X_{th} \approx X_s \,. \tag{4.6}$$

Equation 4.5 and 4.6 are simplified and approximated due to $X_m >> R_s$ and $X_m + X_s >> R_s$. Then the magnitude of the rotor current can be calculated using the Thevenin equivalent voltage and impedance as:

$$I_r' = \frac{V_{th}}{\sqrt{\left(R_{th} + \frac{R_r'}{s}\right)^2 + (X_{th} + X_r')^2}} \,. \tag{4.7}$$

Then, the rotor current magnitude of Equation 4.7 is substituted into Equation 4.2 for the calculation of the induced electromechanical torque defined as:

$$\tau_{mech} = \frac{1}{\omega_s} \frac{3V_{th}^2 \frac{R_r'}{s}}{\left(R_{th} + \frac{R_r'}{s}\right)^2 + (X_{th} + X_r')^2} \,. \tag{4.8}$$

Furthermore, the maximum pullout torque can be determined based on the maximum air-gap power of the induction motor. Henceforth, in order to obtain this operational condition, the referred rotor resistance R_r'/s should be equal to the magnitude of the source impedance defined as [43]:

$$R_r'/_s = Z_{source} = \sqrt{R_{th}^2 + \left(X_{th} + X_r'\right)^2} \,. \tag{4.9}$$

Then, the slip at which the air-gap power is maximum can be extracted from Equation 4.9 and used to determine the value of the induction motor pullout torque as follows:

$$s_{max} = \frac{R_r'}{\sqrt{R_{th}^2 + (X_{th} + X_r')^2}} \tag{4.10}$$

$$\tau_{max} = \frac{1}{2\omega_s} \frac{3V_{th}^2}{(R_{th} + \sqrt{R_{th}^2 + (X_{th} + X_r')^2})} \,. \tag{4.11}$$

As illustrated by Equation 4.11, the maximum torque is directly proportional to the square value of the Thevenin equivalent voltage and is independent of the rotor resistance. Furthermore, as illustrated by Figure 3.5 from Chapter 3, for a constant V/f control, the induction motor is said to be operating in the constant torque region when the machine is running below rated frequency. Indeed, for any given speed in this region, the induction motor is able to deliver its rated torque. Consequently, the torque locus for frequencies below the rated value is characterized by the same maximum torque quantity only shifted based on the corresponding rotor speed. The torque locus of the 2-hp induction motor presented in Chapter 3 is shown in Figure 4.2 for frequencies between 10 and 60 Hz.

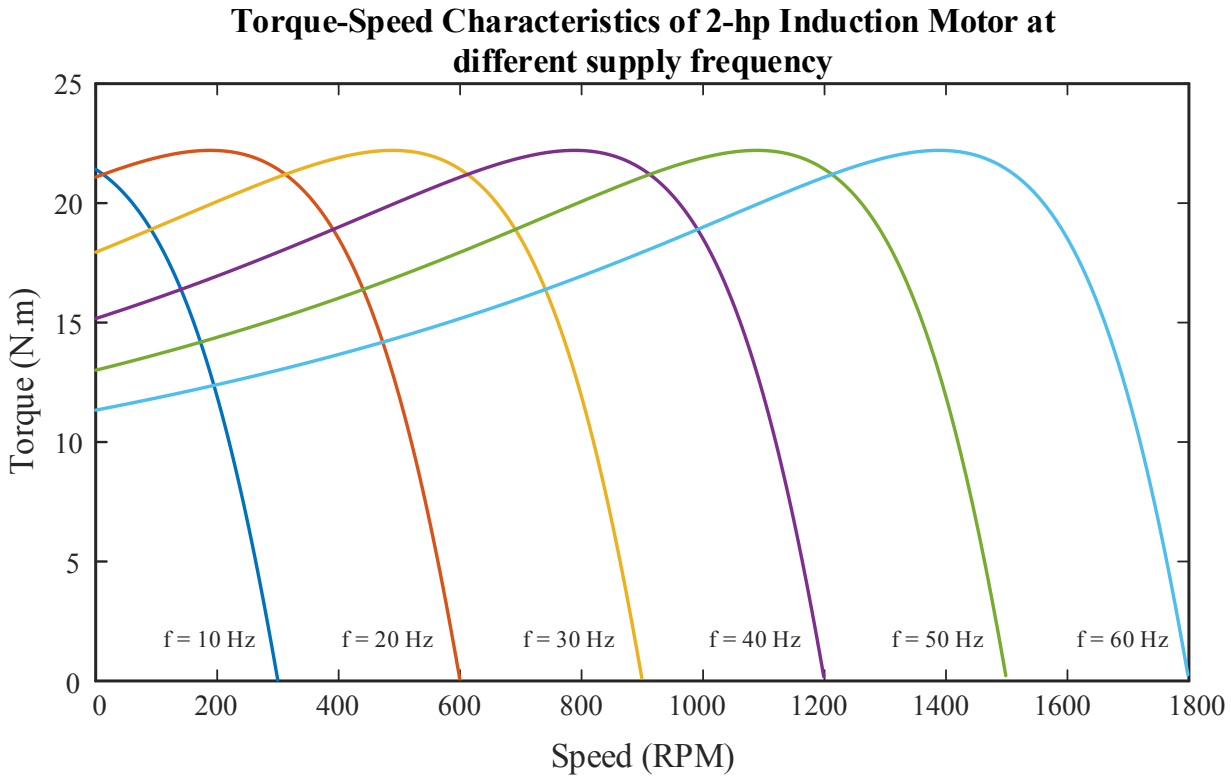

Figure 4.2: Torque locus generated from the 2-hp induction motor equivalent circuit for frequencies between 10 and 60 Hz.

As illustrated by Figure 4.2, for the lower frequency operation, the maximum torque is slightly less due to the effect of the stator resistance voltage drop, thus the requirement for boost voltage compensation in the control of the drive. Moreover, when the induction motor is running above

rated frequency in the field weakening region, the applied voltage across the stator remains constant at the rated value and the operating frequency becomes larger than the rated frequency. From the datasheet of the Baldor M1556T 2-hp induction motor [40], the maximum pullout torque is shown as 20.94 Nm whereas the one computed for the induction motor equivalent circuit is estimated as 22.1 Nm. Moreover, while the voltage value remains constant, the ratio between the operating and rated frequencies becomes greater than 1 resulting in a decreasing effect in the machine maximum pullout torque. However, for the purpose of this work, only the constant torque region is considered as the performance of the induction motor is analyzed for constant flux operation. The control of the induction motor drive is implemented for operation between 0 and 60 Hz as it would be observed for the tunnel ventilation fan systems.

4.3 Tunnel Operational Profile for the Summer

The first operational profile to be considered is for a reference summer day in terms of the typically solicited electrical loads. Consequently, due to the warmer weather in summer, there are no requirements for heating elements. Indeed, the main electrical loads present during the considered season are the lighting and ventilation loads. In regards to the lighting load, the corresponding power demand is higher during this period of time due to the daylight being longer in time in addition to the lighting levels being also higher than what would be observed during a winter day. Moreover, the ventilation fans are mainly operating during the summer due to the warmer temperature, leading to a reduced level of air quality. Consequently, the ventilation fans are operating to extract the polluted air and supply clean air inside the tunnel. Hence, the selector switches SW1, SW3, SW4, and SW5 shown in Figure 4.1 are closed, while the rest remains open for this scenario. The simulated operational profile system configuration SLD is shown in Figure 4.3.

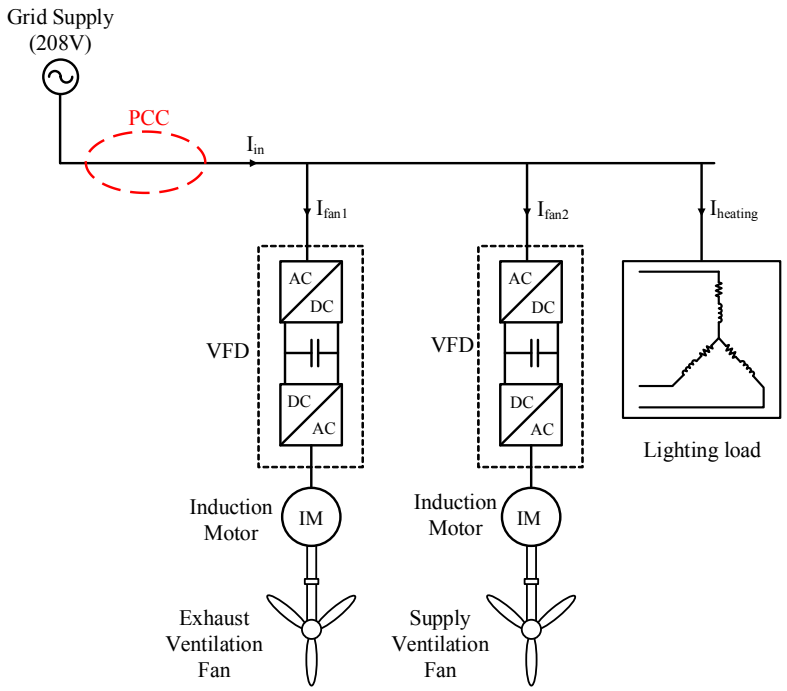

Figure 4.3: SLD of the simulated tunnel system configuration for a summer day.

Here, the ratings of exhaust and supply ventilation fans are assumed to be equal. Furthermore, the peak power demand from the lighting is also greater than the peak power demand observed from the ventilation. Consequently, the ratings of each element shown in the emulated system of Figure 4.3 are summarized below in Table 4.1.

Table 4.1: System element ratings for the tunnel operational profile during a summer day.

System Elements	Ratings
Grid Supply	208 V, 60 Hz
Exhaust Ventilation Fan	208 V, 6.1 A, 2-hp, 60 Hz
Supply Ventilation Fan	208 V, 6.1 A, 2-hp, 60 Hz
Lighting Load	208V, 4000 VA, PF = 0.95, 60 Hz

4.3.1 Power Characteristics Assessment of Summer Scenario

In the summer scenario described above, the simplified electrical system is comprised of the electrical grid supplying the considered loads shown in Figure 4.3. Indeed, in regards to the tunnel operational profile during the summer, the ventilation fans in addition to the lighting system are said to be in operation under this scenario. With their respective power characteristics discussed

in the introduction of this chapter, the current and voltage waveforms are measured at the PCC and for each load independently to visualize their respective contribution to the overall power quality.

Considering the nature of the electrical loads incorporated into this emulated scenario, the input current measured at the PCC is expected to be highly distorted due to the presence of the two VFDs used for the control of the ventilation fans. Indeed, the diode bridge rectifier component is conducting only during the period where the input instantaneous line voltage is greater than the average DC-link voltage [58]. Hence, the input current to the VFD is not sinusoidal, but is shaped as pulses. Consequently, the PF and the THD of this particular load are significantly impacted by the ventilation load.

A corresponding model to the system configuration shown in Figure 4.3 is implemented in Simulink for the simulation of the tunnel operational profile during a summer day. The ratings used for the electrical loads of this scenario are indicated in Table 4.1. In this scenario, their operating speed and loading percentage are identical. Indeed, the given reference speed is the synchronous speed of 1800 RPM and the loading torque is 6 N-m. The supply voltage is assumed to be maintained constant and the electrical loads balanced. The phase voltage and the line current for the lighting load are plotted together and illustrated in Figure 4.4.

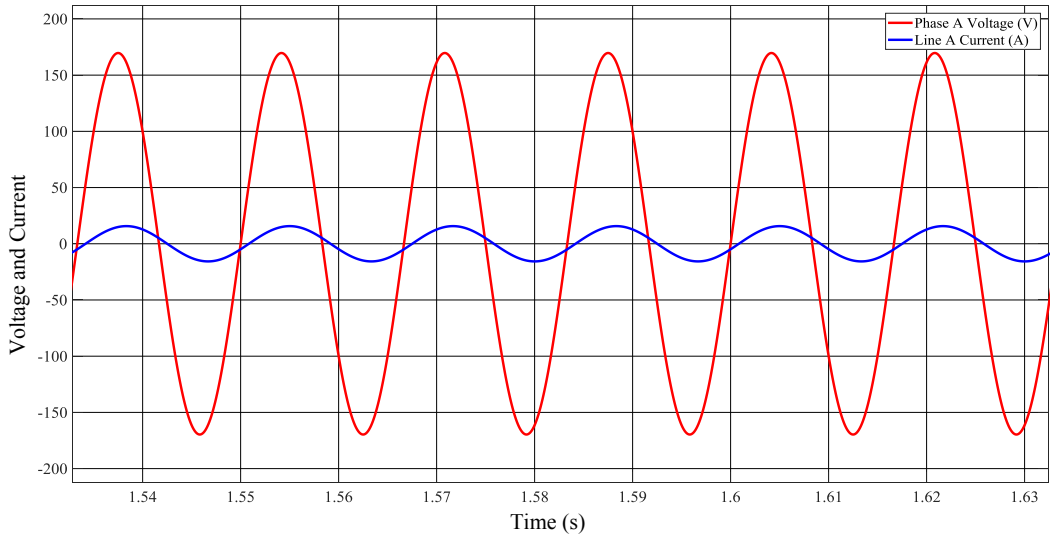

Figure 4.4: Phase voltage superimposed with the line current for the lighting electrical load during a summer day.

From Figure 4.4, the line current is slightly lagging the phase voltage as expected from the designed load. Indeed, when looking at the fundamental component, the current is lagging the voltage by 18.5°, corresponding to a PF of 0.95. The level of harmonic is relatively low for this load as illustrated by the sinusoidal current waveform. Indeed, the on-site measurements presented in Chapter 2 have led to the same observation. With the supply voltage assumed constant and the load to be balanced, the operation of the lighting system is considered ideal. Indeed, flickering in the HPS lights could be observed in the event of voltage sag [59].

Moreover, the line currents for a single fan are computed and shown in Figure 4.5 for the summer electrical profile emulation. The same waveform is observed for the second fan as well.

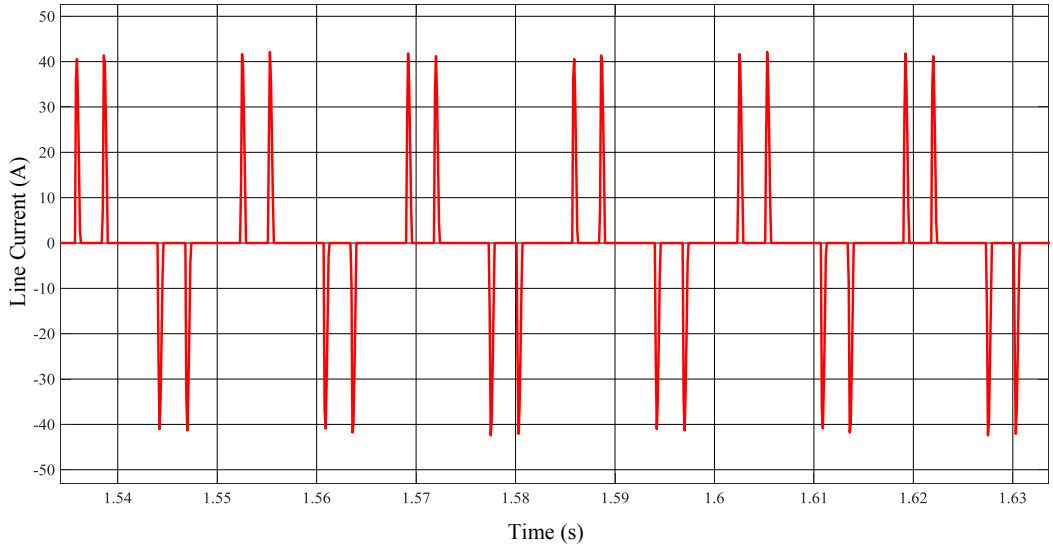

Figure 4.5: Line current I_{fan1_a} for a single ventilation fan electrical load during a summer day.

As can be seen from Figure 4.5, the input current of the VFD is highly non-linear due to the diodes of the rectifier conducting only under a certain threshold determined by the DC bus voltage. Thus, for ventilation fans, the level of current harmonics introduced into the tunnel electrical system is high at 242.51%. The repetitive sequence of two spikes in the line current waveform seems to indicate that the DC link capacitor is oversized for the 2-hp induction machine as the DC bus voltage is maintained. Indeed, one can notice similarities with the actual line currents measured at the input of the VFD during the site visit, which is illustrated below in Figure 4.6. However, in this real system, the load of the ventilation fan and the induction motor is more demanding on the VFD. Hence, the discharge of the capacitor is reflected on the actual input current.

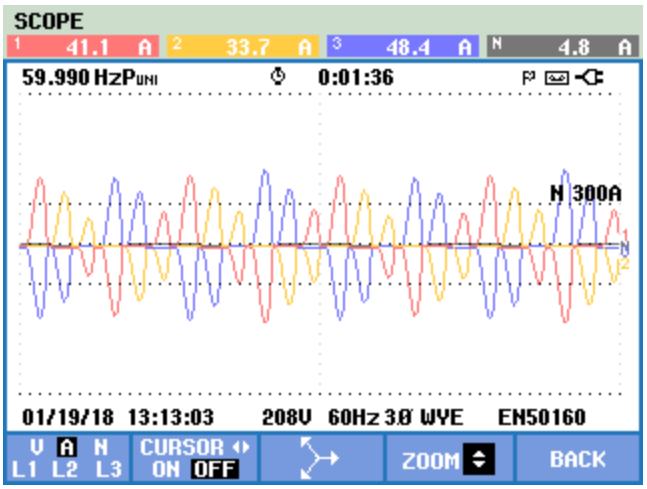

Figure 4.6: Line currents measured at the VFD input of the tunnel ventilation fan.

The apparent power consumed by the individual ventilation fan can be calculated using the RMS value of the line current and voltage measured at the input of the VFD. Then, the active power can also be estimated based on the power balance theory between the input AC signal of the rectifier and its output DC signal. As such, the consumed active power is calculated using the DC bus voltage and current. The system is assumed lossless as ideal components are used in the modeling of the drive. The active and apparent powers are calculated using respectively Equation 4.12 and 4.13 as follows:

$$S_{fan} = \sqrt{3} V_{fan} I_{fan} \tag{4.12}$$

$$P_{fan} = V_{DC} I_{DC} \tag{4.13}$$

where, S_{fan} is the apparent power consumed by the ventilation fan (VA), V_{fan} is the RMS input line voltage of the VFD, I_{fan} is the RMS input line current of the VFD, P_{fan} is the active power consumed by the ventilation fan, V_{DC} is the average voltage across the DC bus and I_{DC} is the average current flowing through the DC bus. The PF is then computed as the ratio between the active power and the apparent power.

The power characteristics for one single ventilation fan are summarized in Table 4.2 based on the selected system parameters for this operational scenario.

Table 4.2: Power characteristics for a single ventilation fan for the summer operational scenario.

System Parameters	Ratings
Voltage (RMS)	208 V
Current (RMS)	3.86 A
Apparent Power (S)	3619 VA
Active Power (P)	1391 W
PF	0.384
THDi	242.51 %

The PF indicated in Table 4.2 is relatively low compared to what was observed from the tunnel measurements at the input of the actual VFD. Indeed, with the induction motor load being relatively low and the DC link capacitor being oversized for the given application, the active power transfer from the AC side to the DC side is limited. Hence, the ratio between the active and apparent power is relatively low. In the tunnel infrastructure, the industrial VFDs are sized accordingly to the motor and are often equipped with an active front end converter for power factor correction. The same thing can be said for the high level of harmonics. Since the power transfer is reduced, the RMS value of the fundamental component is reduced. Hence, the ratio between the harmonics and the fundamental component is relatively high. The THD percentage is reducing with a larger drawn current due to the fundamental component increasing whereas the level of harmonics is maintained constant.

Then, the load profile for a summer day is analyzed at the PCC to evaluate the combined impact of all the loads at the PCC. To assess the power quality for this scenario, the input line current of the system is measured when all the loads for this scenario are operating. The measured waveform is shown in Figure 4.7.

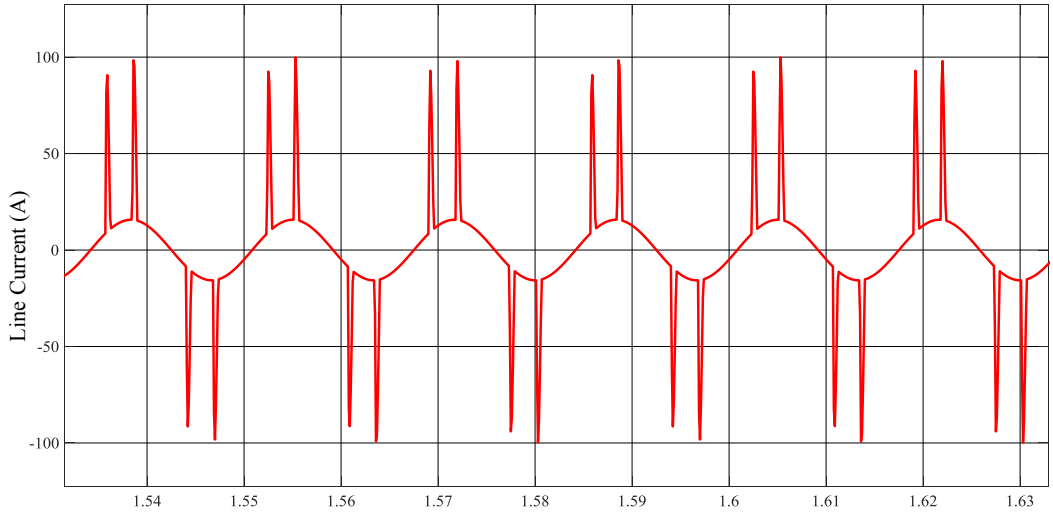

Figure 4.7: Input line current at the PCC for the summer operational scenario.

From the input line current waveform shown in Figure 4.7, one can observe the effect of each load individually at the PCC. Indeed, the sinusoidal component is the result of the lighting load whereas the spikes are caused by the ventilation loads. With the system assumed to be lossless, the active power consumed under this scenario is determined by the sum of the consumption of each load individually. The apparent power is determined by the product of the RMS values of the input line current and voltage.

Table 4.3: Power characteristics at the PCC for the summer operational scenario.

System Parameters	Ratings
Voltage (RMS)	208 V
Current (RMS)	18.58 A
Apparent Power (S)	9426 VA
Active Power (P)	6582 W
PF	0.70
THDi	101.34 %

As can be observed from Table 4.3, the summer scenario presents some power quality limitations in regards to the PF and the level of harmonics at the PCC. Indeed, a lower PF results in additional losses in the system whereas the high level of harmonics creates a potential hazard

for the tunnel equipment. Indeed, from the power characteristics mentioned in Table 4.3, the risk for power quality problems is greater during the summer due to ventilation fans being operated more frequently. The power electronic devices associated with the ventilation system result in a higher injection of current harmonics inside the system, which can result in damaging transformers or any other electrical devices.

Furthermore, the power demand during the summer operational scenario is at his lowest level on a yearly basis as mainly only the ventilation fans and the lighting system are operating on a frequent basis. In summary, the summer scenario is characterized by a lower power demand on the electrical grid with, however some concerns on the power quality level at the PCC.

4.4 Tunnel Operational Profile for the Winter

The second developed operational scenario involves the load profile of an arbitrary winter day representing the typical electrical loads that are solicited during this season. Compared to the profile presented for a summer day in Section 4.3, the demand from the ventilation system during the winter is practically null due to its operation being greatly influenced by the warm weather and the traffic intensity. Consequently, for the simulation of a winter day operational profile, the power demand from the ventilation system is assumed to be zero in the analysis. Furthermore, based on the report entitled "*Efficacité énergétique et déglaçage des entrées et sorties sans utilisation de sel du Tunnel Louis-Hippolyte-La Fontaine*" [14], the ventilation system operation percentage is increasing from almost zero during the month of May reaching a maximum energy consumption in August. Then, it decreases progressively back to almost zero in December. Then, due to the colder outside temperature, the heating load is now considered into the simulation of the tunnel electrical profile. Indeed, as illustrated by Figure 2.3 of Chapter 2, the overall power demand during the winter is corresponding to almost twice the demand for the summer months. Hence, with the lighting load being slightly less during winter, the considered resistive heating load is then of higher rating to illustrate the high contribution it plays in terms of energy consumption given this scenario. Hence, the selector switches SW5 and SW6 shown in Figure 4.1 are closed, while the rest remains open for this scenario. The simulated system for the tunnel operational profile for a winter day is illustrated in Figure 4.8.

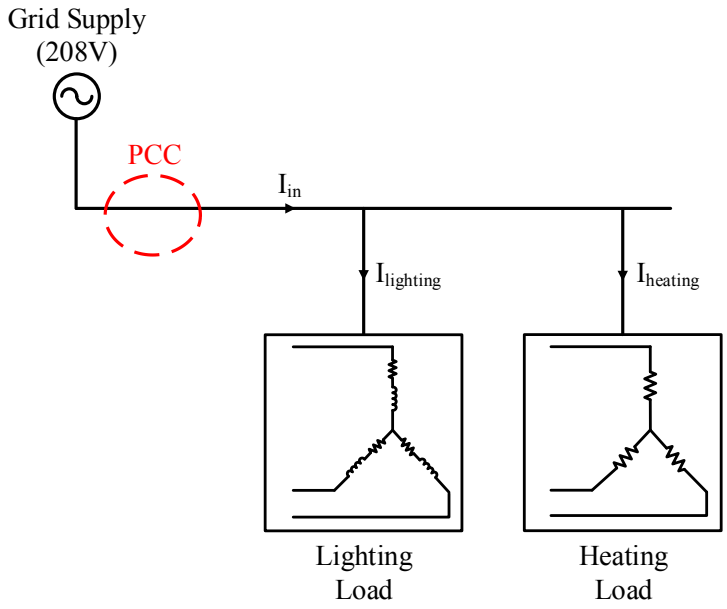

Figure 4.8: SLD of the simulated tunnel system configuration for a winter day.

Furthermore, as indicated above, the considered electrical loads for this operational profile are the heating and lighting loads. The ratings of the considered system elements are tabulated in Table 4.4.

Table 4.4: System element ratings for the tunnel operational profile during a winter day.

System Element	Ratings
Grid Supply	208 V, 60 Hz
Heating Load	208V, 10 000 W, 60 Hz
Lighting Load	208V, 4000 VA, PF = 0.95, 60 Hz

4.4.1 Power Characteristics Assessment of Winter Scenario

The tunnel winter scenario consists of the electrical grid which feeds the electrical loads typically in operation during this season. As mentioned above, the simulated winter electrical profile for the tunnel is mainly defined by the increase in power consumption due to the intensive heating requirements. For this scenario, the ventilation fan system is omitted as the fans are not running under these weather conditions. Consequently, for simulation purposes only the lighting and heating loads are considered. The extracted waveforms from Simulink are analyzed for the assessment of the power characteristics of this operational scenario. Again, the loads are assumed

to be balanced and the supply voltage is considered to be constant. The phase voltage superimposed with the line current for the lighting system are shown in Figure 4.9.

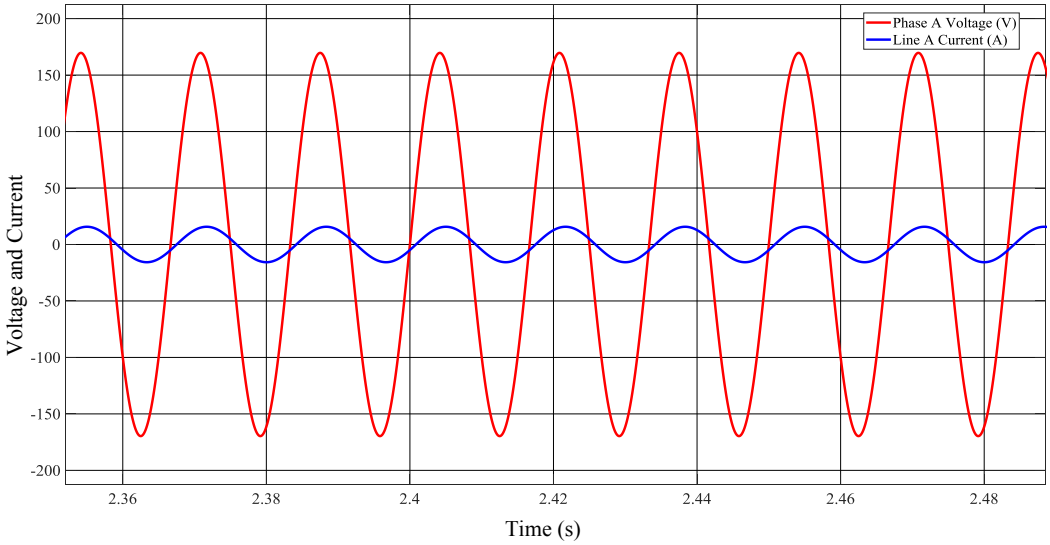

Figure 4.9: Phase voltage superimposed with the line current for the lighting electrical load during a winter day.

As illustrated by Figure 4.9, the lighting electrical load current is slightly lagging the voltage with a PF of 0.95. The same load is used for the summer and winter operational scenarios. Hence, the power characteristics noted for the lighting load in Section 4.3.1 are also applied here for the winter scenario. Indeed, the input current has a RMS value of 11.1 A and is characterized by a low THD of 0.31%. The consumed apparent power by the lighting load is evaluated as 3 998.95 VA.

Next, the heating electrical system is defined as a purely resistive load. Hence, the current and the voltage are in phase with unity PF. The power rating for the heating load is higher compared to the lighting load to illustrate the significant impact of the heating requirements during the winter. The heating load line current is computed with the respective phase voltage and is shown in Figure 3.10.

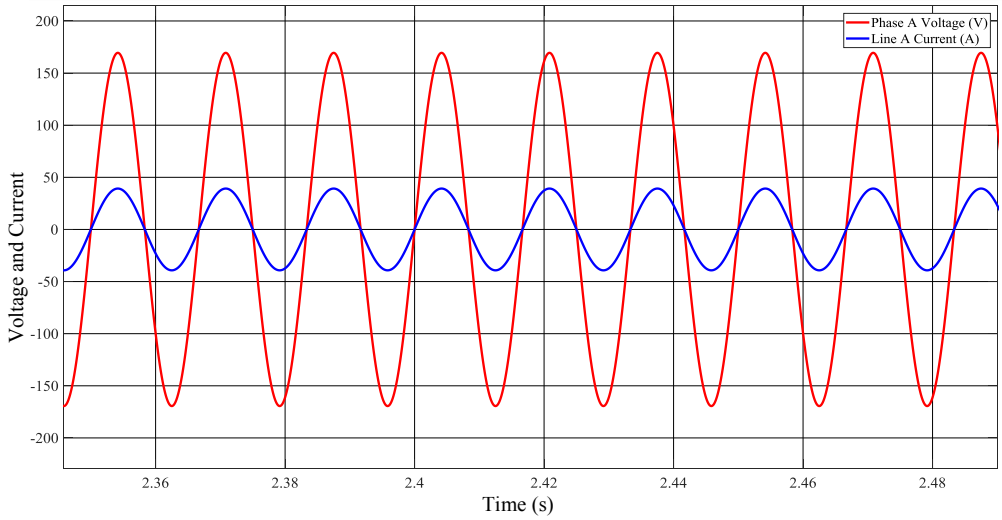

Figure 4.10: Phase voltage superimposed with the line current for the heating electrical load during a winter day.

As illustrated from Figure 4.10, the load line current is in phase with the phase voltage for unity PF. Indeed, for a purely resistive load, only active power is consumed. The line current RMS value is evaluated as 27.73 A. With a large current flowing through small resistors of high power capacity, the heat is dissipated and used for increasing the temperature.

The input current and voltage at the PCC for the winter scenario is shown in Figure 4.11.

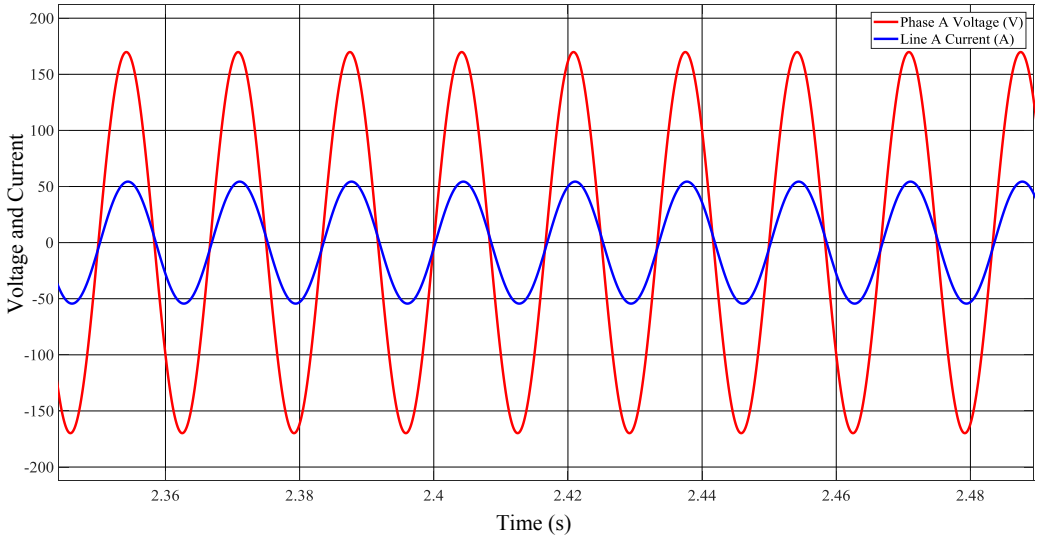

Figure 4.11: Input phase voltage superimposed with the line current at the PCC for the summer operational scenario.

As illustrated by Figure 4.11, the power characteristics of the input signal at the PCC for the winter operational scenario are defined by a sinusoidal current with a low level of harmonics and a high PF. The measured current waveform illustrates the effect of the two loads considered for the winter operational scenario. The corresponding power characteristics at the PCC are summarized in Table 4.5.

Table 4.5: Power characteristics at the PCC for the winter operational scenario.

System Parameters	Ratings
Voltage (RMS)	208 V
Current (RMS)	38.43 A
Apparent Power (S)	13 850 VA
Active Power (P)	13 769 W
PF	0.99
THDi	0.29 %

As can be observed from Table 4.5, when considering only the main electrical loads used under these constraints, the input current and voltage signals show no concerns in terms of power quality risks. Indeed, the PF is evaluated at 0.99 whereas the current THD is calculated as 0.29 %. Therefore, almost all the power drawn from the grid is directly fed to the load with minimal waste. The main characteristic noted for the winter scenario is indicated by the higher amount of real power drawn from the grid to meet the more exhaustive requirements during this season. Hence, higher power consumption results in a higher economic cost for the tunnel during the winter. Even though, the input signal at the PCC presents high PF and low THD, a higher power consumption from an industrial load like the tunnel is not ideal for the electrical provider during peak hours. Indeed, the power demand of the tunnel combined with the high demand of the surrounding area can lead to difficulties on the electrical provider side, where power could be lost due to the high demand.

4.5 Tunnel Operational Profile During an Emergency Event

The final operational scenario to be considered is in a situation of emergency where the tunnel electrical system is disconnected from the electrical grid and must be supplied by the emergency power supply (diesel generator). During such an event, only the critical loads are to be powered

by the back-up supply. Hence, the main lighting system is no longer powered and only the emergency tunnel and night lighting systems are supplied. Furthermore, under this operational scenario, heating cables must be powered by the diesel generator to ensure continuous flow in the fire protection conduits in the situation where a fire is ignited inside the tunnel. As such, a heating load is added to the simulated system for this scenario. Additionally, the ventilation system is also incorporated into the system to be analyzed as it is still required to extract polluted air from the tunnel even though the tunnel is only fed by the emergency system. Furthermore, as for the heating cables, the ventilation system must be able to operate at full capacity in the event of a fire to extract the fumes from the tunnel. The simulated system configuration for this emergency scenario is illustrated below in Figure 4.12.

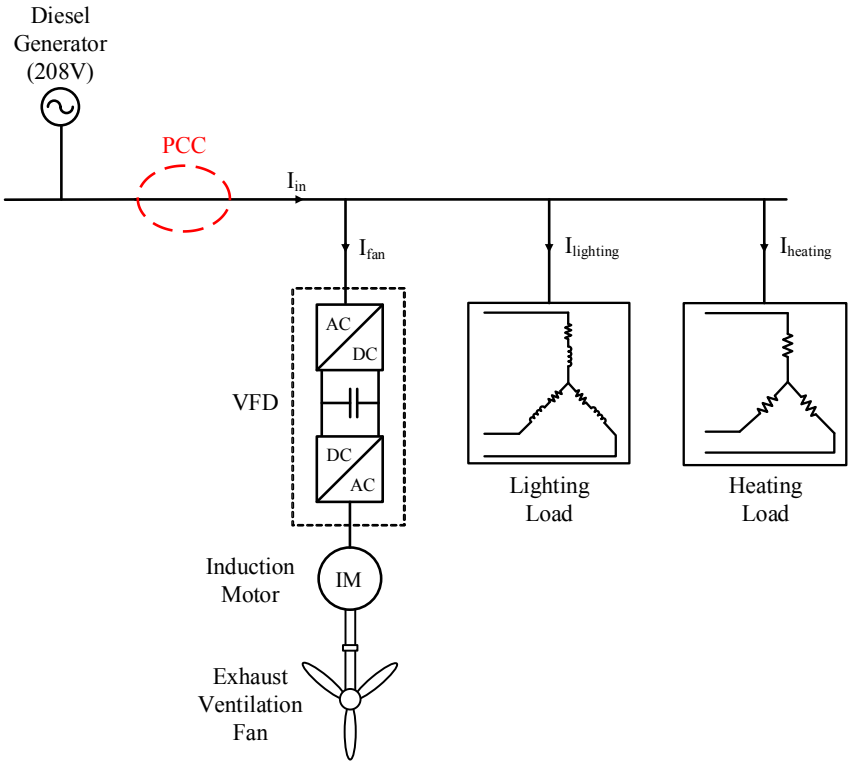

Figure 4.12: SLD of the simulated tunnel system configuration during an emergency event.

Hence, the considered electrical loads for the simulation of this scenario include the emergency and night lighting system, the heating cables and a single fan for the ventilation system. Furthermore, instead of being powered by the grid, the loads are supplied only by the diesel generator. The ratings of each are then scaled down as only the essential systems are powered. The ratings of the system elements shown in Figure 4.12 are summarized in Table 4.6.

Table 4.6: System element ratings for the tunnel operational profile during an emergency event.

System Element	Ratings
Diesel Generator	208 V, 3.5 kW, 60 Hz
Exhaust Ventilation Fan	208 V, 6.1 A, 2-hp, 60 Hz
Heating Load	208V, 1000 W, 60 Hz
Lighting Load	208V, 750 VA, PF = 0.95, 60 Hz

As indicated in Table 4.6, the diesel generator model proposed in [51] is rated at 3.5 kW. Consequently, the loads powered under this scenario should then be rated under this threshold, hence the reason for the values tabulated in Table 4.6. Indeed, as indicated previously in this research work, the actual emergency system of the tunnel is designed to have the capability to supply the power demand only from the essential loads. Doing so, it maintains a safe operation once disconnected from the grid.

4.5.1 Power Characteristics Assessment of Emergency Scenario

The emergency operational scenario consists of the emergency power supply which feeds only the essential loads during an emergency event. For the tunnel infrastructure, diesel generators are used as backup power supply and have limited power capabilities. In this operational scenario, the considered essential loads are defined as a scaled-down rating percentage of the heating, lighting, and ventilation electrical system presented previously. Indeed, lowering the ratings is allowing for a more accurate representation of the operational profile of the tunnel during an emergency event.

As opposed to the summer and winter operational scenarios where the grid is the main supply, the emergency diesel generator supply is impacted by the current harmonics generated by the tunnel electrical system non-linear loads (i.e. the VFDs). The ideal power supply is characterized by sinusoidal waveforms for the voltage and current. However, synchronous generators have a larger reactance compared to the electrical grid, which results in voltage distortion in the supplied signal. As such, once the diesel generator is loaded with the ventilation system, the supplied voltage should no longer be sinusoidal due to the high levels of harmonics introduced by the VFD [60, 61].

To illustrate the effects of the non-linear load on the synchronous diesel generator, the simulated operational scenario during an emergency scenario first starts with the grid supplying

the ventilation fan. Then, the grid is disconnected at T = 2s, and the emergency diesel generator takes over and maintains the supply to the ventilation fans. Furthermore, at T = 4s, the load imposed on the generator is increased with the heating and lighting loads being turned on. Finally, at a simulation time of T = 6s, the ventilation fan is disconnected and the diesel engine is only providing power to the heating and lighting loads. The complete transients for the diesel engine supply line voltage and current during the emergency operational scenario described above are illustrated in Figure 4.13.

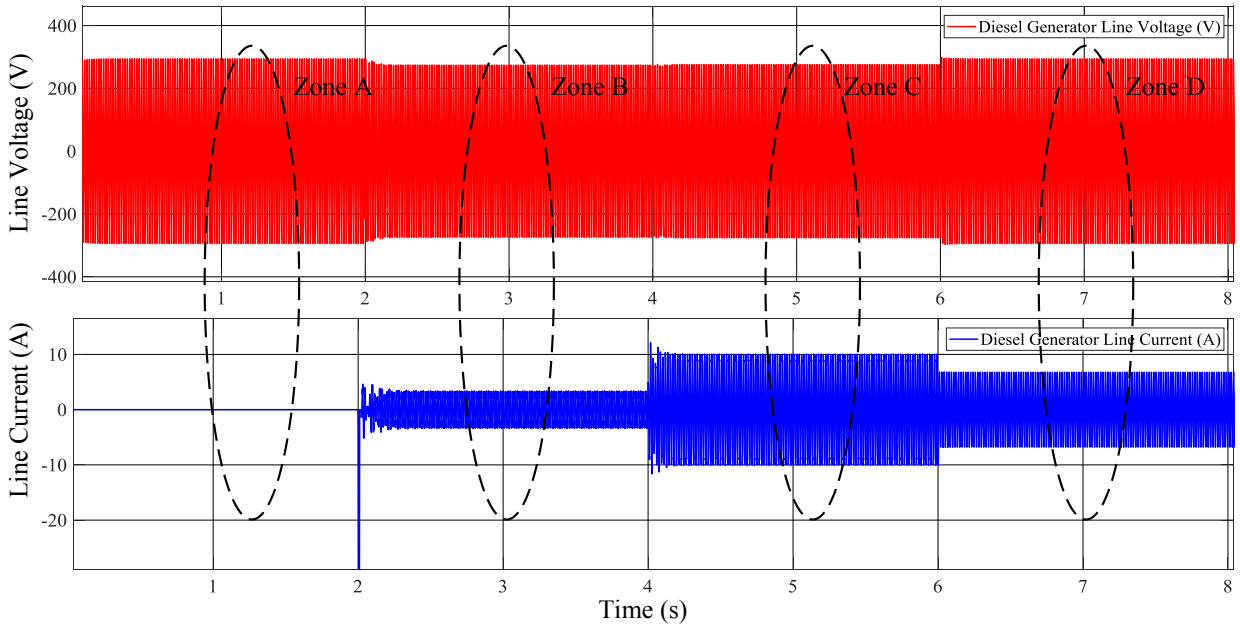

Figure 4.13: Diesel generator supply line voltage and current during the emergency operational scenario.

Moreover, the waveforms shown in Figure 4.13 are analyzed deeper by having a look at the different circled areas for which, the supply or the loads vary. Indeed, the effects of the different loads applied on the diesel generator are reflected in the line current and voltage waveforms. The different sequences observed in Figure 4.13 are summarized as:

- Zone A: Grid is still connected to the tunnel distribution system feeding the ventilation fan load;
- Zone B: Grid is suddenly disconnected and the emergency diesel generator takes over as the backup power supply feeding only the ventilation load;

- Zone C: Emergency diesel generator is now feeding all essential loads (i.e. heating, lighting, and ventilation loads); and
- Zone D: Emergency diesel generator is only feeding the heating and lighting loads.

As such, a closer perspective on the line current and voltage for each zone described above is taken and illustrated in Figure 4.14 a), b), c), and d).

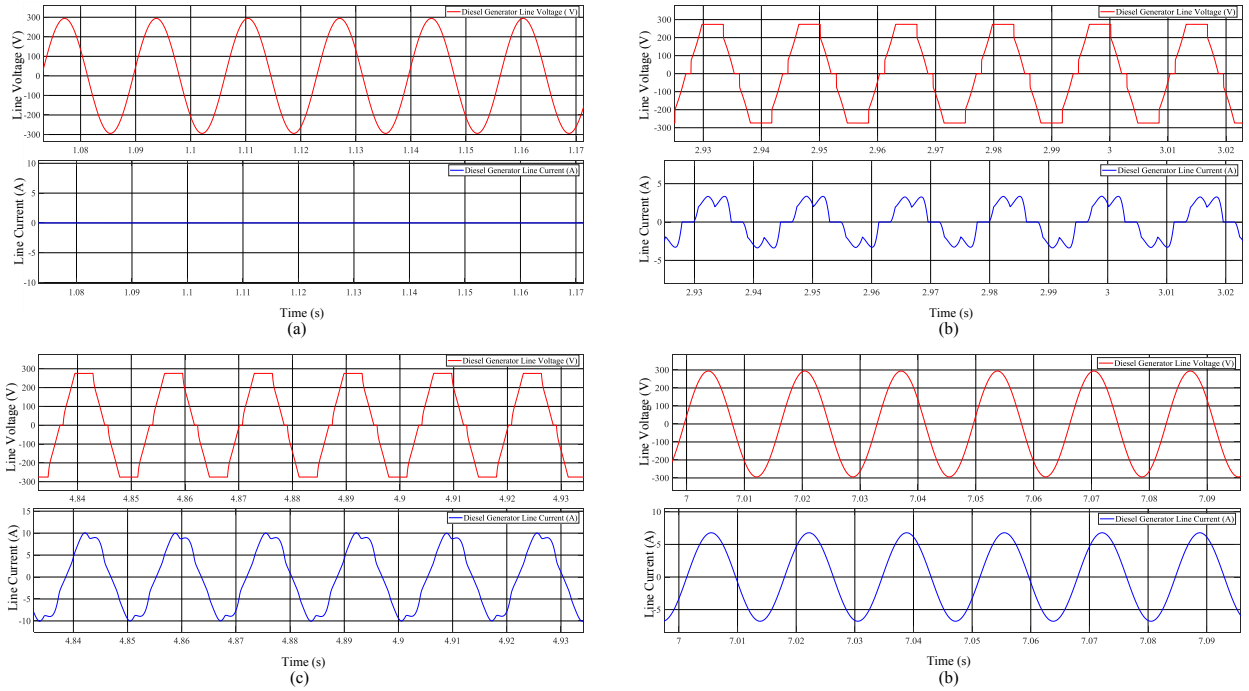

Figure 4.14: Diesel generator supply line current and waveforms during, (a) Zone A, (b) Zone B, (c) Zone C, and (d) Zone D.

As illustrated in Figure 4.14 (a), with the grid still connected to the simulated system, the current drawn from the emergency backup power supply is zero and the voltage measured at the PCC is perfectly sinusoidal. The current drawn at the PCC has the same characteristics of the computed current shown in Figure 4.5.

Then, in Figure 4.14 (b), the grid is disconnected and the diesel generator supplies the ventilation load. The effects of the non-linear load on the diesel generator are reflected in the emergency supply voltage waveforms and currents. The ventilation fan is loaded with a torque of 3.5 N-m and a rotational speed of 1765 RPM. Thus, the active power drawn by the induction motor is evaluated as 646.9 W, which is corresponding to 18.5 % of the diesel generator capacity. As

indicated previously, the input voltage of the diesel generator is distorted when connected to the ventilation fan system due to the VFD used to control the motor rotational speed. The high input impedance interacts with the current harmonics and results in a distorted supply voltage. This phenomenon is not observed in the situation where the grid is supplying the drive because of the low input impedance of the facility power transformer and the high mechanical inertia contributing to maintaining a constant voltage supply [61, 62]. The tunnel power transformer is sized to carry the total electrical infrastructure loads whereas the diesel generator is sized to carry only the essential loads. Furthermore as shown in Figure 4.14 (b), the diesel generator line voltage is flattened at the peak of the waveform with the peak value reduced with the non-linear load connected. However, the RMS value across the diesel generator terminals is maintained at 208V.

In Figure 4.14 (c), the heating, lighting, and ventilation electrical loads are now all supplied by the emergency diesel generator. Again, the same observations can be made in regards to the voltage waveform distortion caused by the harmonics generated by the VFD. The current drawn by these two linear loads is no longer sinusoidal as it would be seen if the electrical grid was the main supply. Consequently, the level of harmonics introduced back into the system is increasing with all the loads connected to the diesel generator.

Then, in Figure 4.14 (d), the ventilation system is disconnected and the diesel generator is only supplying the heating and lighting load. Without the non-linear load, the diesel generator terminal voltage is now purely sinusoidal, and is reflected on the line current as well.

The characteristics observed at the diesel generator terminals for each zone of interest are summarized in Table 4.7.

Table 4.7: Diesel generator terminals line current and voltage characteristics.

System Parameters	Zone A	Zone B	Zone C	Zone D
RMS Voltage (V)	207.9	207.3	204.6	208
Peak Voltage (V)	294	273.5	275	294.1
RMS Current (A)	0	2.17	6.86	4.80
Current THD (%)	N/A	28.33	13.29	0.78
Voltage THD (%)	2.55	10.39	13.55	0.79

As illustrated from Table 4.7, once the diesel generator takes over the electrical grid as the main supply for the tunnel electrical loads, a voltage drop is observed in the supply line voltage following the transition from Zone A to Zone B. Indeed, the current harmonics introduced by the non-linear load are resulting in a voltage drop across the generator source impedance. Consequently, the voltage THD of the system is increasing, thus resulting in a distorted signal. Then, as illustrated from the transition between Zone C and D where the non-linear load is disconnected, the supply voltage is back to a sinusoidal waveform and the current and voltage harmonics are back within standards [63].

The effects on non-linear loads on the emergency generator should be mitigated to avoid any damages to the equipment. Indeed, the introduction of current and voltage harmonics into the system can result in overheating of windings, torque pulsations or even losses in the system [64]. The length of life of the generator alternator is also reduced due to harmonics as the insulation damaged by extensive overheating.

Moreover, strategies can be implemented to limit the effect of the non-linear load on the synchronous diesel generator. Indeed, one strategy implies to oversize the generator to a rating corresponding to 2-2.5 the kVA rating of the drive [65]. Furthermore, the system can be improved by increasing the number of linear loads and limiting the quantity of non-linear loads on the generator by including parallel generators. Consequently, the ratio between the linear loads and non-linear loads would be reduced in regards to the generator capacity. Indeed, the non-linear loads should be limited to below 25% of the diesel generator capacity [66].

4.6 Summary

In this Chapter, the tunnel electrical profile was simulated based on the on-site measurements and the tunnel operation profile discussed in Chapter 2. Indeed, using the observed power characteristics of the considered main electrical loads and the developed drive model for the ventilation system, three different operational scenarios were computed in Simulink. First, the summer operational profile was comprised of the ventilation and the lighting loads. The simulation of this scenario showed some power quality limitations generated by the operation of the VFDs used for the fan speed control. Then, the winter scenario was comprised of the heating and lighting loads. With both systems being mostly resistive, the power consumed from the grid was almost only active power, showing no power quality limitations. However, the power demand was

considerably higher due to the intensive heating requirements. Finally, the emergency operational profile was defined as a disconnection from the electrical grid supply after which the backup diesel generator takes over as the main supply to only the essential loads. As such, to analyze the impact of each load on the diesel generator, it was first loaded only with the non-linear ventilation system. It was observed that, as opposed to the electrical grid, the generator supplied voltage was distorted due to the presence of harmonics generated by the VFD, for which the voltage waveform was no longer sinusoidal. Then, the diesel generator was loaded with the heating, lighting and ventilation load at a lower power rating as a means to follow the diesel generator power ratings. Again, due to the non-linear load applied to the backup power supply, the distorted voltage was also reflected in the current drawn by the resistive loads that are the heating and lighting loads. Finally, the VFD and induction motor were disconnected from the distribution system allowing the diesel generator to power only the heating and lighting loads. Once the non-linear load was disconnected, the terminal voltage supplied by the diesel generator retrieved its sinusoidal waveform. As a result, the current drawn by these loads were also sinusoidal, thus reducing the level of harmonics introduced back into the supply source.

.

Chapter 5: Conclusion and Future Work

5.1 Conclusion

In this work, the Louis-Hippolyte Lafontaine tunnel connecting the island of Montreal and the South Shore was taken as a case study for the implementation and analysis of the electrical profile observed for this critical infrastructure. Indeed, from this research project, the tunnel electrical profile was implemented considering the three main contributors in terms of energy consumption designated by the heating, lighting, and ventilation electrical loads. The developed system was also comprised of the electrical grid, as the main supply, and a diesel generator, as the auxiliary and emergency power system.

The actual electrical system of the tunnel was first defined and described based on the data provided by the engineering group responsible for the tunnel rehabilitation project. The provided information was then used to present the tunnel operation profile on a yearly basis as a means to illustrate the power demand fluctuations with the different periods of the year. Indeed, from the power demand profile taken for the year of 2015, a higher power demand was observed for the colder months of the winter due to intensive heating requirements under these outside weather constraints. Consequently, it illustrated how intensive are the heating loads in regards to the overall electrical profile of the tunnel. In order to define the estimated power consumption of each load, power equations, using only the information available in the tunnel's logging database system, were developed based on measurements taken on-site for the three main considered electrical loads. From this visit, the outcome of the site survey showed that the heating loads were purely resistive, the lighting loads were also almost consuming only active power and the ventilation fan power consumption was affected by the speed of operation.

Then, when referring to the literature survey, it was determined that the exhaust and supply ventilation fan systems were essential to the operation of the tunnel, to maintain a proper air quality level. As such, in order to implement a representative model for the electrical profile of the tunnel, a variable frequency drive (VFD) model was developed as a means to control the induction motor applied voltage and thus, the rotational speed. The implemented control system followed the theory of open-loop scalar control or constant voltage-over-frequency ratio as typically used in the industry ventilation systems due to the simplicity of the control and the absence of high precision

speed control requirements in these particular applications. To overcome the low-frequency voltage drop, a voltage boost was added. The control was developed for a 2-hp induction motor, for which the parameters were extracted using the method proposed by the IEEE Std 112^{TM} – 2017. Moreover, the modulation strategy used was the SPWM to which was incorporated third harmonic injection to enhance the DC bus utilization ratio of the inverter and overcome the limitations imposed by the laboratory equipment. By accomplishing this, it allowed for the induction motor to operate at rated voltage experimentally. Thus, the constant V/f curve was generated for both the simulation and experimental system under no-load conditions. The outcome of this procedure showed that both V/f ratios closely followed the theoretical quantity. Furthermore, the experimental curve was slightly offset from the simulation due to the non-idealities effects generated by the real components, which were not considered in the simulation. Then, the control strategy was validated for speed command changes as a means to emulate the operational profile of the tunnel ventilation system subjected to vary the speed based on the air quality level.

Finally, using the on-site measurements of the main electrical loads considered for this research work and the developed drive model, the tunnel electrical system was emulated for three different operational scenarios: a summer day, winter day and during an emergency event. From these simulations, the summer operational scenario indicated limitations in the power quality at the point of common coupling (PCC) due to the effects of the more frequent operation of the ventilation system. Indeed, the power electronic device that is the variable frequency drive used to control the motor speed introduced current harmonics back to the source in addition to reducing the power factor. Second, the winter scenario showed no sources of power quality issued at the PCC. Indeed, the heating system being purely resistive and the lighting system being mainly resistive, the PF at the PCC was almost at unity. However, as proven by the tunnel yearly power demand, the emulated winter scenario showed a considerable increase in the power demand compared to the summer scenario due to the exhaustive heating requirement. Last, the emergency event emulated scenario showed some concerns in regards to the capability of the diesel engine to supply the essential loads and especially the non-linear loads that are the VFDs and induction motor.

5.2 Future Work

In terms of future work related to this research project, one task would involve the implementation of an improved model of the electrical profile of the tunnel by incorporating

additional electrical loads. Indeed, with the heating, lighting, and ventilation contributing in great proportion to the energy consumption of the tunnel, other loads such as electrical pumps are also being frequently operated, thus also influencing the operational profile of the tunnel. Therefore, with the electrical pumps operating in a similar way to the operation of the ventilation fans using a VFD for speed control, the developed drive model could be modified for such applications based on new machine parameters.

In reference to the drive model, due to the nature of the application being used for ventilation fans system, the requirement for higher accuracy in terms of speed control is not mandatory. Indeed, the open-loop scalar control is commonly used for this type of application. However, the low-speed performance of the control implemented in Chapter 3 could be improved to ensure constant flux for the complete operating range of the induction motor. While maintaining an open-loop control scheme, the scalar control could be improved through feedforward slip compensation to compensate for large slip occurrence at lower frequencies. Additionally, instead of using a constant boost voltage, for which the value is accurate for one operation point, the control strategy could be improved by implementing an adaptive boost voltage varying with the operating conditions of the induction motor.

Additionally, in this work, the assumption that electrical loads were physically located nearby, thus neglecting the impedance voltage drop in the distribution system was taken. To improve the system model, the impedance of the conductors interconnecting the distribution system could be modeled. Doing so, one could have a better representation of the electrical profile of the tunnel at the point of common coupling (PCC) with the electrical grid. Hence, the power characteristics observed at the PCC would help define which power quality mitigation strategies would be more suitable for this type of critical infrastructure.

Finally, one additional task that could be achieved related to this research work would be the analysis of incorporating to the tunnel power system alternative renewable supply systems. With renewable technologies emerging and their associated cost reducing, systems combining PVs and energy storage system could be considered as potential add-ons to the tunnel's infrastructure. The use of renewable energy could limit the tunnel power demand on the electrical grid and result in economic and environmental benefits. Furthermore, the energy stored in the battery energy storage system (BESS) could also be used to mitigate power quality issues in the electrical system, while

acting as a shunt active filter and achieving reactive power compensation. Moreover, the emergency supply could be modified to a combination of PVs and BESS with diesel generator sets. This hybrid configuration would also reduce the size of the diesel generator set.

REFERENCES

[1] Government of Canada, "Critical Infrastructure," 07 June 2019. [Online]. Available: https://www.publicsafety.gc.ca/cnt/ntnl-scrt/crtcl-nfrstrctr/index-en.aspx. [Accessed 02 April 2019].

[2] M. Panteli and P. Mancarella, "Modeling and Evaluating the Resilience of Critical Electrical Power Infrastructure to Extreme Weather Events," *IEEE Systems Journal,* vol. 11, no. 3, pp. 1733-1742, 2017.

[3] M. Panteli, P. Mancarella, X. Hu, I. Cotton, D. Calverly, R. Wood, C. Pickering, S. Wilkinson, R. Dawson and K. Anderson, "Impact of climate change on the resilience of the UK power system," in *IET International Conference on Resilience of Transmission and Distribution Networks (RTDN) 2015*, 2015.

[4] R. Bruemmer, "Rebuilding Louis-Hippolyte-La Fontaine Tunnel a four-year ordeal," Montreal Gazette, 21 June 2018. [Online]. Available: https://montrealgazette.com/news/local-news/rebuilding-louis-hippolyte-la-fontaine-tunnel-a-four-year-ordeal. [Accessed 2 April 2019].

[5] K. Olikara, "Power Quality Issues, Impacts, and Mitigation for Industrial Customers," Rockwell Automation, Inc, 2015. [Online]. Available: https://literature.rockwellautomation.com/idc/groups/literature/documents/wp/power-wp002_-en-p.pdf;. [Accessed 6 May 2019].

[6] A. E. Mofty and K. Youssef, "Industrial power quality problems," in *Conference and Exhibition on Electricity Distribution, 2001. Part 1: Contributions. CIRED. (IEE Conf. Publ no. 482)*, Amsterdam, 2001.

[7] H. Dagdougui, N. Mary, A. Beraud-Sudreau and L. Dessaint, "Power management strategy for sizing battery system for peak load limiting in a university campus," in *2016 IEEE Smart Energy Grid Engineering (SEGE)*, Oshawa, ON, 2016.

[8] R. Belaidi, M. Hatti, A. Haddouche and M. M. Larafi, "Shunt active power filter connected to a photovoltaic array for compensating harmonics and reactive power simultaneously," in *4th International Conference on Power Engineering, Energy and Electrical Drives*, Istanbul, 2013.

[9] S. Srinath, S. Poongothai and T. Aruna, "PV Integrated Shunt Active Filter for Harmonic Compensation," *Energy Procedia,* vol. Volume 117, pp. 1134-1144, 2017.

[10] T. Lledó-Ponsati, D. Montesinos-Miracle and S. Galceran-Arellano, "Multipurpose emulation platform for research in microgrids," in *2016 18th European Conference on Power Electronics and Applications (EPE'16 ECCE Europe),*, 2016.

[11] Transports Québec, "Tunnel Louis-Hippolyte La Fontaine - Réfection majeure," Gouvernment du Québec, [Online]. Available: https://www.transports.gouv.qc.ca/fr/projets-infrastructures/reseau-routier/projets-routiers/CMM/louis-hippolyte-lafontaine/Pages/refection-pont-tunnel.aspx. [Accessed 6 April 2019].

[12] Ministère des Transports, de la Mobilité Durable et de l'Électrification des Transports, "Tunnel Louis-Hippolyte-La Fontaine, Réfection Majeure et Travaux liés," 27 June 2017. [Online]. Available: https://www.transports.gouv.qc.ca/fr/projets-infrastructures/reseau-routier/projets-routiers/CMM/louis-hippolyte-lafontaine/Documents/Documentation/pres-tlhl-briefing-2017-06-27.pdf. [Accessed 04 April 2019].

[13] Google Maps, "Tunnel Louis-Hippolyte-La Fontaine, Boucherville, Qc," [Online]. Available: https://www.google.com/maps/place/Tunnel+Louis-Hippolyte-La+Fontaine,+Boucherville,+QC/@45.5831804,-73.5078705,2823m/data=!3m1!1e3!4m5!3m4!1s0x4cc91d01cd9b1251:0xb97153aaf6a84e09!8m2!3d45.5819934!4d-73.49262. [Accessed 6 April 2019].

[14] A. K. Athienitis, K. D'Avignon, C. Alecsandru, P. Pillay, T. Stathopoulos and L. Wang, "Efficacité énergétique et déglaçage des entrées et sorties sans utilisation de sel du tunnel louis-hippolyte-la fontaine," Montreal, 2017.

[15] A. Gagnon and S. B. Ekongolo, "Note technique no6 - calcul des charges électriques du système existant," Montreal, 2016.

[16] A. Dolara, "Power quality in public lighting systems," in *Proceedings of 14th International Conference on Harmonics and Quality of Power - ICHQP 2010*, 2010.

[17] C. R. B. S. Rodrigues, P. S. Almeida, G. M. Soares, J. M. Jorge, D. P. Pinto and H. A. C. Braga, "An experimental comparison between different technologies arising for public lighting: LED luminaires replacing high pressure sodium lamps," in *2011 IEEE International Symposium on Industrial Electronics*, Gdansk, 2011.

[18] T. M. Blooming and D. J. Carnovale, "Application of IEEE STD 519-1992 Harmonic Limits," in *Conference Record of 2006 Annual Pulp and Paper Industry Technical Conference*, Appleton, WI, 2006.

[19] U. S. Department of Energy, "Improving Motor and Drive System Performance: A Sourcebook for Industry," 2014.

[20] C. M. Burt, X. Piao, F. Gaudi, B. Busch and a. N. F. N. Taufik, "Electric Motor Efficiency under Variable Frequencies and Loads," *Journal of irrigation and drainage engineering,* vol. 134, no. 2, pp. 129-136, 2008.

[21] Y. Shakweh, "33 - Drives Types and Specifications," in *Power Electronics Handbook (Third Edition)*, Boston, Butterworth Heinemann, 2011, pp. 897-898.

[22] T. Rai and P. Debre, "Generalized modeling model of three phase induction motor," in *2016 International Conference on Energy Efficient Technologies for Sustainability (ICEETS)*, 2016.

[23] F. Stinga, A. Soimu and M. Marian, "Online estimation and control of an induction motor," in *2015 19th International Conference on System Theory, Control and Computing (ICSTCC)*, 2015.

[24] K. B. Hunasikatti, R. L. Naik and B. V. Hiremath, "Implementation of FPGA Based Closed Loop V/f Speed Control of Induction Motor Employed for Industrial Applications," in *2018*

Second International Conference on Advances in Electronics, Computers and Communications (ICAECC), 2018.

[25] D. Karthik and T. R. Chelliah, "Analysis of scalar and vector control based efficiency-optimized induction motors subjected to inverter and sensor faults," in *2016 International Conference on Advanced Communication Control and Computing Technologies (ICACCCT)*, 2016.

[26] V. R. Babu, T. Maity and S. Burman, "Optimization of energy use for mine ventilation fan with variable speed drive," in *2016 International Conference on Intelligent Control Power and Instrumentation (ICICPI)*, 2016.

[27] Natural Resources Canada, "Variable Frequency Drives: Energy Efficiency Reference Guide," CEATI International, 2009.

[28] B. K. Bose, "Variable frequency drives-technology and applications," in *ISIE '93 - Budapest: IEEE International Symposium on Industrial Electronics Conference Proceedings*, 1993.

[29] P. C. Sen, "Electric motor drives and control-past, present, and future," *IEEE Transactions on Industrial Electronics,* vol. 37, no. 6, pp. 562-575, 1990.

[30] S. Gdaim, A. Mtibaa and M. F. Mimouni, "Design and Experimental Implementation of DTC of an Induction Machine Based on Fuzzy Logic Control on FPGA," *IEEE Transactions on Fuzzy Systems,* vol. 23, no. 3, pp. 644-655, 2015.

[31] A. K G R and W. Beevi M, "Indirect Field Oriented Control of induction motor using Predictive Current Controller,"," in *2015 International Conference on Control Communication & Computing India (ICCC)*, 2015.

[32] Z. Zhang, Y. Liu and A. M. Bazzi, "An improved high-performance open-loop V/f control method for induction machines," in *2017 IEEE Applied Power Electronics Conference and Exposition (APEC)*, 2017.

[33] K. T. Chau, "Induction Motor Drives," in *Electric Vehicle Machines and Drives: Design, Analysis and Application*, 2015, pp. 39-68.

[34] A. Munoz-Garcia, T. A. Lipo and D. W. Novotny, "new induction motor V/f control method capable of high-performance regulation at low-speeds," *IEEE Transactions on Industry Applications,* vol. 34, no. 4, pp. 813-821, 1998.

[35] A. Smith, S. Gadoue, M. Armstrong and J. Finch, "Improved method for the scalar control of induction motor drives," *IET Electric Power Applications,* vol. 7, no. 6, pp. 487-498, 2013.

[36] A. Kumar and T. Ramesh, "Direct Field Oriented Control of Induction Motor Drive," in *2015 Second International Conference on Advances in Computing and Communication Engineering*, 2015.

[37] N. V. Naik and S. P. Singh, "Improved dynamic performance of direct torque control at low-speed over a scalar control," in *2013 Annual IEEE India Conference (INDICON)*, 2013.

[38] J. N. Forestieri, M. Farasat and A. M. Trzynadlowski, "Indirect Real- and Reactive-Power Control of Induction Motor Drives," *IEEE Journal of Emerging and Selected Topics in Power Electronics,* vol. 6, no. 4, pp. 2109-2125, 2018.

[39] P. Vladimir and S. Dmitry, "To issue of designing scalar closed-loop controllers for frequency controlled induction motor drives," in *018 17th International Ural Conference on AC Electric Drives (ACED)*, 2018.

[40] Baldor Reliance, "Product Information Packet M1556T," [Online]. Available: https://www.baldorvip.com/servlet/productInfoPacket/M1556T.pdf.

[41] Power and Energy Society, "IEEE Standard Test Procedure for Polyphase Induction Motors and Generators," *IEEE Std 112-2017 (Revision of IEEE Std 112-2004),* pp. 1-115, 2018.

[42] A. E. Fitzgerald, C. Kingsley and S. D. Umans, "Chapter 6: Polyphase induction machines," in *Electric Machinery*, 6 ed., New York, McGraw-Hill, 2003, pp. 306-348.

[43] S. J. Chapman, "Chapter 7: Induction Motors," in *Electric Machinery Fundamentals*, 4 ed., New York, McGraw-Hill, 2004, pp. 380-467.

[44] S. Haghbin and T. Thiringer, "DC bus current harmonics of a three-phase PWM inverter with the zero sequence injection," in *2014 IEEE Transportation Electrification Conference and Expo (ITEC)*, 2014.

[45] Ngoc-ThinhQuach, S. H. Chae, S. Lee, H. Kim and E. Kim, "Analyzing Modulation Techniques for the Modular Multilevel Converter," *International Journal of Computer and Electrical Engineering,* vol. 8, no. 4, pp. 259-271, 2016.

[46] N. Mohan, "Chapter 8: Space Vector Pulse Width-Modulated (SV-PWM) Inverters," in *Advanced Electric Drives: Analysis, Control and Modeling Using MATLAB/Simulink*, New Jersey, John Wiley & Sons, 2014, pp. 119-128.

[47] A. M. Trzynadlowski, "Chapter 7: Dc-to-AC Converters," in *Introduction to Modern Power Electronics*, 2nd ed., New Jersey, John Wiley & Sons, 2010, pp. 288-297.

[48] I. T. Force, "Load representation for dynamic performance analysis (of power systems)," *IEEE Transactions on Power Systems,* vol. 8, no. 2, pp. 472-482, 1993.

[49] A. Arif, Z. Wang, J. Wang, B. Mather, H. Bashualdo and D. Zhao, "Load Modeling—A Review," *IEEE Transactions on Smart Grid,* vol. 9, no. 6, pp. 5986-5999, 2018.

[50] M. EL-Shimy, N. Mostafa, A. Afandi, A. Sharaf and M. A. Atti, "Impact of load models on the static and dynamic performances of grid-connected wind power plants: A comparative analysis," *Mathematics and Computers in Simulation,* vol. 149, pp. 91-108, 2018.

[51] M. H. Ashourianjozdani, L. A. C. Lopes and P. Pillay, "Power sharing control strategy for a no-storage hydrokinetic-diesel system in an isolated AC mini-grid," in *2016 IEEE Power and Energy Society General Meeting (PESGM)*, 2016.

[52] A. J. Collin, G. Tsagarakis, A. E. Kiprakis and S. McLaughlin, "Development of Low-Voltage Load Models for the Residential Load Sector," *IEEE Transactions on Power Systems,* vol. 29, no. 5, pp. 2180-2188, 2014.

[53] S. Jing, "Research on Active Power Factor Correction of the Electronic Ballast for High-Pressure Sodium Lamps Based on L6563," in *2010 International Conference on Electrical and Control Engineering*, 2010.

[54] G. C. R. Sincero and A. J. Perin, "High Pressure Sodium Lamp High Power Factor Electronic Ballasts Using AC–AC Converters," *IEEE Transactions on Power Electronics,* vol. 22, no. 3, pp. 804-814, 2007.

[55] J. Mucko, "Properties of high-pressure sodium lamp by different supply methods," 217.

[56] S. Ben-Yaakov and M. Gulko, "Design and performance of an electronic ballast for high-pressure sodium (HPS) lamps," *IEEE Transactions on Industrial Electronics,* vol. 44, no. 4, pp. 486-491, 1997.

[57] I. I. Artyukhov, S. V. Molot, S. F. Stepanov, S. G. Kalganova, S. V. Trigorly and G. N. Tulepova, "Voltage quality problems in power supply system of boiler stations using pumps with variable-frequency drive," in *2018 19th International Scientific Conference on Electric Power Engineering (EPE)*, Brno, 2018.

[58] M. G. Sayed, M. Aly, E. M. Ahmed and M. Orabi, "Power quality enhancement of variable frequency drive by PWM bridgeless dual boost converter," in *2017 Nineteenth International Middle East Power Systems Conference (MEPCON)*, Cairo, 2017.

[59] Z. Huaying, S. Shuaibin, L. Sha, H. Zhiwei, W. Yusheng, L. Ping and Z. Jiang, "The Research about Influence of Voltage Sag on High-Pressure Sodium Lamp," in *2016*

International Conference on Smart Grid and Electrical Automation (ICSGEA), Zhangjiajie, 2016.

[60] P. S. G. Dana and P. S. Ion, "Study of the harmonics of current and voltage for a synchronous generator in the context of railway constraints," in *2016 International Symposium on Power Electronics, Electrical Drives, Automation and Motion (SPEEDAM)*, Anacapri, 2016.

[61] G. M. Williams, "Understanding Nonlinear Loads and Generator Set," Caterpillar Inc., [Online]. Available: https://www.idc-online.com/technical_references/pdfs/electrical_engineering/Generators_and_nonlinear_loads.pdf. [Accessed 05 May 2019].

[62] J. T. Streicher, "Applying Variable Speed Drives on A Generator Power Source," [Online]. Available: https://literature.rockwellautomation.com/idc/groups/literature/documents/wp/drives-wp014_-en-p.pdf. [Accessed 05 May 2019].

[63] A. Thakur, "Managing Emergency Generators with Nonlinear Loads," Kohler Co., 2017. [Online]. Available: https://resources.kohler.com/power/kohler/industrial/pdf/Managing_Emergency_Generators_with_Nonlinear_Loads.pdf. [Accessed 10 June 2019].

[64] S. V. Giannoutsos and S. N. Manias, "A Systematic Power-Quality Assessment and Harmonic Filter Design Methodology for Variable-Frequency Drive Application in Marine Vessels," *IEEE Transactions on Industry Applications,* vol. vol. 51, no. 2, pp. 1909-1919, 2015.

[65] R. Akey and J. Fell, "Sizing Generators When They are Used to Power Variable Speed Drive," ABB, 17 December 2013. [Online]. Available: https://library.e.abb.com/public/0007878791e17d0985257cca005bb048/LVD-EOTN64U-EN_REVA.pdf. [Accessed 07 May 2019].

[66] C. Nebula and B. Bradley, "How VFDs Affect Genset Sizing," 2006. [Online]. Available: https://www.trane.com/content/dam/Trane/Commercial/global/products-systems/education-training/engineers-newsletters/control-systems-electrical-considerations/admapn019en_0106.pdf. [Accessed 06 May 2019].